



UNIVERSITY OF  
BIRMINGHAM

# Constraining the effects of axion-cooling in solar-like oscillators

E. Willett<sup>A</sup>    D. Williams<sup>B</sup>    J. Parker<sup>C</sup>    A. Lyttle<sup>D</sup>    C. Green<sup>E</sup>    P. O'Connor<sup>F</sup>  
K. Bruce<sup>G</sup>    J. Campbell-Barr<sup>H</sup>    M. Clarke<sup>I</sup>    R. Hickey<sup>J</sup>    T. Mehta<sup>K</sup>    S. Rizvi<sup>L</sup>  
A. Sharp<sup>M</sup>    O. Wightwick<sup>N</sup>

March 23, 2018

---

## Abstract

Stars provide a unique opportunity to study novel particle physics. With the advent of asteroseismology, high precision constraints on stellar parameters have allowed for the study of hypothetical weakly interacting particles, such as the axion. This study employs a variety of models and observational data of solar-like oscillators in the mass range  $0.8 M_{\odot}$ – $2.0 M_{\odot}$ . We have sought to constrain the potential coupling of axions to photons and electrons. Considering the tip luminosity of the RGB, an upper bound of  $g_{a\gamma} \lesssim 1.5 \times 10^{-10} \text{ GeV}^{-1}$  was determined. This value was matched by another method considering the position of the red clump on an asteroseismic HRD. With better implementation of model physics, this method suggests that the upper limit might be further constrained to the range  $0.6 \times 10^{-10} \text{ GeV}^{-1}$ – $1.0 \times 10^{-10} \text{ GeV}^{-1}$ . Furthermore, we have shown that consideration of the mixed mode period spacing in low-luminosity red giants offers potential for inference on the changes to internal structure due to axion production.

---

**Keywords:** asteroseismology, axions, red giants, solar-like oscillators, stellar models

---

<sup>A</sup>Lead

<sup>B</sup>Subgroup 1 Lead

<sup>C</sup>Subgroup 2 Lead

<sup>D</sup>Editor

<sup>E</sup>Subgroup 1 Editor

<sup>F</sup>Subgroup 2 Editor

# Contents

<b>1</b>	<b>Introduction</b>	<b>3</b>
<b>2</b>	<b>Theory</b>	<b>4</b>
2.1	Evolution of Low & Intermediate-Mass Stars . . . . .	4
2.1.1	Pre-Main Sequence . . . . .	4
2.1.2	Main Sequence . . . . .	4
2.1.3	Sub-Giant Branch . . . . .	5
2.1.4	Red Giant Branch . . . . .	5
2.1.5	Red Clump . . . . .	6
2.1.6	Asymptotic Giant Branch . . . . .	6
2.2	Asteroseismology . . . . .	7
2.3	Axions . . . . .	10
2.4	Stellar Axion Energy-Loss . . . . .	10
2.4.1	Coupling to Photons . . . . .	11
2.4.2	Coupling to Electrons . . . . .	11
2.4.3	The Impact of Energy-Loss . . . . .	12
<b>3</b>	<b>Methods</b>	<b>14</b>
3.1	Introduction to MESA . . . . .	14
3.1.1	Stopping Conditions . . . . .	14
3.2	Modifying MESA . . . . .	14
3.2.1	Implementing the Primakoff Process . . . . .	14
3.2.2	Implementing Axion Coupling to Electrons . . . . .	15
3.3	GYRE . . . . .	15
3.3.1	Running GYRE . . . . .	15
3.3.2	Limitations . . . . .	16
3.3.3	Using the Outputs . . . . .	16
3.4	Data Trimming . . . . .	17
3.4.1	Justification of Data Trimming Parameters . . . . .	17
3.5	Comparing the RGB bump and RC luminosity . . . . .	18
3.5.1	Locating the RGB Bump and RC in MESA models . . . . .	18
3.5.2	Estimating the Luminosity of the RGB Bump . . . . .	18
3.5.3	Estimating RC Luminosity from Observed Data . . . . .	19
3.6	Effect of Axions on the TRGB . . . . .	19
3.7	Frequency & Period Spacing Investigation . . . . .	19
3.7.1	Isolating the RC . . . . .	20
3.7.2	Core Overshooting . . . . .	20
3.7.3	Available data for $\Delta\Pi_1$ . . . . .	21
3.8	Axion cooling in the asteroseismic HRD . . . . .	22
3.8.1	Modifying the RC trimming parameters . . . . .	23
3.8.2	Axion-photon coupling constant and HeCB mixing schemes . . . . .	23
3.8.3	Calibrating the value of $g_{10}$ using old open clusters . . . . .	23
3.8.4	Obtaining Synthetic Cluster Data . . . . .	24
3.9	Modelling Low-Luminosity RGB Stars . . . . .	24

<b>4 Results &amp; Discussion</b>	<b>26</b>
4.1 Combining Asteroseismology with the HRD . . . . .	26
4.2 Statistical analysis of MESA output data . . . . .	26
4.2.1 Quantifying the change in mass and radius with different $g_{10}$ values . . . . .	27
4.2.2 Application of statistical method to model grids . . . . .	28
4.2.3 Analysis of mass difference as a result of axion cooling in the RGB bump and RC . . . . .	29
4.2.4 Conclusions drawn from statistical analysis . . . . .	30
4.3 Investigating Stellar Central Properties . . . . .	30
4.3.1 Chemical Composition . . . . .	30
4.3.2 Pressure . . . . .	31
4.3.3 Central Temperature . . . . .	32
4.3.4 Radius . . . . .	32
4.3.5 Surface Gravity . . . . .	32
4.3.6 Analysis of changes in mass and density . . . . .	34
4.4 Population & Asteroseismic Parameters . . . . .	34
4.4.1 Analysis of changes in the R parameter . . . . .	34
4.4.2 Analysis of the changes in $\Delta\Pi$ . . . . .	35
4.4.3 Analysis of changes in $\nu_{max}$ . . . . .	37
4.4.4 Analysis of the first cycle models - $\Delta\nu$ . . . . .	37
4.4.5 Mass and metallicity effects on the $\Delta\Pi_1$ vs $\Delta\nu$ plot . . . . .	37
4.5 Luminosity Changes . . . . .	39
4.5.1 Luminosity of the Main Sequence and the Sub-Giant Branch . . . . .	39
4.5.2 Luminosity of the RGB tip . . . . .	40
4.5.3 Mixing Zones and the RGB Bump . . . . .	41
4.5.4 The RGB bump as a Function of Mass . . . . .	41
4.6 RC Luminosity vs RGB Bump Luminosity . . . . .	41
4.6.1 Analysis of behaviour of MESA simulations . . . . .	41
4.6.2 Model-Data Comparison . . . . .	42
4.7 Effect of Axions on the TRGB . . . . .	43
4.7.1 Interpretation . . . . .	43
4.7.2 Improvements . . . . .	44
4.7.3 Axion-Electron TRGB . . . . .	45
4.7.4 Alternative considerations from M5 . . . . .	45
4.8 Frequency & Period Spacing Investigation . . . . .	47
4.8.1 Overshooting Changes . . . . .	47
4.8.2 Calibrating $g_{10}$ using old open clusters . . . . .	48
4.8.3 Synthetic Cluster Results . . . . .	48
4.9 $\Delta\Pi$ of Low-Luminosity Red Giants . . . . .	51
4.9.1 Propagation Diagrams . . . . .	51
4.9.2 Fits to the mixed mode pattern . . . . .	55
4.9.3 Observing Period Spacing . . . . .	57
4.10 Sound Speed Profiles . . . . .	57
<b>5 Conclusions</b>	<b>61</b>
5.1 Luminosity of RGB Bump and RC . . . . .	61
5.2 TRGB Summary . . . . .	61
5.3 Asteroseismic HRD Conclusion . . . . .	61
5.4 Low-Luminosity RGB Summary . . . . .	62
5.5 Limitations of Current Data . . . . .	62
<b>A Stellar Modelling</b>	<b>68</b>
A.1 MESA Additions . . . . .	68
A.1.1 Axion Coupling to Electrons . . . . .	68
A.1.2 Improvements . . . . .	69
A.2 GYRE Input . . . . .	70
<b>B Tables</b>	<b>72</b>
B.1 Luminosity of the TRGB . . . . .	72

# Chapter 1

## Introduction<sup>H</sup>

Since the general review on asteroseismology by Brown and Gilliland (1994) [1], capabilities within the field have extended far beyond what was possible. Initially, the only accurate data on solar-like oscillations available was for the Sun, and while it remains an excellent example of the information that can be gathered using asteroseismic methods, missions such as Kepler and CoRoT in recent years have produced an unprecedented amount of high quality data on a wide ranging stellar population. This has hugely benefited understanding of stellar physics as a whole and allowed for continued constraining of physical quantities to an increasingly high precision. Asteroseismology is an exceptionally useful tool with regards to characterising stellar properties to an unmatched level of precision. In simple terms, its the utilization of stellar oscillations in order to determine the internal structure. Other methods fail to provide information on the deep stellar interior, which is fundamental for understanding stellar evolution and structure.

The unmatched mass and scale of stars, combined with the extreme conditions present in stellar interiors, may be exploited as laboratories in which we can study in conditions which cannot be replicated on Earth. Under these unique circumstances, small effects can be integrated over a long lifetime. This makes it possible to experiment with processes inaccessible otherwise, particularly in particle physics. An example of such a process is the production of hypothetical weakly-interacting particles. The existence of such particles could potentially affect both the evolution and internal structure of stars. One such particle is the axion; it is theorized that they might be produced in stellar cores. Analogous to neutrinos, their weak interactions with matter allow the transport of energy out of the stellar interior, effectively making them energy sinks. The result of this increased energy loss in the star would potentially be a modified evolutionary timescale, luminosity, or internal structure. The latter can only be probed using asteroseismic methods.

There have been previous studies focused on constraining axion coupling by exploiting stellar models, primarily using the Sun, given that we possess greater information on it than on any other star. In particular, we acknowledge the recent papers CAST (2017) [2] and Giannotti et al. (2017) [3] which report upper

bounds for the axion-photon and axion-electron coupling constants which this study assumes to be standard. These values are  $g_{a\gamma} \lesssim 0.66 \times 10^{-10} \text{ GeV}^{-1}$  and  $gae \approx 1.6 \times 10^{-13}$ . However, the effects axions have on stars is a relatively new field, and is as of yet unquantified. Recent studies have investigated the effects of axions in the Sun [2], white dwarfs, on the delays to helium ignition on the RGB and in supernovae neutrino bursts [4]. As a potential cold dark matter candidate, confirming the existence of axions could pave the way to understanding unexplained areas of physics and change the way we consider the structure of our universe.

The primary aim of this report is to identify the effects of axion production in solar-like oscillators and examine existing observational data for evidence of these effects. In preparation for the availability of the data from the upcoming missions, including Gaia, TESS and PLATO, this report suggests some avenues for further study based on our findings.

The report is structured as follows:

- The second section provides an overview of the theoretical background of the evolution of low to intermediate-mass stars, asteroseismology, axions and the effect they might have in stars.
- The third section describes the various methods applied in order to test for the presence of axion effects within stars. There is a review of the function of Modules for Experiments in Stellar Astrophysics (MESA), a computational environment for the creation of stellar models and GYRE, a source code for analysing stellar oscillations. Details on the handling and manipulation of the data obtained by these means and observations of real stars are also described.
- In the fourth section all results yielded by this analysis are presented. This section includes a detailed discussion on their implications in the context of this study. We consider whether the predicted effects of axions on stellar evolution match up with observational evidence.
- In the final section a set of more general conclusions are drawn. The current limitations on observational data are also discussed, as well as the potential of future research to build on the outcomes of this report.

# Chapter 2

## Theory

### 2.1 Evolution of Low & Intermediate-Mass Stars<sup>B</sup>

The evolution of any star is marked by a series of distinct phases, resulting from changes in the internal composition that predominantly arise due to nuclear reactions. Most of these stages correlate with changes in the observable properties. The overall state of a star can be described using a series of differential equations; the most prominent of which are known as the ‘structure equations’, listed below, with symbols taking their common definitions,

$$\frac{dM}{dr} = 4\pi r^2 \rho \quad (2.1)$$

$$\frac{dp}{dr} = -\frac{Gm}{r^2} \rho \quad (2.2)$$

$$\frac{dL}{dm} = \epsilon_{nuc} - \epsilon_\nu - T \frac{ds}{dt} \quad (2.3)$$

$$\frac{dT}{dr} = -\nabla \frac{Gm\rho}{r^2} \frac{T}{p} \quad (2.4)$$

with  $\epsilon$  being the energy generation rate,  $s$  is the specific entropy and  $\nabla \equiv d \ln T / d \ln P$ . These equations are that of conservation of mass, momentum, energy and the temperature gradient respectively.

The detailed evolution of higher mass stars ( $\gtrsim 2.0 M_\odot$ ) is beyond the scope of this report, since they differ quite significantly to solar-like stars, having more complicated post-MS evolutionary tracks. Nonetheless they do go through the same rough evolutionary states:

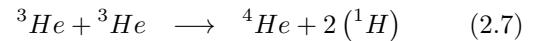
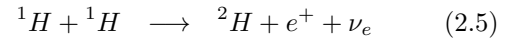
1. Pre-Main Sequence
2. Main Sequence
3. Sub-Giant Branch
4. Red Giant Branch
5. Red Clump / Horizontal Branch
6. Asymptotic Giant Branch

#### 2.1.1 Pre-Main Sequence

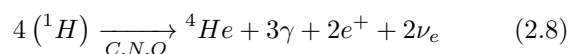
Stars form from contracting regions of gas in interstellar space. These balls of gas contract, heating up due to the release of gravitational energy. The star follows what is known as a Hayashi Track as it evolves towards the MS — the time taken for this process to take place is dependent upon the mass, typically ranging from  $10^5$  years (for high mass) to around  $10^7$  years for a solar-like star. The luminosity initially decreases due to increasing opacity, with the gas acting as an ideal gas. However as core temperatures increase, opacity decreases once again as radiation becomes the dominant energy transport mechanism, with the result that the surface temperature,  $T_{eff}$ , increases. Once the conditions of pressure and temperature are sufficient in the core of the protostar, nuclear fusion reactions may begin and the star reaches the Zero-Age Main Sequence (ZAMS). The position of a star on the ZAMS curve represented on a Hertzsprung-Russell Diagram (HRD) is a function of its mass, which impacts the luminosity and effective temperature of the surface.

#### 2.1.2 Main Sequence

This is the longest-lasting portion of a stars evolution, and arguably the most stable. hydrogen is burnt through nuclear reactions to form helium, either via the proton-proton (pp) chain, represented by the following set of reactions:



or through the Carbon-Nitrogen-Oxygen (CNO) cycle described in simplified terms thus:



The rates of each of these processes are highly dependent upon core temperature (and hence initial mass of the star), such that:

$$\epsilon_{pp} \propto \rho X_H^2 T^4 \quad (2.9)$$

$$\epsilon_{CNO} \propto \rho X_H X_{CNO} T^{18} \quad (2.10)$$

where  $X_i$  represents the chemical abundance of a given component. The relative contribution to the total energy output is illustrated in Figure 2.1, with the transition between the dominant mechanism occurring between  $1.2 M_\odot - 1.3 M_\odot$ .

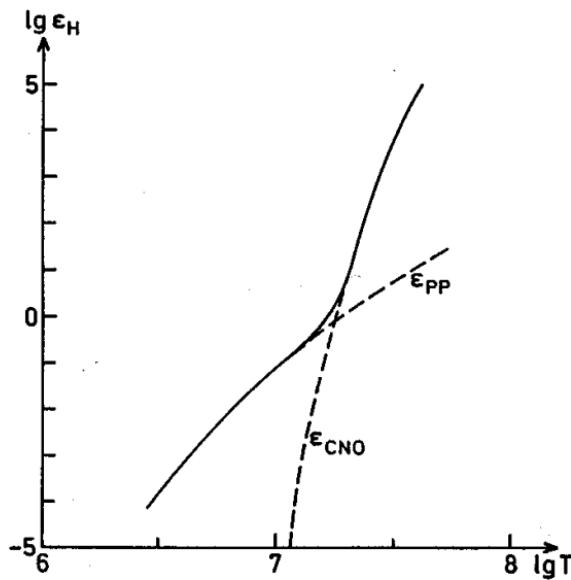


Figure 2.1: Total total energy output  $\epsilon_{nuc}$  ( $\text{erg g}^{-1} \text{s}^{-1}$ ) with increasing core temperature, at density  $1 \text{ g cm}^{-3}$  and chemical abundances  $X = 1$  and  $X_{CNO} = 0.01$  respectively[5].

Stars with the pp-chain as their dominant energy source have radiative cores. Conversely, radiation alone is an insufficient transport mechanism to support the energy provided by the CNO cycle, so these stars have convective cores. As core hydrogen supplies dwindle at the Terminal-Age Main Sequence (TAMS), the star begins to move off the main sequence. For stars around  $1.2 M_\odot$  and greater, there is an extra kink in the evolutionary tracks at the end of the main sequence, which is attributed to an additional burst of hydrogen burning from the CNO cycle.

### 2.1.3 Sub-Giant Branch

Once a MS star has insufficient hydrogen remaining in its core to continue stable fusion, the core begins to contract and increase in temperature. The layer surrounding the inert helium core also contracts whilst the outer envelope expands and cools. During this period,  $T_{eff}$  decreases whilst the luminosity of the star remains relatively unchanged, moving sideways on an HRD.

The contraction of the inner layers provides sufficient temperatures for hydrogen fusion to commence in a shell region around the helium core. An increase in degeneracy pressure among stars with  $M \lesssim 2.0 M_\odot$  allows hydrostatic equilibrium to be maintained throughout this stage, since their cores never exceed the Schönberg-Chandrasekhar mass [6].

### 2.1.4 Red Giant Branch

Eventually the pressure in the core of the Sub-Giant (SG) star become sufficient that it becomes fully degenerate. The degeneracy pressure prevents any fur-

ther collapse of the core: under degenerate conditions, an increase in temperature does not correspond to an increase in density. The hydrogen burning shell remains; as the mass of the degenerate core increases, it contracts further, increasing radius and luminosity. Hence, the rate at which the H-burning shell must use fuel increases as the star progresses up the RGB.

#### RGB Bump<sup>B</sup>

As the hydrogen burning shell progresses radially outwards, it eventually reaches the point where the formerly radiative and convective regions of the star met. Since convection is a very efficient means of mixing material, this results in a discontinuity in the hydrogen abundance. As the shell crosses the boundary, it finds itself in an environment richer in hydrogen so the rate of nuclear reactions decreases, thereby maintaining equilibrium. This results in a drop in the luminosity of the star, until such time that this excess of material has been burned, causing a characteristic bump in the evolutionary track of a star on an HRD.

Notably the RGB bump only occurs for stars of mass less than approximately  $2.2 M_\odot$  [7]. A more thorough description of the RGB bump, as well as a discussion of its potential as a diagnostic tool in asteroseismology can be found in Christensen-Dalsgaard (2015) [7].

#### Helium Flash<sup>B</sup>

The outwardly progressing hydrogen burning shell gradually deposits more matter onto the degenerate core. Once a critical mass has been reached, the temperature is sufficient for helium to begin undergoing nuclear reactions. Conversely to what one might expect, this does not happen in the core of the star, but a shell around it. The core of an RGB star is cooled by neutrino losses, which efficiently remove energy from the innermost regions, as represented in Equation 2.3. The existence of these neutrinos is not attributed to nuclear reactions, but spontaneous emission events due to electro-weak interactions, for example

$$e^- + \gamma \rightarrow e^- + \nu + \bar{\nu} \quad (2.11)$$

that can occur at very high temperatures and pressures.

Importantly however, since the matter is degenerate, the release of energy does not contribute to an increase in pressure, but solely to the internal energy. This increase in temperature accelerates the fusion reactions, resulting in a runaway thermonuclear reaction. Eventually, the temperature rises sufficiently ( $T \approx 10^8 \text{ K}$ ) that degeneracy is lifted in a localised shell around the ignition region.

Helium ignition doesn't proceed in one clean motion however, as degeneracy is only lifted in the local environment of the runaway reaction. The 'flame front' then progresses inwards towards the core, initiating a series of successive pulses until the whole core has its degeneracy lifted; these can be clearly seen

as sharp spikes in the luminosity output from Helium Core Burning (HeCB) in Figure 2.2.

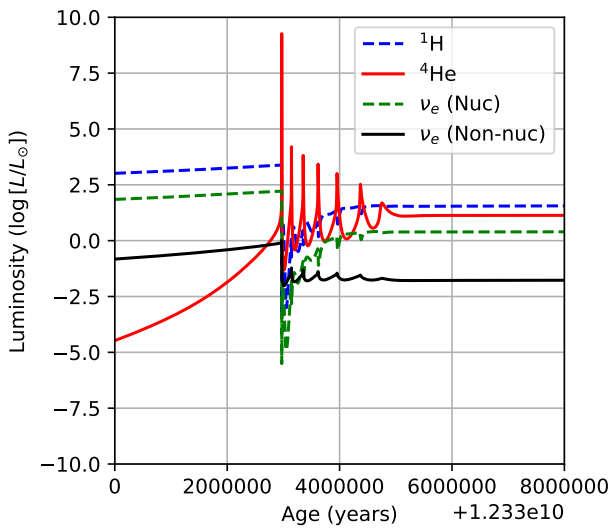
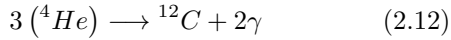


Figure 2.2: Change in contribution from various components to overall luminosity around the period of the helium flash, showing the successive pulses during the migration to the Red Clump (RC).

### 2.1.5 Red Clump

For stars that undergo the helium flash, regardless of mass (within our considered range of  $0.8 M_{\odot}$ – $1.8 M_{\odot}$ ), they will have very similar luminosities and effective temperatures whilst on the RC. This is because the ignition of the degenerate helium core is initiated by the core reaching a critical mass, rather than being dependent upon the mass of the star as a whole. More massive stars undergo a more gradual ignition of helium in their cores (being non-degenerate) and form a more diffuse secondary clump, whilst metal-poor stars display higher effective temperatures during this phase, forming a ‘Horizontal Branch’ on the HRD.

Whilst on the RC, the star undergoes another period of relatively stable evolution of HeCB via the Triple- $\alpha$  process, described thus:



This process is extremely sensitive to temperature, with a rate equation given [8]:

$$\epsilon_{3\alpha} \propto X_4^3 \rho^2 T^{40} \quad (2.13)$$

and as such the convective burning region of the star is very small due to the enormous dependence upon  $T$ . Surrounding the burning core is an inert helium shell, then a thin hydrogen burning shell, followed by an inert outer envelope.

Despite the triple- $\alpha$  process producing carbon, the element never becomes the majority constituent of the core, as shown in Figure 2.3. This is because when conditions are suitable for helium fusion, they are also suitable for the synthesis of oxygen. This happens via

the capture of an alpha particle by a carbon nucleus

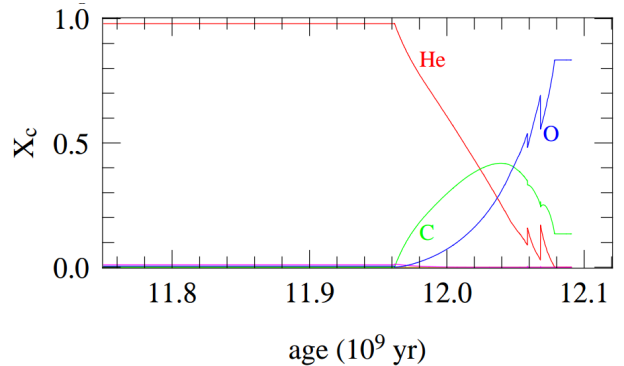
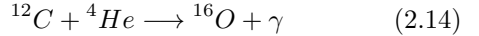


Figure 2.3: Contributions to total composition from different elements over the course of a star’s evolution, given for the example of a solar mass star, showing a peak  $^{12}\text{C}$  value during the RC.[9]

As the helium core fraction drops below 20% [10], core energy output decreases due to the Triple- $\alpha$  process, leading to a compensatory increase in output from the  $\alpha$ -particle capture by carbon, as described in Equation 2.14. This results in an increase in luminosity, marking the start of the transition off the RC, as seen in the far right of Figure 2.4.

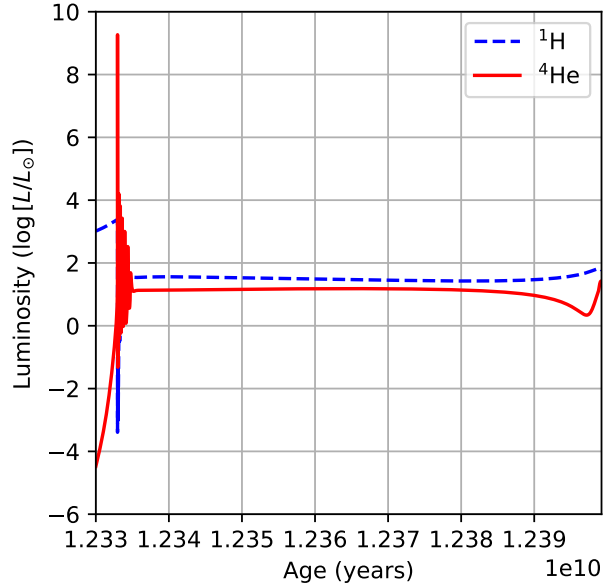


Figure 2.4: Changes in luminosity from hydrogen and helium burning from a period starting just before the helium flash, and encompassing the RC stage.

### 2.1.6 Asymptotic Giant Branch

The cessation of HeCB results in a disruption of the hydrostatic equilibrium in the core of the star. Gravitational collapse of the core occurs in a manner analogous to the evolution off the MS; contraction causes a radiative helium burning shell to ignite around the

now-degenerate carbon-oxygen core, in addition to the hydrogen burning shell farther out. The increase in energy output from the He-burning shell causes the layers above to expand, extinguishing the outer H-burning shell, as shown in Figure 2.5.

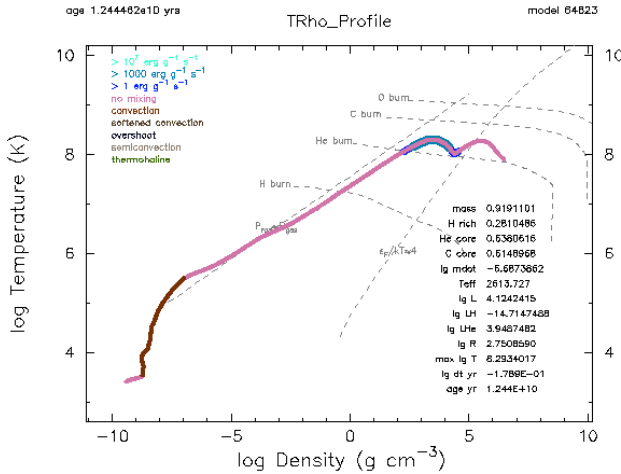


Figure 2.5: Internal profile plot produced in MESA of a solar-mass star during the AGB showing the helium burning shell region.

As the helium burning shell progresses outwards, it eventually comes in relative proximity with the hydrogen burning shell and begins to run out of fuel. The resulting contraction heats up and re-ignites the hydrogen shell; unlike in higher mass stars, conditions never become suitable for the nucleosynthesis of heavier elements and the degenerate core grows in mass.

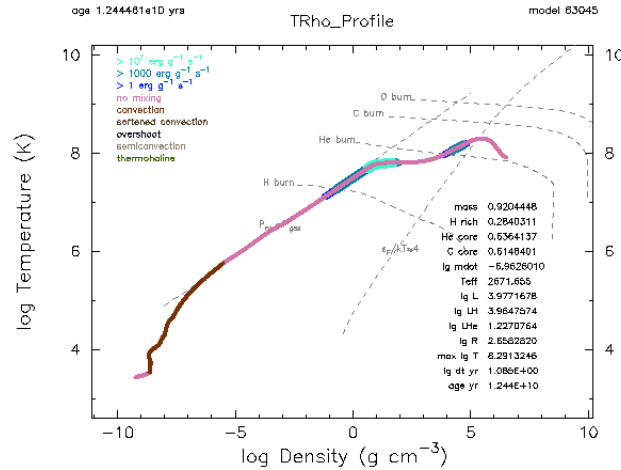


Figure 2.6: The same star as in Figure 2.5 but at a slightly later period of evolution, showing the change in the burning regions as the star undergoes thermal pulses.

This double shell burning phase shown in Figure 2.6 is thermally unstable and alternating periods of single and double-shell burning commence, known as the Thermally Pulsing Asymptotic Giant Branch (TP-AGB) — variations in the star's luminosity as a result of these fluctuations can be seen in Figure 2.7.

As these pulses progress, the already tenuously bound outer layers are gradually sloughed off, leading to the formation of a planetary nebula. This exposes the hot degenerate carbon-oxygen core as the stellar remnant, more commonly known as a white dwarf.

## 2.2 Asteroseismology<sup>A</sup>

Asteroseismic studies of stellar oscillations provide a view into the stellar interior which cannot be obtained by other means of observation. In ‘solar-like’ oscillators, oscillations are stochastically excited (and intrinsically damped) in near-surface convective regions. The oscillations appear as a pattern of expanding and contracting regions in the photosphere, produced by trapped standing waves, and are typically described in terms of spherical harmonics. In this notation, used throughout this report,  $n$  is the radial order and describes the number of radial nodes of the oscillation mode. The angular degree,  $l$ , is related to the wavelength of the mode on the surface of the star (radial modes have  $l = 0$ ) and the azimuthal order,  $m$ , measures the number of oscillation nodes about the stellar equator. The modes of oscillation may be broadly divided into two types, by consideration of their physical origins.

Pressure or p modes are acoustic in nature, and so gradients of pressure act as the restoring force. In MS stars, p modes of high radial order may be detected, with frequencies approximated by

$$\nu_{nl} = \Delta\nu \left( n + \frac{l}{2} + \epsilon \right) - \Delta\nu^2 \left[ \frac{Al(l+1) - B}{\nu_{nl}} \right], \quad (2.15)$$

$\Delta\nu$  is therefore the inverse of the time required for sound to travel the diameter of the star:

$$\Delta\nu = \left( 2 \int_0^R \frac{dr}{c} \right)^{-1}. \quad (2.16)$$

where  $c$  is the sound speed and  $R$  is the stellar radius.  $\epsilon$  is determined by the boundary conditions of the oscillation cavity and is dominated by those near the stellar surface, and  $A$  is defined by

$$A = \frac{1}{4\pi^2\Delta\nu} \left[ \frac{c(R)}{R} - \int_0^R \frac{dc}{dr} \frac{dr}{r} \right] \quad (2.17)$$

$B$  is another correction, determined by the surface conditions [11].

A regular overtone spacing is observed between modes of the same angular degree,  $l$ :

$$\Delta\nu_{nl} = \nu_{nl} - \nu_{n-1,l} \approx \Delta\nu, \quad (2.18)$$

where  $\Delta\nu_{nl}$  is the ‘large frequency separation’. The near approximation of the average large frequency separation ( $\langle \Delta\nu_{nl} \rangle$ ) to  $\Delta\nu$  allows it to be related to the acoustic radius of the star (Equation 2.16), and thus to the mean stellar density:

$$\langle \Delta\nu_{nl} \rangle \propto \langle \rho \rangle^{\frac{1}{2}}. \quad (2.19)$$

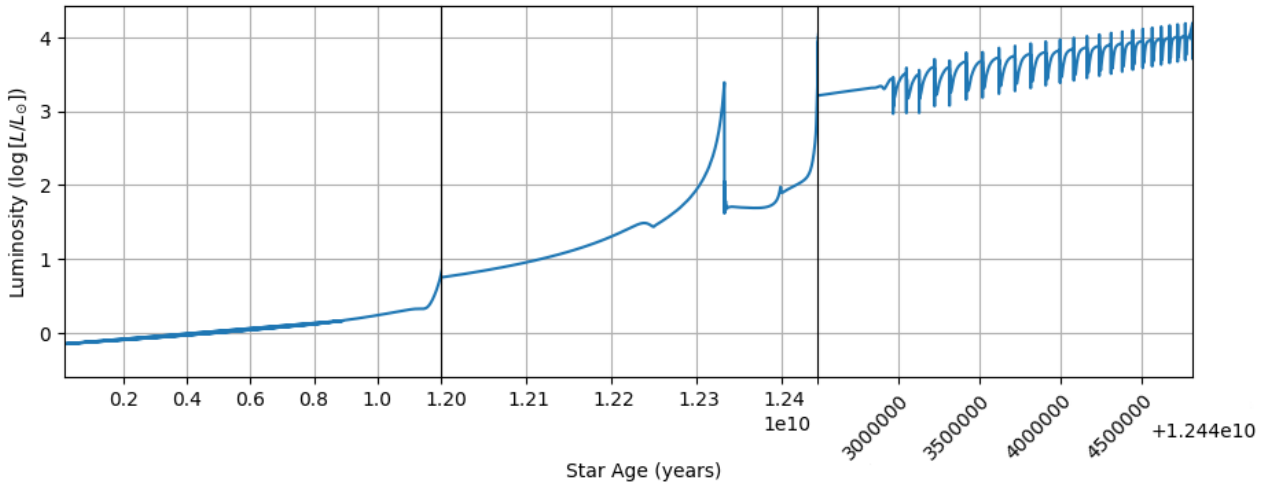


Figure 2.7: The change in output luminosity of a  $1M_{\odot}$  star over its entire lifetime (up to end of TP-AGB phase), showing increased complexity in the lattermost stages of evolution.

This pattern also implies a degeneracy, the departure from which is described by

$$\delta\nu_{ll+2}(n) = \nu_{nl} - \nu_{n-1l+2} \approx -(4l + 6) \frac{\Delta\nu}{4\pi^2\nu_{nl}} \int_0^R \frac{dc}{dr} \frac{dr}{r}. \quad (2.20)$$

This ‘small frequency separation’ is sensitive to the sound speed gradient near the stellar core, and thus provides a probe of the conditions in this region. Rotation splits the frequencies of the non-radial modes, resulting in a dependence on the azimuthal order,  $m$ , but this is not considered in detail in this project.

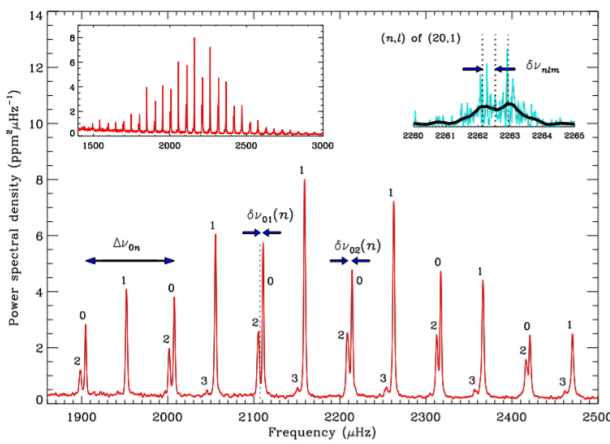


Figure 2.8: Example frequency spectrum of a main sequence star, taken from [11]. The large ( $\Delta\nu_{0n}$ ) and small ( $\delta\nu_{02}(n)$ ) frequency separations are labelled for the  $l = 0$  modes, as is the angular degree,  $l$ , of each oscillation frequency.

The complete frequency spectrum (Figure 2.8) shows a clear envelope with a frequency of maximum power,  $\nu_{max}$ . This value is linked to the conditions of the near-surface regions. The acoustic cut-off fre-

quency is given by:

$$\nu_{ac}^2 = \left( \frac{c}{4\pi H} \right)^2 \left( 1 - 2 \frac{dH}{dr} \right) \quad (2.21)$$

where  $H = -(\mathrm{dln}\rho/\mathrm{d}r)^{-1}$  is the density scale height.  $\nu_{ac}$  controls the behaviour of waves near to the surface, and fixes an upper limit on the frequency of trapped oscillations; only those with  $\nu < \nu_{ac}$  are reflected. Through the use of an isothermal approximation, and by assuming a proportionality between  $\nu_{max}$  and  $\nu_{ac}$ , a scaling relation which links  $\nu_{max}$  to the measurable surface properties may be obtained:

$$\nu_{max} \propto \nu_{ac} \propto \frac{c}{H} \propto \frac{g}{\sqrt{T_{eff}}} \quad (2.22)$$

where  $g \propto M/R^2$  is the surface gravity. By assuming that observed parameters of distant stars, from the MS to the RGB, may be scaled against precisely measured solar properties, we may obtain a set of asteroseismic scaling relations [11]. For example

$$\frac{R}{R_{\odot}} \approx \left( \frac{\nu_{max}}{\nu_{max,\odot}} \right) \left( \frac{\langle \Delta\nu_{nl} \rangle}{\langle \Delta\nu_{nl,\odot} \rangle} \right)^{-2} \left( \frac{T_{eff}}{T_{eff,\odot}} \right)^{0.5}, \quad (2.23)$$

$$\frac{M}{M_{\odot}} \approx \left( \frac{\nu_{max}}{\nu_{max,\odot}} \right)^3 \left( \frac{\langle \Delta\nu_{nl} \rangle}{\langle \Delta\nu_{nl,\odot} \rangle} \right)^{-4} \left( \frac{T_{eff}}{T_{eff,\odot}} \right)^{1.5}, \quad (2.24)$$

$$\frac{L}{L_{\odot}} \approx \left( \frac{\nu_{max}}{\nu_{max,\odot}} \right)^{-4} \left( \frac{\langle \Delta\nu_{nl} \rangle}{\langle \Delta\nu_{nl,\odot} \rangle} \right)^2 \left( \frac{T_{eff}}{T_{eff,\odot}} \right)^5, \quad (2.25)$$

Further manipulation returns expressions describing the relationship of the density and surface gravity with asteroseismic parameters. Estimates of radii by these means are inherently less uncertain than those of mass and luminosity, as the lower powers limit the effect of

errors propagated from measurements of  $\nu_{max}$ ,  $\Delta\nu_{nl}$  and  $T_{eff}$  [11, 12].

Gravity or g modes are driven by buoyancy, and may be visualised as a parcel of stellar material which oscillates around an equilibrium position. The standing waves are trapped between two turning points; one close to the stellar core, and one below the convective zone. The behaviour of these modes is controlled by the Brunt-Väisälä frequency:

$$N^2 = g \left( \frac{1}{\Gamma_1} \frac{d\ln p}{dr} - \frac{d\ln \rho}{dr} \right) \quad (2.26)$$

where  $\Gamma_1 = (\partial \ln p / \partial \ln \rho)_{ad}$ . If we assume that the displacement of the fluid parcel is adiabatic, this frequency describes the rate at which it oscillates about its equilibrium. We may also write

$$N^2 = g^2 \frac{\rho \chi_T}{p \chi_\rho} \left( \nabla_{ad} - \nabla_T - \frac{\chi_\mu}{\chi_T} \nabla_\mu \right) \quad (2.27)$$

which relates  $N$  to the Ledoux criterion and so to the convective stability of the region [12]. If  $N^2 < 0$ , the fluid is unstable to convection and g modes cannot propagate as the parcel will continue to rise or sink, rather than oscillating. g modes have  $\nu < N$  (in a convectively stable region with  $N$  is real) and those of high radial order may be described by

$$\Pi_{nl} = \nu_{nl}^{-1} \approx \Delta\Pi_l(n + \epsilon_g). \quad (2.28)$$

g modes are equally spaced in period, so the period spacing  $\Delta\Pi$  is analogous to  $\Delta\nu$  for the p modes. The period spacing in a convectively stable region  $r_1$  to  $r_2$  may be described by

$$\Delta\Pi_l = \frac{2\pi^2}{\sqrt{l(l+1)}} \left( \int_{r_1}^{r_2} \frac{N}{r} dr \right)^{-1}. \quad (2.29)$$

As a star leaves the MS, the central density increases, resulting in an increase of the Brunt-Väisälä frequency,  $N$  [12]. The increase is sufficient to take it into the frequency range of the high  $n$  p modes, allowing modes of mixed character to form when p and g modes of very similar frequency and the same angular degree interact. They display g mode-like behaviour near the core and p mode-like behaviour near the surface of the star and this may be visualised on a propagation diagram. The solid line shows  $N$  as a function of the fractional radius within the star. The dashed line is the Lamb frequency:

$$S_l^2 = l(l+1) \frac{c^2}{r^2}, \quad (2.30)$$

related to the sound speed gradient in the stellar interior. The regions where a given frequency may oscillate as a p or g mode are indicated; The p mode cavity is the region for which  $\nu > N$  and  $\nu > S_l$ , while the g modes propagate in regions where  $\nu < N$  and  $\nu < S_l$ . The shaded band separating these cavities is the evanescent region, where the waves decay exponentially. The size of this region changes with the evolutionary state of the

star, as both  $N$  and  $S_l$  depend on the internal conditions.  $\Delta\Pi$  may also be used as a probe of evolutionary state, commonly to separate the HeCB stars from the rest of the RGB [13, 14]. Upon the ignition of central helium,  $N$  decreases due to the decrease in the core density, thus increasing  $\Delta\Pi$  [14]. In addition, the convective core of the star shrinks the g mode propagation cavity, further increasing  $\Delta\Pi$ .

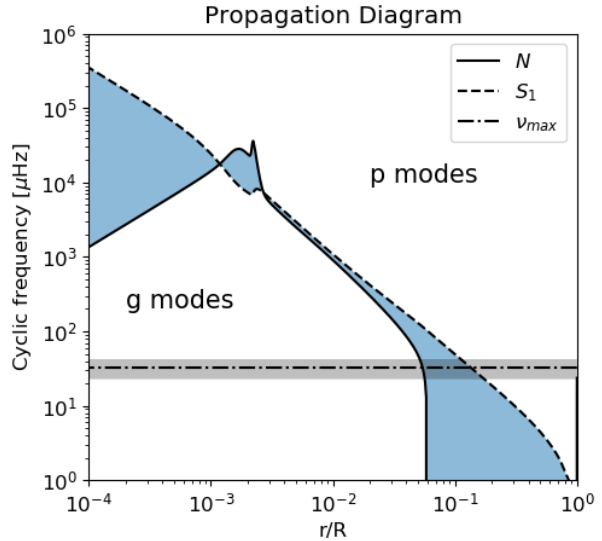


Figure 2.9: An example propagation diagram<sup>D</sup>, produced for a star which has evolved past the RGB bump. The shaded region indicates the evanescent region, where a frequency may not propagate as either a p or g mode and divides the oscillation cavities. An example value of  $\nu_{max}$  is shown, and the grey bands on either side indicate the extent of the mode frequencies generally observable in distant stars.

The use of individual mode frequencies provides an opportunity for further inference on stellar properties, beyond what is possible with the global asteroseismic parameters discussed above. Modelling the interaction of p and g modes allows, in principle, a robust inference of stellar parameters [15], especially those related to the internal properties, such as  $N$ , and the size of the evanescent region. Mosser et al. (2017) have explored the diagnostic potential of the coupling strength of the p and g modes, and its relationship to the size of the evanescent region [16]. From the relationships described in this work for

$$\alpha = \frac{N}{S_1} \quad (2.31)$$

and the coupling factor

$$q \approx \frac{1}{4} \left( \frac{r_1}{r_2} \right)^{\frac{2\sqrt{2}}{\beta}} \approx \frac{1}{4} \alpha^{\frac{2\sqrt{2}}{\beta}} \quad (2.32)$$

we may extract the approximation

$$\frac{N}{S_1} \approx \left( \frac{r_1}{r_2} \right)^\beta \quad (2.33)$$

where  $\beta \approx 1 - 1.5$ .  $r_1$  and  $r_2$  are the inner and outer radii of the evanescent region. The value of  $N$  and the size of the evanescent region are inversely related; an increase of  $N$  corresponds to an increase in the radius of the inner edge of the evanescent region, thus making the whole region smaller.

## 2.3 Axions<sup>D</sup>

Postulated by Roberto Peccei and Helen Quinn in the late 1970s [17], the axion is a hypothetical pseudoscalar particle proposed to resolve the strong Charge-Parity (CP) problem. The CP problem refers to the Quantum Chromodynamics (QCD) prediction that CP symmetry should be violated in strong interactions. CP symmetry is the product of charge conjugation symmetry (same physical laws across a particle-antiparticle transformation) and parity symmetry (such that a reaction occurs at the same rate as its inverse). However, no such CP violation is observed. Peccei-Quinn theory introduces an explanation for the apparent CP conservation through an additional small CP violating term,  $\mathcal{L}_\theta$ , to the QCD Lagrangian [18],

$$\mathcal{L}_\Theta = \Theta \frac{\alpha_s}{8\pi} G_b^{\mu\nu} \tilde{G}_{b\mu\nu}, \quad (2.34)$$

where  $\alpha_s$  is the strong fine-structure constant,  $G$  is the colour field strength tensor,  $\tilde{G}$  is its dual, and  $b$  are the colour degrees of freedom. The parameter,  $\Theta$ , can be allowed to vanish through the presence of a dynamical axion field [19] from which the massless axion emerges.

Strong candidates for dark matter, axions with a decay constant of  $f_a \sim 10^{12} \text{ GeV}$  might even comprise the majority of the illusive cosmological material [20]. Through mixing with the neutral pions via the strong interaction, axions acquire small mass. One might constrain the mass of the axion by considering its cosmic density parameter,  $\Omega_a$ . As expansion of the universe leads to a cooling below the QCD vacuum energy, the axion field must relax to its ground state. This produces a background of cosmic axions which correspond to an axion mass,  $m_a \leq 10^{-5} \text{ eV}$  [18]. The axion mass was also recently constrained to  $50 \mu\text{eV} < m_a < 1,500 \mu\text{eV}$  through simulating the formation of axions during the post-inflation period after the Big Bang [21].

Constraining the axion mass might be most appropriate through cosmological methods, but one can also constrain the existence of the pseudoscalar in extreme physical conditions, such as stellar cores, by considering its coupling to photons and fermions. Examples include probing the cooling anomaly of white dwarfs [22], considering the luminosity of the Tip of the Red Giant Branch (TRGB) in globular clusters [23] and by observing hypothetical axion flux from the Sun through their conversion to x-rays in strong electromagnetic fields. Recently, for example, the CAST (CERN Axion Solar Telescope) constrained the axion-photon coupling strength to  $g_{a\gamma} \lesssim 0.66 \times 10^{-10} \text{ GeV}^{-1}$  [2]. Furthermore, another recent review fits a value

for the axion-electron coupling strength at  $g_{ae} = (1.6 \pm 0.3) \times 10^{-13}$  by combining constraints obtained from observing white dwarfs and evolution on the RGB [3].

## 2.4 Stellar Axion Energy-Loss<sup>D</sup>

Additional energy-loss within a star affects its evolution in many different ways. Let's propose an energy-loss due to process  $x$  within a star. An extra term is added to Equation 2.3 for the luminosity-mass gradient,

$$\frac{dL}{dm} = \epsilon_{nuc} - \epsilon_\nu - \epsilon_x - T \frac{ds}{dt}, \quad (2.35)$$

where  $x$  is the additional energy-loss rate per unit mass, and  $s$  is the specific entropy. In short, an additional energy-loss mechanism causes an increased burning rate, acting to accelerate the evolution of the star and increase its luminosity. This is explored further in Section 2.4.3.

Axions are weakly interacting and thus their production would act to carry energy out of the star. To model this energy-loss, one must consider the processes by which axions might be produced. There are many such processes, some analogous to non-nuclear neutrino losses, but only a few dominate in the extreme conditions of a star. The three processes considered in this report are depicted in Figure 2.10. However, there is also a fourth process worth mentioning: pair production from electron-positron annihilation. The cross-section for axion pair production,  $\sigma \propto s \log s$ , where  $\sqrt{s}$  is the centre-of-mass energy of the process [24]. On the contrary, for neutrinos,  $\sigma \propto s$ . For the typical energies in the cores of  $1 M_\odot - 2 M_\odot$  stars, pair production losses are dominated by neutrinos, thus its effects would be negligible.

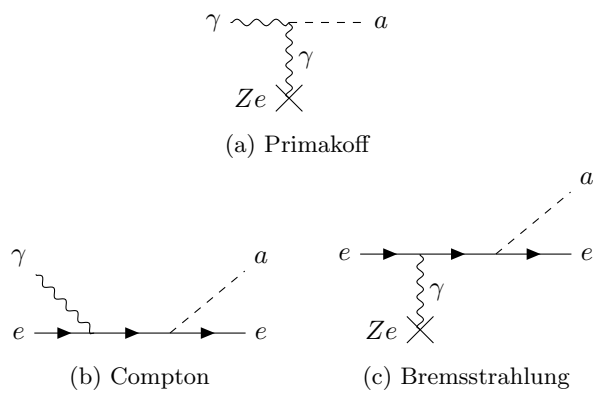


Figure 2.10: Feynman diagrams of the three axion production processes considered in this report. The atomic nucleus is denoted by its charge  $Ze$ .

This report considers the coupling of axions to photons via the Primakoff process, and the coupling to electrons via Compton and bremsstrahlung. Unless otherwise stated, natural units will be used in this section such that  $c = \hbar = k_B = 1$ .

Before proceeding, one must understand the properties of the stellar interior. Firstly, consider the characteristics of a stellar plasma. Let  $X_i$  be the fraction of mass due to some species  $i$  at a given point in the star. The atomic mass is given by  $\mathcal{A}_i u$  (where  $u$  is the atomic mass unit) and the charge is  $\mathcal{Z}_i e$  (where  $e$  is the electron charge). The number density of species  $i$  can be expressed as,

$$n_i = \frac{\rho}{u} \frac{X_i}{\mathcal{A}_i}, \quad (2.36)$$

where  $\rho$  is the density at a given point. Therefore, the number density of electrons is,

$$n_e = \sum_i \mathcal{Z}_i n_i, \quad (2.37)$$

Substituting Equation 2.36) into 2.37, the average number of free electrons per baryon is defined as,

$$Y_e = \sum_i \frac{X_i \mathcal{Z}_i}{\mathcal{A}_i} \approx \frac{\langle \mathcal{Z} \rangle}{\langle \mathcal{A} \rangle}, \quad (2.38)$$

such that,

$$n_e = \frac{\rho}{u} Y_e, \quad (2.39)$$

and  $\langle \mathcal{Z} \rangle e$  and  $\langle \mathcal{A} \rangle u$  are the average charge and atomic mass of the plasma respectively. Note that the approximation in Equation 2.38 is appropriate when  $\mathcal{A} \approx 2\mathcal{Z}$  for helium and hydrogen burning stars.

Secondly, consider the screening wavenumber for a nondegenerate, non-relativistic plasma,  $k_s$ . Screening involves the suppression of long-range electric fields in the presence of an electron fluid, reducing the effective interaction between particles in the plasma to a shorter ranged “screened” Coulomb force. In general, stellar plasmas are considered to be in thermal equilibrium, hence the Debye-Hückel approximation for the wavenumber is used [24]. Therefore,

$$k_s^2 = \frac{4\pi\alpha}{T} \frac{\rho}{u} \left( Y_e + \sum_i \frac{X_i \mathcal{Z}_i^2}{\mathcal{A}_i} \right), \quad (2.40)$$

where  $\alpha \approx 1/137$  is the fine structure constant,  $T$  is the temperature of the plasma, and the right-hand term inside the brackets,

$$\sum_i \frac{X_i \mathcal{Z}_i^2}{\mathcal{A}_i} \approx \frac{\langle \mathcal{Z}^2 \rangle}{\langle \mathcal{A} \rangle}. \quad (2.41)$$

The above approximation is most appropriate for small  $\mathcal{Z}$  (i.e. predominantly for helium and hydrogen composition) and overestimates the sum with increasing  $\mathcal{Z}$ . Therefore, the approximations in Equations 2.38 and 2.41 should be treated with caution in more evolved, massive stars.

### 2.4.1 Coupling to Photons

Axions couple to photons through the Primakoff process. Often called the “Primakoff conversion”, the mechanism converts photons to and from axions in the

presence of strong electromagnetic fields. In the extreme conditions of a stellar plasma, this process allows the production of axions in the electric fields of electrons and nuclei [25] as shown in Figure 2.10a. In non-relativistic conditions, where  $T \ll m_e$ , electrons and nucleons may be treated as far heavier than that of the incident photons. Therefore, the energy of the axion can be considered the same as that of the converted photon.

The energy-loss rate per unit mass is given as [26],

$$\epsilon_{a\gamma} = 27.3 \text{ erg g}^{-1} \text{ s}^{-1} \cdot g_{10}^2 T_8^7 \rho_3^{-1} F(\kappa^2), \quad (2.42)$$

where  $g_{10} \equiv g_{a\gamma} \times 10^{-10} \text{ GeV}^{-1}$ ,  $T_8 \equiv T \times 10^{-8} \text{ K}$  and  $\rho_3 \equiv \rho \times 10^{-3} \text{ g cm}^{-3}$ . The function  $F(\kappa^2)$ , where  $\kappa^2 = k_s^2/4T^2$ , is approximated in equation (4) of Friedland et al. (2013) [26] and is explored in more detail by Raffelt (1996) [25].

Standard model pair production and plasmon decay dominate for very high temperatures and pressure. However, the  $T^7$  dependence in Equation 2.42 means that the best core conditions to probe the effects of axion-photon coupling are that of a HeBC. Core temperatures for helium burning are  $1 \lesssim T_8 \lesssim 4$ , with typical average densities of  $10^5 \text{ g cm}^{-3}$  in the low-mass stars considered in this report. Neutrino energy-loss rates of the order  $1 \text{ erg g}^{-1} \text{ s}^{-1}$  would be expected here [27], whereas losses of about  $10 \text{ erg g}^{-1} \text{ s}^{-1}$  are calculated using Equation 2.42. It must be noted that energy losses of this order could also be expected from non-standard neutrino rates [23, 27].

### 2.4.2 Coupling to Electrons

In a typical stellar plasma, axions couple to electrons via the Compton and Bremsstrahlung processes.

The Compton case has the following energy loss rate, in a non-relativistic medium [28],

$$\epsilon_C = 33.0 \text{ erg g}^{-1} \text{ s}^{-1} \cdot \frac{g_{13}^2}{4\pi} Y_e T_8^6 F_{deg}, \quad (2.43)$$

where  $g_{13} \equiv g_{ae} \times 10^{-13}$  and  $T_8 \equiv T \times 10^{-8} \text{ K}$  are the reduced axion-electron coupling constant and temperature in the regime. A correction for degeneracy effects is contained within  $F_{deg}$ , defined as [28],

$$F_{deg} = (1 + f_{deg}^{-2})^{-1/2}, \quad (2.44)$$

where,

$$f_{deg} = \frac{3E_F T}{p_F^2} = \frac{3T}{\beta_F p_F}, \quad (2.45)$$

contributes to the suppression of the Compton process in high pressure, degenerate regimes [24]. The Fermi velocity is  $\beta_F = p_F/E_F = (m_e^2/p_F^2 + 1)^{-1}$  with the Fermi momentum and energy given by,

$$p_F^2 = (3\pi^2 n_e)^{2/3}, \quad (2.46)$$

$$E_F^2 = m_e^2 + p_F^2, \quad (2.47)$$

respectively, where the electron number density is given in Equation 2.39. Relativistic corrections can be made

to Equation (2.45). However, in relativistic conditions, axion production is dominated by the bremsstrahlung process, so this can be neglected for the low-mass stars considered in this report.

Bremsstrahlung occurs when an electron emits a boson or neutrino pair by deflecting off the Coulomb field of a nucleus. The energy of the emitted particle corresponds to the energy lost by the deceleration of the electron. For axion emission, the bremsstrahlung process can be split into the non-degenerate case (ND) and the degenerate case (D), since both regimes are present in a star.

The energy-loss rate due to the ND case is given empirically by the following [24],

$$\epsilon_{ND} = 590.0 \text{ erg g}^{-1} \text{ s}^{-1} \cdot \frac{g_{13}^2}{4\pi} T_8^{2.5} \rho_6 Y_e \times \sum_i \frac{X_i}{\mathcal{A}_i} \left( \mathcal{Z}_i^2 + \frac{\mathcal{Z}_i}{\sqrt{2}} \right), \quad (2.48)$$

where  $\rho_6 \equiv \rho \times 10^{-6} \text{ g cm}^{-3}$ . In the D regime, the energy-loss rate is also determined to be,

$$\epsilon_D = 10.8 \text{ erg g}^{-1} \text{ s}^{-1} \cdot \frac{g_{13}^2}{4\pi} T_8^4 F \sum_i \frac{X_i \mathcal{Z}_i^2}{\mathcal{A}_i}. \quad (2.49)$$

The function  $F$  in Equation 2.49 is defined as [24]

$$F = \left[ \frac{2 + 5\kappa^2}{15} \ln \left( \frac{2 + \kappa^2}{\kappa^2} \right) - \frac{2}{3} \right] \beta_F^2 + \frac{2}{3} \ln \left( \frac{2 + \kappa^2}{\kappa^2} \right) + \mathcal{O}(\beta_F^4), \quad (2.50)$$

where  $\kappa^2 = k_s^2 / 2p_F^2$  is the screening wavenumber from Equation 2.40 adjusted for electron degeneracy. In the ultrarelativistic limit, further approximations can be made (see Raffelt (1996) [29]).

All three of the energy loss rates are interpolated using the following equation,

$$\epsilon_{ae} = \epsilon_C + (\epsilon_{ND}^{-1} + \epsilon_D^{-1})^{-1}. \quad (2.51)$$

Since the ND and D bremsstrahlung rates are only valid in their respective regimes, they are combined using a harmonic mean.

### 2.4.3 The Impact of Energy-Loss

Energy losses due to novel particles, such as axions, become important when the loss rates are of the same order as standard model neutrino losses. This is apparent in Equation 2.35 for energy conservation adjusted for an additional loss  $\epsilon_X$ . In order to understand the impact of axion energy-loss, one must consider an example star at different evolutionary stages.

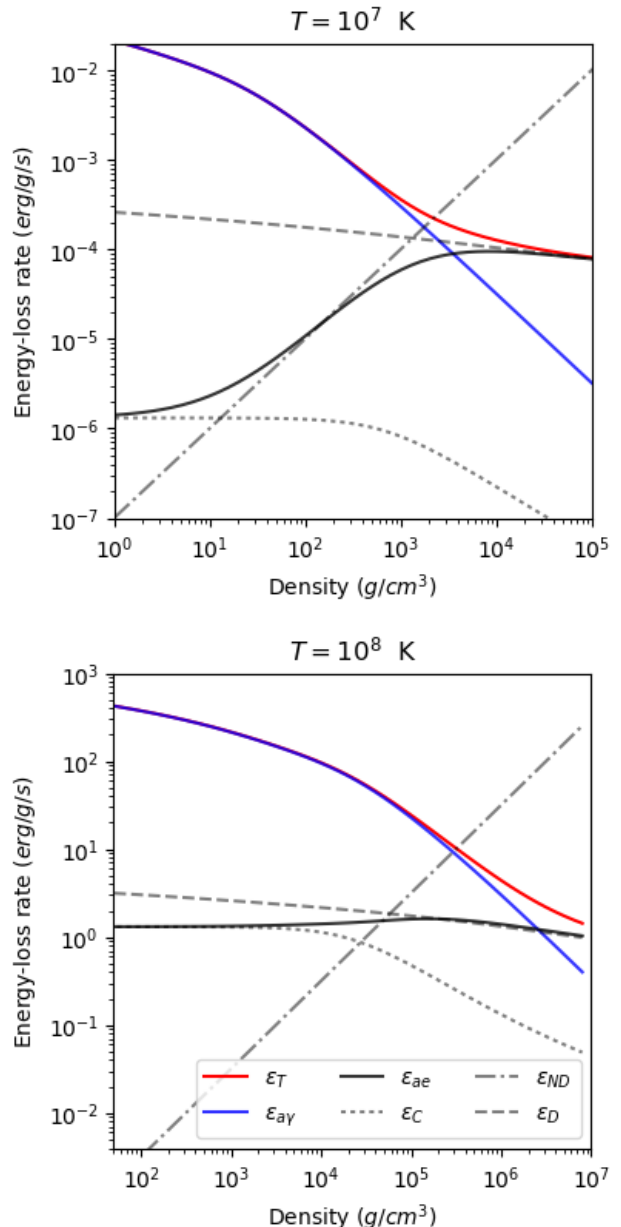


Figure 2.11: Energy-loss rates with respect to density in a helium core at typical temperatures before (top) and at (bottom) the conditions for HeCB. A coupling of  $g_{10} = g_{13} = 1$  is considered for the axion-photon and axion-electron processes respectively. The rates are defined in Sections 2.4.1 and 2.4.2 with  $\epsilon_T$  as the combined rate due to both coupling to photons and electrons.

Consider a stellar plasma of helium composition ( $\mathcal{Z} = 2$  and  $\mathcal{A} = 4$ ). Figure 2.11 shows the energy-loss rates for axion Primakoff, Compton and bremsstrahlung processes using the equations in Sections 2.4.1 and 2.4.2. Considering a constant temperature of  $10^7 \text{ K}$ , of the order of an RGB stellar core, typical central densities of  $10^5 \text{ g cm}^{-3}$  show a relative dominance of axion-electron processes (specifically the degenerate bremsstrahlung case). The energy-loss here is of the order of  $10^{-4} \text{ erg g}^{-1} \text{ s}^{-1}$  which is ten times that of standard neutrino processes [27]. At this stage

of stellar evolution one might be able to constrain the coupling of axions to electrons. Notice that the axion-electron energy-loss dominates in the core, where g modes propagate (see Section 2.2). Therefore, one might expect any effects of axion-electron coupling to emerge in measurements of  $\Delta\Pi$ , particularly on the low-luminosity RGB or RGB bump.

On the contrary, at core temperatures of  $10^8$  K the energy-loss picture inside the star is considerably different. Here, the Primakoff process dominates for all densities up to  $10^6 \text{ g cm}^{-3}$ . The energy-losses here are of the order of, and somewhat exceed, those expected from standard neutrino physics [27]. Crucially, losses here become import when approaching helium ignition.

As stars of  $0.8 M_\odot$ – $1.8 M_\odot$  ascend the RGB, hydrogen shell burning increases the mass of the degenerate helium core and it contracts via the relationship  $R \propto M^{-1/3}$  [30]. In turn, this releases large amounts of gravitational binding energy of the order of  $100 \text{ erg g}^{-1} \text{ s}^{-1}$  [31]. Novel energy-loss rates approaching or exceeding this value result in a delay in the helium flash, further increasing the core mass. Figure 2.11 shows core energy losses of  $10 \text{ erg g}^{-1} \text{ s}^{-1}$  for a coupling of  $g_{10} = 1$  in the conditions approaching the He flash. Since  $\epsilon \propto g_{10}^2$ , a coupling of  $g_{10} \gtrsim 3$  or  $g_{13} \gtrsim 10$  would result in a helium ignition delay. These impose upper bounds on the couplings in stars of mass  $M \lesssim 2 M_\odot$  because the core mass requirement for helium burning is approximately  $0.45 M_\odot$  [5]. Therefore, any significant delay in helium ignition would increase this value until it becomes unphysical. However, RGB luminosity scales with core mass,  $L \propto M_c^6$  for  $M_c \lesssim 0.5 M_\odot$  [5] thus very small changes in  $M_c$  could be picked up in the luminosity of the RGB tip.

# Chapter 3

## Methods

### 3.1 Introduction to MESA<sup>B</sup>

The stellar evolution models produced for this project were made using the computational environment MESA [32], written in Fortran 95.

Using sensible starting conditions, MESA attempts to solve a series of differential equations, including structural and energy production relations (see Equations 2.1– 2.4). These allow the evolution of a star to be accurately modelled, however there are a number of important caveats that one must be aware of:

- Stars are spherical (some hyper-rotating stars are highly ellipsoidal).
- The stellar interior acts and can be described by conventional fluid equations.
- The star is isolated with respect to its surrounding environment, such that it can evolve without external influencing factors: only binaries with sufficient separation can be deemed to meet this criterion.
- All other forces except gravity are ignored (i.e. influence of B-fields are considered negligible), and unless stated, the star is non rotating.
- Any star is static over its free-fall timescale.
- All regions are in thermal equilibrium (not applicable to the coronal region of the atmosphere).

All simulations are controlled using files called in-lists, which provide all the initial parameters, evolution controls and stopping conditions. The modular nature of the program allows for additional parameters and custom scripts to be added in order to refine and improve the stellar models.

#### 3.1.1 Stopping Conditions

Initial tests on a solar mass star took far longer than anticipated, taking many hours to complete. Upon inspection of the output file, the vast majority of the model consisted of the latter stages of the stars evolution; in particular the TP-AGB stage. This is because this period of evolution is extremely complex to model

due to the periodic changes in the structure of the star over relatively short timescales, as illustrated in Figure 2.7. Consequently, it was desirable to provide conditions in the MESA inlist that would halt the model one a certain condition had been satisfied.

The first potential condition available was based upon when the first TP occurs. Given the fact the definition of this criterion was not exactly clear when this was satisfied, being based on the positions of the shells, it was decided it would be more appropriate to develop our own conditions.

```
stop_at_TP = .true.
```

Ultimately, it was decided the most appropriate choice would be to define a condition where the core helium fraction drops below  $10^{-3}$ . This would stop the star as it begins to ascend up the AGB, and was more effective than the TP condition, since it shortened each simulation by around 30 mins.

```
a_central_lower_limit_species(1) = 'he4'  
xa_central_lower_limit(1) = 1d-3
```

Since there were stages where a large number of models needed to be output relatively quickly, this time saving was an important consideration to make. Nonetheless, the TP condition was retained as a fail-safe for the unlikely situation the primary one failed.

### 3.2 Modifying MESA<sup>D</sup>

The stellar evolution package, MESA [32], allows for implementation of additional routines. Examples of this could be to test new element diffusion mechanisms, the formation of black holes, or additional cooling mechanisms within the star. The latter might arise from non-standard physics such as neutrino dipole-moments or, in the case of this report, axion production.

In order to test the validity of the MESA additions, energy-loss rates for each process implemented is output to the profile and history data files. This also allows the user to see where the energy-loss dominates in the star and how it changes with evolution.

#### 3.2.1 Implementing the Primakoff Process

Implementing the additional energy-losses due to coupling of axions to photons through the Primakoff process requires an extra to the `other_neu.f` MESA routine. This is written by Friedland et al. (2013) [26] in the MESA test-suite. Upon closer inspection, a mistake in the routine is found and corrected [33]. In Friedland et al. (2013) [26], Equation 2.41 is approximated to  $\langle \mathcal{Z}^2 \rangle$ ,

```
axionz2ye = z2bar + ye
```

rather than  $\langle \mathcal{Z}^2 \rangle / \langle \mathcal{A} \rangle$ ,

```
axionz2ye = z2bar/abar + ye
```

leading to a factor of 4 difference to the term for a helium composition, and more so for subsequent burning phases.

The approximations to Equations 2.38 and 2.41 are made because MESA allows access to the values of  $\langle \mathcal{Z} \rangle$ ,  $\langle \mathcal{Z}^2 \rangle$  and  $\langle \mathcal{A} \rangle$  for each mesh point.

### 3.2.2 Implementing Axion Coupling to Electrons

Energy-loss via axion-electron Compton and bremsstrahlung are added to the `other_neu.f` routine in MESA. The stellar evolution modules allow access to the temperature, density, composition, and average atomic number and mass for each mesh point in the star. The value for axion-electron coupling,  $g_{13} = g_{ae} \times 10^{-13}$ , is set by the user in the MESA `inlist` file. Using the equations in Section 2.4.2, the energy-loss rates are calculated and combined using the interpolation formula in Equation 2.51. See Appendix A.1 for more details on the additional MESA routine and suggested improvements.

## 3.3 GYRE<sup>G</sup>

To investigate the effects of axion cooling on the frequency and period spacings of our stellar models, the individual mode frequencies of harmonic degree  $l = 0$  and  $l = 1$  were required. These were calculated using GYRE, an open source stellar oscillation code. GYRE solves stellar pulsation equations using the Magnus Multiple Shooting scheme, as described in detail by Townsend and Teitler [34]. Shooting schemes consider initial value problems from grid points and integrate across small regions in opposite directions. The difference between these solutions is quantified by a discriminant function of frequency  $D(\nu)$  which becomes zero when the integrations match. Roots of this discriminant correspond to modes of the stellar model. Whilst GYRE is capable of solving non-adiabatically, we will consider the adiabatic solutions for the purposes of this investigation.

### 3.3.1 Running GYRE

Running GYRE requires a stellar model, which can be produced by MESA for each profile output. The options and parameters of the run are then defined by several Fortran namelist groups in a namelist input file. The full list of options for these namelists is given in the GYRE documentation [35], and an example of the namelist input file used in this investigation can be found in Appendix A.2.

In this example, the model is defined in the ‘model’ namelist and options for the outer boundary condition, numerical difference scheme and output file options are determined in the ‘osc’, ‘num’ and ‘ad\_output’ respectively. Two ‘mode’ namelists are defined to calculate  $l = 0$  and  $l = 1$  modes respectively. As defined by the tags, each of these modes has a ‘scan’ namelist which

determines a set of points in frequency space to scan for changes in the sign of the discriminant, indicating a root to be solved for between those frequencies. Since  $l = 0$  modes are purely radial the grid type is spaced linearly in frequency. As g modes cannot couple with these p modes there are significantly fewer modes than found in  $l = 1$  and hence fewer grid points are required. In contrast,  $l = 1$  modes are affected by g modes and hence the grid is spaced uniformly in period and has significantly more points. The final namelist of significance is the ‘grid’ namelist which defines the minimum number of points per wavelength to be added in important regions of the spatial grid during the grid refinement process. These additional points are significant for seeing high-order p and g modes as the waveform can vary rapidly.

With the options set by the namelist input files, a GYRE run begins by constructing the spatial grid, on which the pulsation equations are solved. This is based on the underlying grid of the stellar model, with points spanning a range of the fractional radius. Additional points are then added considering the ‘grid’ namelist parameters. Points are added near the centre of the star by considering the inner turning point  $x_{turn}$ , where the wavefunction changes from oscillatory to evanescent. This is considered with the parameter  $n_{inner}$  to set a target grid spacing as follows [36],

$$\Delta x_{targ} = \frac{x_{turn}}{n_{inner}} \quad (3.1)$$

Points are then added between the minimum spatial point and  $x_{turn}$  until the required spacing is achieved. Since the position of  $x_{turn}$  depends on the oscillation frequency of the mode, which is the unknown we are trying to find for each mode, GYRE considers  $x_{turn}$  for each of the frequencies in the frequency grid then uses the minimum value to calculate the target spacing, and the maximum value when establishing the interval to add points to. To add points throughout the rest of the star, further target spacings are considered as follows,

$$\Delta x_{targ,osc} = \frac{2\pi}{\alpha_{osc} \times Re\{k_r\}} \quad (3.2)$$

$$\Delta x_{targ,exp} = \frac{2\pi}{\alpha_{exp} \times Im\{k_r\}} \quad (3.3)$$

where  $\alpha_{osc}$  and  $\alpha_{exp}$  are constants defined in the ‘grid’ namelist and  $k_r$  is the local radial wavenumber. The smallest of these target spacings is taken and points are added across the range of the spatial grid until the required spacing is achieved. Similarly to when adding the inner points, the values of  $Re(k_r)$  and  $Im(k_r)$  depend on the oscillation frequency and hence the maximum value for each from the frequency grid is considered.

With the spatial grid established, GYRE implements the Magnus integrator, calculating fundamental solutions for each subinterval. Next, it scans through the frequency grid searching for sign changes in the discriminant, thus providing initial guesses for the discriminant roots. The pair of points with opposite signs

are then passed on to the root-finding routine, determining the frequencies of the modes. GYRE then reconstructs the eigenfunctions of each eigenfrequency and classifies them by considering their acoustic and gravity wave winding numbers. For further information on GYRE see Townsend and Teitler [34].

### 3.3.2 Limitations

For the purpose of this investigation it was important to produce modes of continuous radial order so that frequency and period spacings could be calculated easily. Since  $l = 0$  modes are purely radial, and hence are unaffected by g modes, there are only of the order of 10 for each star. Being evenly spaced in frequency they are easily distinguishable, making continuous radial order trivial. However, there are many more  $l = 1$  modes due to coupling between p and g modes. Also, due to the g modes which are far denser, they are roughly evenly spread in period, making the required spacing of grid points significantly smaller to distinguish all roots/changes of determinant sign at low frequencies.

Late evolution RGB stars caused significant issues with GYRE due to the density of g modes, and hence the number of mixed  $l = 1$  modes. To distinguish the many modes and produce continuous radial order required a large number of grid points, thus increasing the computation time. This could extend so far as to cause GYRE to crash due to data being stored for too many points, overloading the memory. Dense g modes also caused issues with mode classification, further ruling late evolution RGB stars out of consideration for this investigation. Erratic mode classification also occurred for RC stars which had not undergone the helium flash, in this case being due to the convective core. For these reasons, our use of GYRE was limited to investigating post helium flash RC stars and low luminosity/early evolution RGB stars.

### 3.3.3 Using the Outputs

Using inlists of the form found in appendix A.2, as described in Section 3.3.2, summary files were produced for profiles of specific stars, producing modes with continuous radial order. These modes have been used to investigate the effects of axion-photon and axion-electron cooling on the frequency spacing, period spacing and p and g mode coupling.

For each mode an individual mode file was also produced, providing a number of parameters as a function of fractional radius. Amongst these outputs, the radial displacement perturbation and the horizontal displacement perturbation allow for the effects of p and g components of mixed modes to be plotted as shown in Figure 3.1 and 3.2.

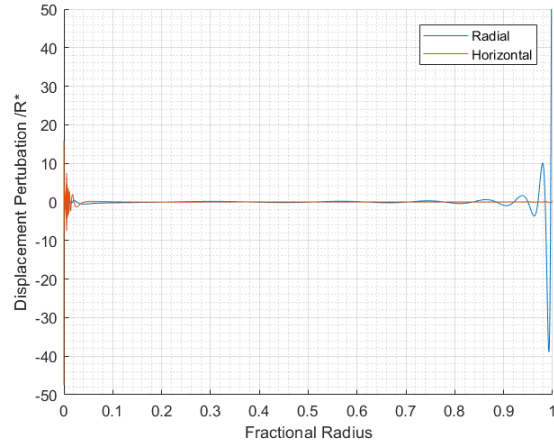


Figure 3.1: Full linear plot of radial and horizontal perturbations of the highest frequency  $l = 1$  mode calculated for the axion-electron cooled model of KIC 03744043, with radial order  $-75$ . Considering the full radius shows the dominance of g mode in the inner region and p mode near the surface of the star.

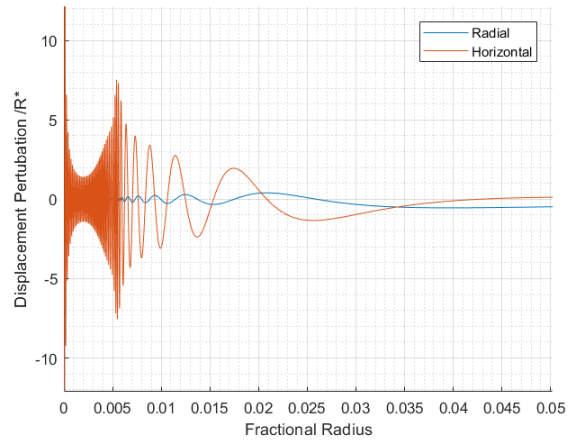


Figure 3.2: Reduced linear plot of radial and horizontal perturbations of the highest frequency  $l = 1$  mode calculated for the axion-electron cooled model of KIC 03744043, with radial order  $-75$ . Looking more closely for small fractional radii reveals the structure of the g mode contribution as well as the appearance of the evanescent region with both horizontal and radial perturbations, just after the dense g mode structure.

An additional output of the individual mode files is the propagation type which suggests at which fractional radii the mode acts as a p mode, g mode or is evanescent. Whilst this offered a potential tool for determining the size of the evanescent region, an explanation of this output could not be found and modes were implied to have multiple evanescent regions which could not be explained. For these reasons, this output was not used to determine the size of the evanescent region.

## 3.4 Data Trimming<sup>E</sup>

By examining the HRD of multiple evolutionary tracks with overlaid asteroseismic parameters (see Section 4.1), the motivation for trimming certain parts of an evolutionary track became clear. This is because early evolutionary stages of higher mass stars would overlap later evolutionary stages of lower mass stars in the luminosity-temperature plane. Therefore, there was a requirement to trim off the pre-MS and post-TRGB stages of evolutionary tracks in order to keep the sections where asteroseismic parameters were overlaid (namely upon the RGB) clear and distinct.

In addition to this, motivation for the ability to trim data sets came from the desire to analyse certain stages of stellar evolution in isolation, such as the RC and the SGB. Therefore, a generic python module of trimming functions was produced which could trim any MESA data set into four distinct sections: MS, SGB, RGB, post TRGB. The pre-MS data was regarded as not useful for examining the effect of axion-cooling and so was neglected. The set of conditions to trim the data for are described and justified in Section 3.4.1. An example plot demonstrating how an evolutionary track could be split into these four sections is shown for a  $1.0 M_{\odot}$  MESA model in Figure 3.3.

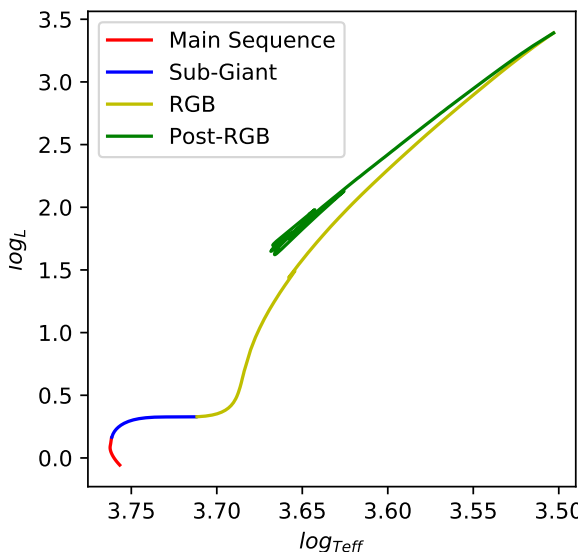


Figure 3.3: Evolutionary track for a  $1.0 M_{\odot}$  star, split into four evolutionary stages based upon our data trimming script.

Other sections of data that required isolating included purely the RC (i.e. without the inclusion of helium flash data) and the RGB bump. These separations were not included in the trimming module but were instead created within the scripts that required these data sets. This is because the conditions used to isolate these sections (see Section 3.4.1) are also satisfied in other places along an evolutionary track, therefore requiring the data sets to be initially trimmed

before applying these extra conditions to them. An example of this is the turning point of luminosity, as used for the RGB bump isolation.

### 3.4.1 Justification of Data Trimming Parameters<sup>M</sup>

#### Main Sequence

During the MS, hydrogen is fused to produce helium in the core of a star. In order to trim the Pre-MS section of the evolutionary track, which was not required for any analysis, we decided to use the “center\_he4” column output from MESA, as there will be helium in the core of a MS star due to fusion of hydrogen. The MESA models have been run under the assumption that the stars have solar composition, which has initial helium mass fraction  $Y = 0.27997$  [32]. Therefore, during the MS, when hydrogen core burning has begun, the helium core mass fraction will be greater than this initial value. It is not clear at exactly which value of helium core mass fraction that the star can be considered to be on the MS, therefore a conservative estimate of 0.5 was made. It is likely that the actual value of this could be lower, somewhere in the range of 0.3–0.5, however no literature could be found to confirm a value meaning that estimates had to be used.

#### Subgiant Branch

The SG stage of the evolution of a star is notoriously difficult to differentiate from the MS and RGB. The beginning of the SG branch occurs as the star leaves the MS, which happens as the star is depleted of hydrogen in the core. For this reason, the end of the MS was defined as when the central hydrogen mass fraction dropped below an arbitrarily low value, which was picked as 0.001. At this value, it can be safely assumed to a reasonable degree of accuracy that the hydrogen fusion process in the core has ceased.

#### Red Giant Branch

The RGB of the evolutionary track follows on from the SGB. As previously mentioned, the difference between an SGB star and a RGB star is somewhat vague. The definition we have adopted to decipher between the stages uses the core degeneracy of the star. MESA simulations define a star as a SG when it reaches a core degeneracy value of 4 eV, as at this value the electron degeneracy has increased the electron pressure to twice that of an ideal electron gas [32]. To confirm this, a plot was created using MESA data for core degeneracy and luminosity over time, shown in Figure 3.4.

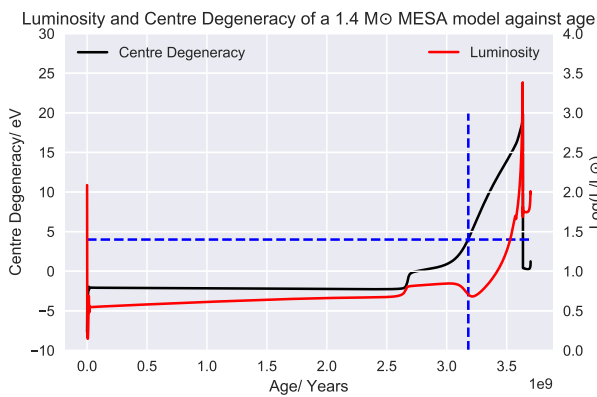


Figure 3.4: Plot showing how the centre degeneracy (black) and luminosity of the star (red) vary throughout the lifetime of the star

In Figure 3.4, a dotted horizontal line is drawn at the core degeneracy value of 4 eV. At the time at which core degeneracy reaches this dotted line, a secondary vertical line is plotted to show the corresponding value of luminosity. At this point, the dotted vertical line crosses near the bottom of the characteristic dip in luminosity seen at the end of the SG phase. This shows that this core degeneracy condition is a sufficiently accurate method of splitting the two evolutionary stages.

### Post-RGB

The period of the evolutionary track after the tip of the RGB is where the RC can be found. This section of the evolution is relatively simple to define, the TRGB is the point at which the star reaches its peak luminosity of the simulated life cycle, as the simulation is stopped at the start of the AGB. Therefore, the Post-RGB is defined as any part of the evolutionary track that occurs after the peak of the stars luminosity.

The accuracy to which the evolutionary stages of the models are split by these parameters was not the highest priority when creating this script; it was most important to ensure that the method of splitting each model was consistent throughout, in order to make each of the models comparable with each other.

## 3.5 Comparing the RGB bump and RC luminosity

### 3.5.1 Locating the RGB Bump and RC in MESA models<sup>M</sup>

In order to produce a plot that compared the luminosity of a star during the RGB Bump against its luminosity on the RC, the data for these stages must be selected from each model in a consistent way. To select a typical RGB Bump star, our trimming module was first used to refine the data to only the RGB, which is where the RGB Bump is found [7]. To then isolate the RGB Bump, a script was created that would output the model at which the luminosity of the RGB

first stops decreasing, as the RGB Bump occurs at this dip in luminosity. This method consistently finds the beginning of the RGB Bump for every model.

To find the luminosity of the RC, our data trimming script was again used, this time refining the data to the Post-RGB. At the beginning of this phase, the star undergoes helium flashes, which cause erratic surges in luminosity. After these flashes have finished, the star remains at an approximately constant luminosity for the majority of its lifetime on the RC, which is shown by a graph of the RC luminosity over time in Figure 3.5.

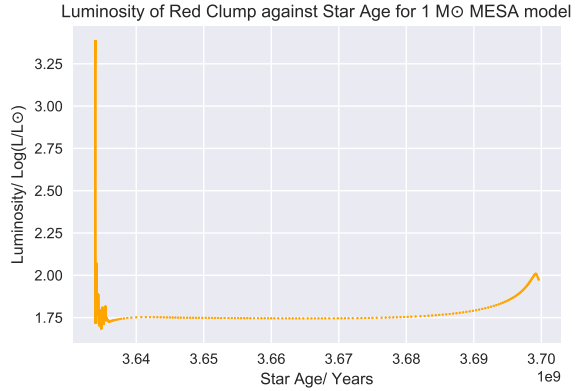


Figure 3.5: Plot showing the luminosity of the RC of a MESA model against the age of the star

As the star spends most of its RC lifetime at this near-constant luminosity, this was a valid assumption to make for the RC luminosity of the models. Therefore, to locate the typical RC luminosity, a script was written to eliminate the helium flashes from the Post-RGB data set. It was noticed that after the helium flashes in any given model, the central carbon fraction of the star exceeded approximately 0.11 for the only time in the star's evolution. Using this information, the model at which the central carbon fraction first reaches this limit was output, and the luminosity of this model was used as the typical RC luminosity.

### 3.5.2 Estimating the Luminosity of the RGB Bump<sup>F</sup>

The luminosity of the RGB bump is difficult to estimate from observational data, therefore an estimation must be made through a different method. Using the TRILEGAL code, a synthetic population of stars was produced with a magnitude limit of  $V \leq 18$  in a  $10 \text{ deg}^2$  field centred around the galactic coordinates  $(l, b) = (90, 20)$  [37]. To produce a reasonable estimate of the luminosity, initially 20 different simulations were run, which was then increased to 100 simulations, with the same initial parameters described above. Combining these populations provided a sample of 3.6 million stars in total, allowing for more certain conclusions to be made.

After analysing a HRD, the effective temperature, luminosity and masses of the population stars were con-

strained and a condition applied to the full length data set in order to reduce the stars down to only RGB and RC stars. The distribution of stars in the simulation can be seen as a histogram with 1000 bins in Figure 3.6.

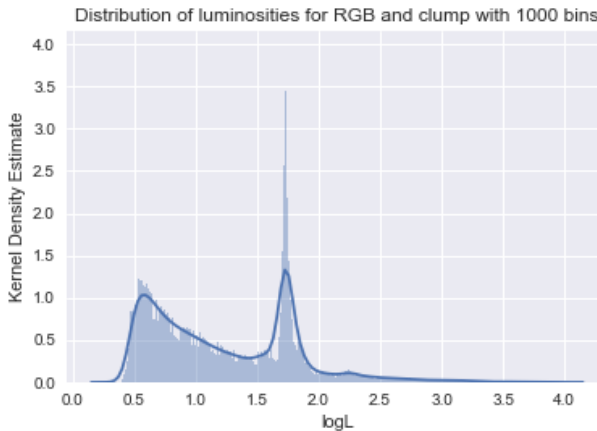


Figure 3.6: Histogram with 1000 bins demonstrating the luminosity of the RGB and RC stars as well as a Kernel Density Estimate (KDE) overlaid. The y-axis is scaled so that the area under the KDE is equal to 1.

The significant peak at a value of  $\log L \approx 1.7$  dex represents the RC stars within the population, with the smaller peak at a slightly lower value of  $\log(L)$  representing the RGB bump stars. The population was then reduced to just these stars in order to provide an estimate for the luminosity of the RGB bump. As the stars are distributed in an approximately normal way, the value of the mean was used as the value of Bump Luminosity,  $L_{\text{Bump}}$ , with the standard error on the mean being used to provide a value for the uncertainty. This returned a value  $L_{\text{Bump}} = (1.5854 \pm 0.0003)$  dex.

### 3.5.3 Estimating RC Luminosity from Observed Data

The luminosity of the RC has already been subject to a fair amount of research, as such observational values of the absolute magnitude of the red clump are available to us. The K-band absolute magnitude of the RC has been subject to previous research and is currently quoted as  $K_s = -1.61 \pm 0.01$  [38]. The equation used to convert this magnitude to a luminosity was Equation 3.4.

$$\log_{10}\left(\frac{L}{L_\odot}\right) = \frac{\mathcal{M}_{\text{bol}} - \mathcal{M}_\odot}{-2.5} \quad (3.4)$$

where  $L$  and  $L_\odot$  are the luminosities of the star and Sun respectively,  $\mathcal{M}_{\text{bol}}$  is the bolometric corrected magnitude of the RC and  $\mathcal{M}_\odot$  is the magnitude of the Sun. All magnitudes are in the K-band. The bolometric correction used to obtain  $\mathcal{M}_{\text{bol}}$  is quoted in [38], as well as the uncertainty which was propagated through equation 3.4.

This method returned the RC Luminosity  $L_{\text{Clump}} = (1.700 \pm 0.041)$  dex, which is a reasonable estimate

with a realistic observational error.

## 3.6 Effect of Axions on the TRGB<sup>C,J</sup>

Stars of mass less than  $2.0 M_\odot$  on the RGB have a degenerate helium core, with hydrogen fusion taking place in the shell. This deposits even more helium into the core, causing it to contract. As this happens, the density of the shell increases causing fusion to occur more efficiently, and the luminosity to increase. Eventually the temperature and density of the core are great enough to ignite helium burning in the core, known as the helium flash. As the helium ignition occurs when the mass of the degenerate core reaches a certain mass and temperature, the TRGB is used as a standard candle because it is a consistent luminosity and as such is a consistent and reliable point in stellar evolution to search for the effects of axion cooling.

The additional energy loss mechanism that the axion cooling provides would lead to a detectable change in the TRGB. Since the degenerate helium core loses energy when axions escape, it takes longer for the core to reach the critical temperature and density required for helium burning to ignite. As more and more helium is deposited in the core by the hydrogen-burning shell, the core contracts and the density of the shell increases. This increases the rate of fusion and thus the star continues to get brighter. With the contraction of the core, the outer layers of the star expand and cool, leading to a drop in the effective temperature. Consequently, the RGB is extended to cooler and brighter stars with the additional axion cooling.

Globular clusters represent a collection of stars with similar composition, metallicity, age and RGB mass due to their approximately simultaneous formation. This makes them good targets to compare with theoretical evolutionary tracks computed in MESA. By comparing the TRGB observed in a cluster with MESA evolutionary tracks under the influence of varying degrees of axion cooling, constraints can be placed upon the axion-photon coupling strength.

## 3.7 Frequency & Period Spacing Investigation<sup>B</sup>

One method of distinguishing different periods of stellar evolution is to plot the asymptotic period spacing  $\Delta\Pi_1$  against large frequency spacing  $\Delta\nu$ . In essence, such a graph can act as an asteroseismic analogue to the HRD, since these two parameters are also affected by changes in the mass, metallicity and compositional parameters. An example of such a graph is shown in Figure 3.7.

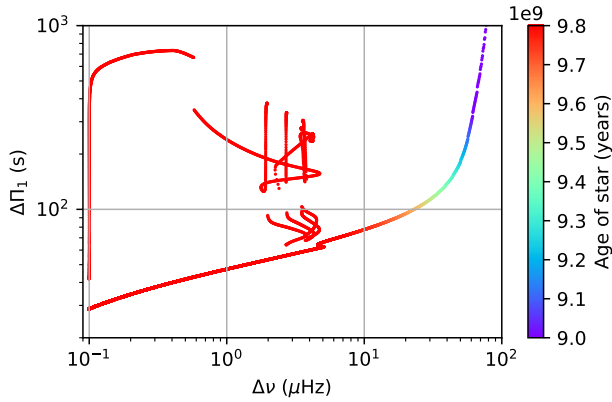


Figure 3.7:  $\Delta\Pi/\Delta\nu$  spacing graph for a star of solar mass and composition, showing the large contribution from the more evolved stages of evolution.

The main omission from such a graph is the MS, since they have no observed g mode oscillations (see Section 2.2). As the star evolves on to the SGB and RGB, it traces out a curve along the bottom of the graph, with decreasing  $\Delta\Pi$  and  $\Delta\nu$  as time progresses. Upon reaching the helium flash, the period spacing shoots up and the resulting pulses during this short stage of evolution are the cause of the rather disjointed set of curves in the centre of the figure.

### 3.7.1 Isolating the RC

The evolutionary splitting script developed earlier in the project was unfortunately insufficient to correctly cut out stars in the RC, since both the helium flash and the initial ascent of the AGB would otherwise be included in the data. It was therefore necessary to find and develop new conditions to avoid this problem. The first stage of narrowing the data was to apply a criterion based upon the time-step used by MESA between successive models. During more complicated phases of stellar evolution, MESA has to decrease the time passed between each model in order to maintain an accurate simulation; applying a cut-off of  $\log(dt) \geq 5$  retained the SGB, early RGB, RC and start of AGB ascent. Hence another value would be needed to separate the the start of the AGB track from the rest of the RC. An investigation of the history files lead to the discovery that the fractional core  $^{16}\text{O}$  content was a reliable method of cutting the data; applicable across the mass range considered. This arguably provided a more discernible cut-off in the data than the He and  $^{12}\text{C}$  fractions because it increased at a far higher rate and started from a negligible amount following the helium flash (carbon had already started increasing during the that period). A maximum fraction of 0.25 was applied, a value that correlated closely to when the core He fraction decreased below 0.2 [10].

The application of these aforementioned criteria provided a consistent method of confidently selecting the region of the evolutionary tracks that corresponded to the RC. An example set of tracks without any modelled axion cooling is shown in Figure 3.9

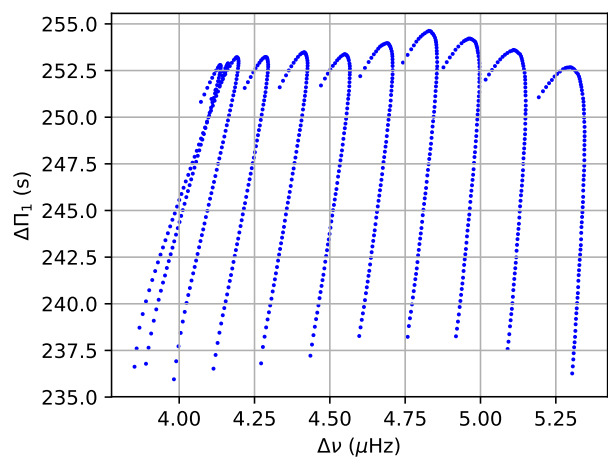


Figure 3.9: RC evolutionary tracks for masses between  $0.8 M_\odot$ – $1.8 M_\odot$ . Tracks increase left to right in  $0.1 M_\odot$  steps.

### 3.7.2 Core Overshooting

Using the methods applied in Section 3.7.1, models were then produced in order to attempt to replicate observations made of real stars. However, when models produced to simulate a cluster in the study by Bossini et al (2017) [39] were compared, it was abundantly clear that there was a discrepancy between our calculated models and observational data — Figure 3.10 shows that this is likely accounted for due to the lack of any mixing regime in our models.

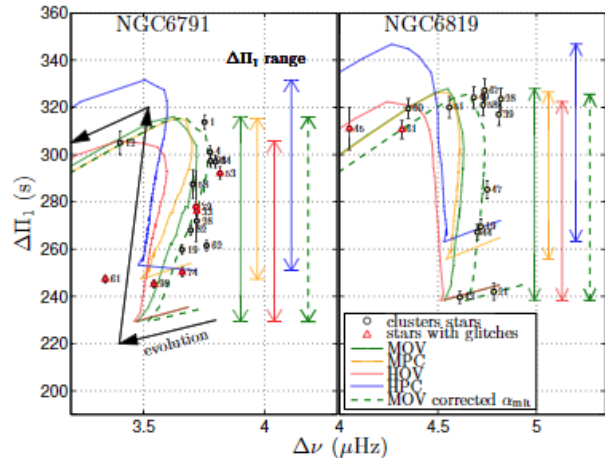


Figure 3.10: Period-Frequency spacing plot for two observed clusters of stars, showing different mixing schemes used in MESA to match the data [39].

By default, MESA uses a Bare Schwarzschild model (described fully in Straniero et al. (2003)[10]), where the convective core is not allowed to grow in mass during the HeCB phase. This is not a particularly accurate representation and there are a number of potential mixing schemes that help to overcome this issue.

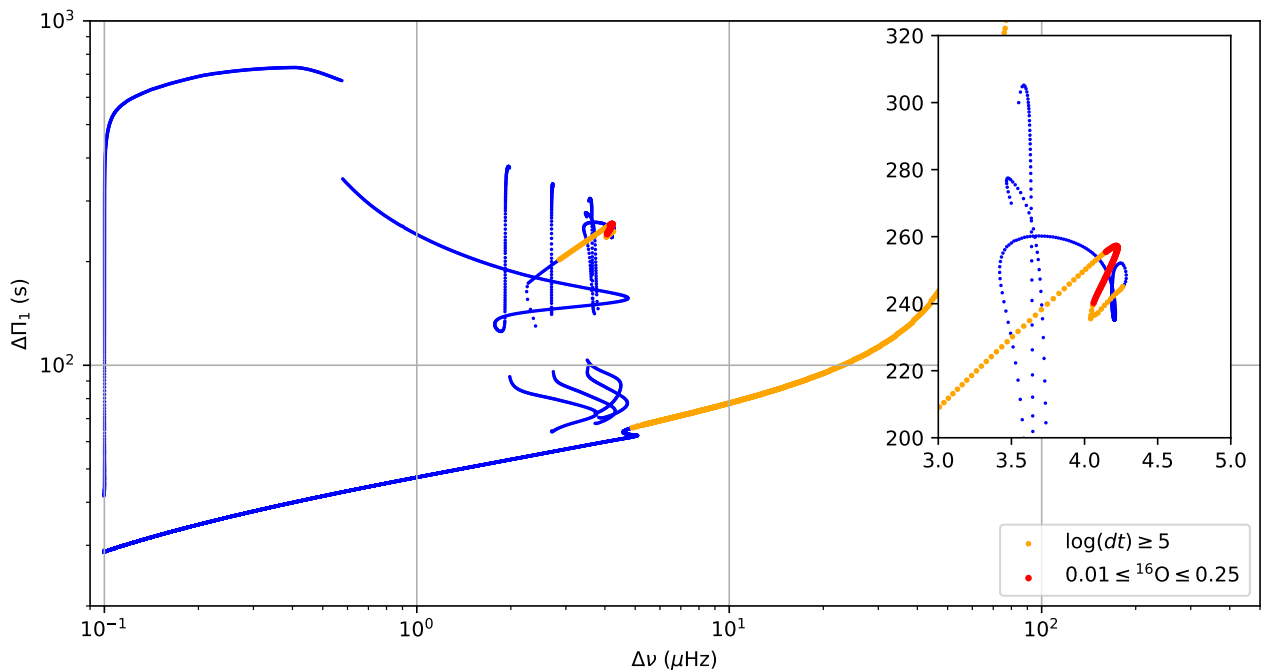


Figure 3.8: Regions have been highlighted using two separate conditions to pick out the RC region of the graph, which covers a comparatively small area.

### Implementing a Regime

The principles of core overshooting have already been covered in great detail [40], however the mixing scheme that was subsequently implemented is known as Step Function Overshooting. The scheme is fully described in Bossini et al. (2015) [41]. Nonetheless, a brief summary is as follows: due to inertia, convective elements can have a non-zero kinetic energy when they reach the traditional convective boundary, defined by  $\nabla_{ad} = \nabla_{rad}$  (the balanced state of the Schwarzschild Criterion). As a result, these pockets of gas can overshoot into the radiative zone above the core, introducing mixing into the region. The step function in MESA is defined by a fractional scale height  $f_0$  from the convective-core boundary and an overshooting parameter  $f$ . An excerpt of the controls that were applied to the MESA inlist follows

```
overshoot_f0_above_burn_he_core = 1d-3
overshoot_f0_above_burn_z_core = 1d-3
step_overshoot_f_above_burn_he_core = 0.2
step_overshoot_f_above_burn_z_core = 0.2
```

Three regime variations were tested of varying mixing parameter; notation chosen to be consistent with schemes used in previous studies [39]:

- LOV (Low Overshooting):  $f = 0.2$
- MOV (Moderate Overshooting):  $f = 0.5$
- HOV (High Overshooting):  $f = 1.0$

The location of convective regions in models can be shown by looking at the diffusion coefficients for convective processes, which will be large and positive in

these cases. An example of the effects of introducing an overshooting scheme is shown in Figure 3.11, with the different regions clearly highlighted. The figure represents a star on the RC, and clearly shows the He-burning convective core, overshooting region and also the outer convective envelope.

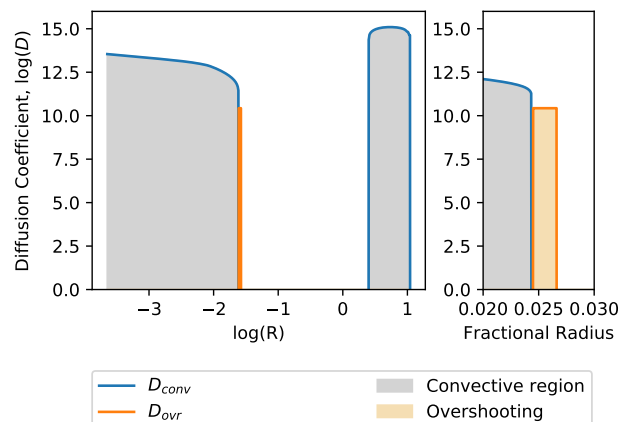


Figure 3.11: Location of convective and overshooting regions for a  $1.4M_\odot$  star on the RC.

### 3.7.3 Available data for $\Delta\Pi_1$ L

Kepler observed about 15,000 RGB stars of which 13,000 displayed solar like oscillations. The asymptotic period spacings ( $\Delta\Pi_1$ ), large frequency separations ( $\Delta\nu$ ) and their corresponding errors for 1142 RGB stars were calculated manually by Mosser et. al. [14] and the separation between the SG, RGB and RC identified on the asteroseismic HRD ( $\Delta\Pi_1$  against  $\Delta\nu$ ). The approximate percentage errors on  $\Delta\nu$  and  $\Delta\Pi_1$  in

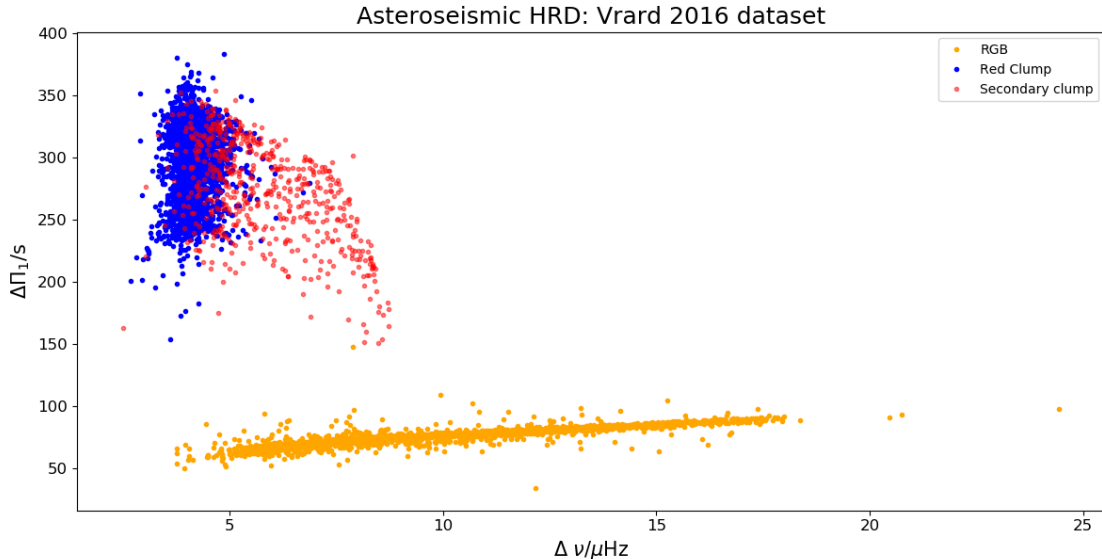


Figure 3.12: Asteroseismic HRD for the full Vrard dataset showing the RGB, RC, and secondary clump stars in the dataset

the RC were identified as 1% and 2% respectively. Unlike the traditional HRD, the asteroseismic HRD allows easier identification between the low luminosity RGB stars and the RC stars, as can be seen from Figure 3.12.

A more recent study by Vrard et. al. [42] used an automated method to calculate  $\Delta\Pi_1$  and  $\Delta\nu$  for 6100 evolved stars, of which 1996 are on the RGB and 3549 are RC stars. This dataset was chosen for the study as it contains more stars, even though it has a higher mean percentage error on  $\Delta\Pi_1$  (2% for the Vrard dataset compared to 1.85% for the Mosser dataset). The errors for  $\Delta\nu$  were not given for the Vrard dataset so the approximate percentage error of 1% on the RC [14] was used.

The masses for the stars given in the dataset were calculated with the scaling relations using the asteroseismic global parameters ( $\Delta\nu$  and  $\nu_{max}$ ) giving an error on the mass of about 10 – 15%. Changing the mass causes a change in  $\Delta\nu$  but no significant change in  $\Delta\Pi_1$  is observed [42]. The metallicities for the stars were obtained from the Kepler Input Catalog [43], to allow for stars of similar composition to be selected as metallicity causes a shift in both  $\Delta\Pi_1$  and  $\Delta\nu$  (see Section 3.8.4). For  $\Delta\Pi_1$ , stars below  $1.2 M_\odot$  display a larger change with metallicity compared to stars above  $1.4 M_\odot$ , where it is negligible [42].

Two old open clusters, NGC 6819 and NGC 6791, were identified by Bossini et. el. (2017) [39]. The Bossini dataset consists of 14 RC stars in NGC 6819 and 16 in NGC 6791. Evolved stars in old open clusters have similar mass and metallicity. These clusters were used to calibrate the value for the axion-photon coupling constant  $g_{10}$ . The full Bossini dataset from which the two clusters were identified, combined the asymptotic period spacings from the Vrard dataset with accurate spectroscopic data [44], to give more accurate

values of mass and metallicities.

### 3.8 Axion cooling in the asteroseismic HRD L

The aim of this study was to identify axion cooling in solar-like oscillators by observing the changes in the asteroseismic parameters -  $\Delta\Pi_1$  and  $\Delta\nu$  with introduction of axion cooling. Evolutionary tracks were created with different HeCB mixing schemes for a range of values for  $g_{10}$  and populated with observed data to determine the track that fit the data best, allowing us to find constraints on the two variables.

A preliminary investigation identified the RC as the region of the asteroseismic HRD where axion cooling was most likely to be detected. Figure 3.13 shows that the tracks for the RC show sufficient spread for the observational data to be able to distinguish between them. The shift of the data to the left of the tracks was identified to be due to the lack of a HeCB mixing scheme being used in creating the models. The RGB on the other hand showed very small deviations in  $\Delta\nu$  and almost no difference in  $\Delta\Pi_1$ . Increased  $g_{10}$  strength is only expected to cause small shifts in  $\Delta\nu$  and since no helium burning takes place during the RGB phase of stellar evolution, introducing a mixing scheme would have no effect on the evolutionary tracks. Consequently the RGB was not investigated further as asteroseismic data of sufficient accuracy to identify the differences between the two tracks is currently not available.

Section 3.8.4 identifies mass and metallicity as two properties of a star which cause significant change in the asteroseismic HRD. Therefore constraints on the mass and metallicity are required to insure the validity of our results. Old open clusters provide robust con-

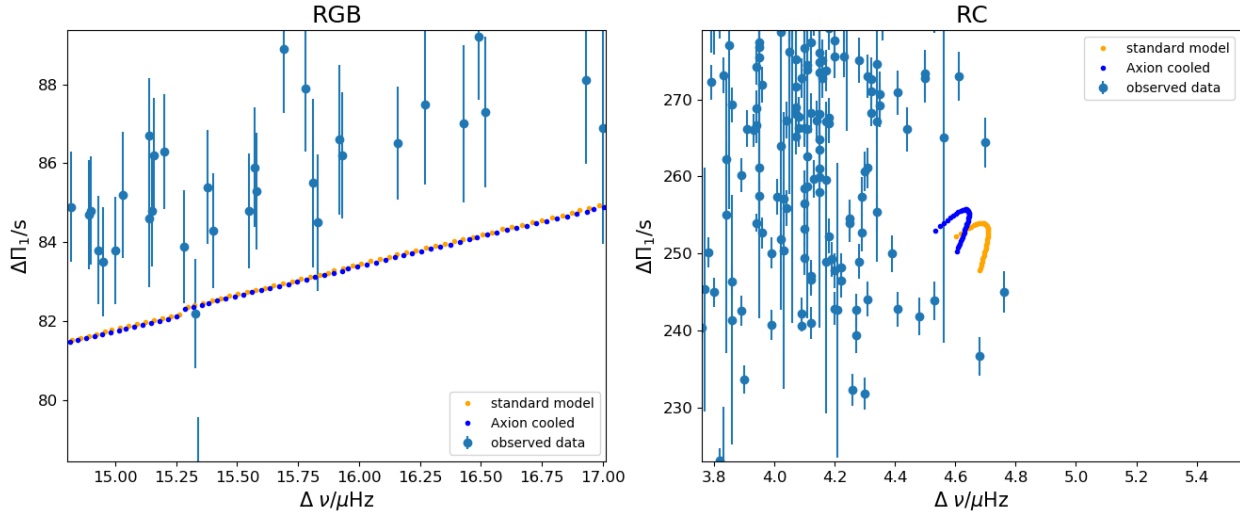


Figure 3.13:  $\Delta \Pi_1$  against  $\Delta \nu$  for evolutionary tracks created with no HeCB mixing scheme for a star with a mass of  $1.4 M_{\odot}$  and solar composition, with and without axion cooling. The tracks are populated with the observational asteroseismic data for  $1.4 M_{\odot}$  stars Vrard et. al. (2016) [42] (a) RGB (b) RC

straints on both for their evolved stars. Using a grid of models, the old open clusters NGC 6819 and NGC 6791 were used to attempt to identify axion cooling and calibrate the value of  $g_{10}$ .

Although open clusters provide an excellent way of constraining the mass and metallicity, fitting models to the data can be unreliable due to the small number of RC stars in open clusters for which the asymptotic period spacing data is available. So larger datasets [39] [42] were used to create synthetic clusters by reducing the data, to identify stars with similar mass and metallicity. This provided us with a larger sample of stars which we used to compare the results that we obtained from our calibration using the open clusters.

### 3.8.1 Modifying the RC trimming parameters

In section 3.7.1, conditions to isolate the RC from the full evolutionary track were investigated. Although the conditions identified ( $\log(dt) \geq 5$  and  $0.05 \leq$  fractional core O-16 content  $\leq 0.25$ ) successfully isolated the RC, we needed to extend the bounds of the fractional core O-16 content ( $0.001 \leq$  fractional core O-16 content  $\leq 0.45$ ) so that the evolution of the star onto and off the RC could be included in the trimmed track. This was required as the early HeCB stars provide robust constraints on fitting the models to the data.

### 3.8.2 Axion-photon coupling constant and HeCB mixing schemes

We implemented three HeCB mixing schemes as detailed in section 3.7.2 - LOV, MOV and HOV. For each of these schemes five tracks with  $g_{10}$  taking the values of 0, 0.33, 0.66, 1.0 and 1.5 were created for each set

of stars with similar mass and composition constrained using our two methods.

### 3.8.3 Calibrating the value of $g_{10}$ using old open clusters

An open cluster refers to a group of stars that was formed from the same molecular cloud and is loosely bound by mutual gravitational attraction. Star formation takes place over a short period of time, before the molecular cloud gets ionised by strong UV radiation from young hot stars and driven away by stellar winds and radiation pressure. This means that members of an open clusters have similar age and metallicity and therefore mass is the only contributing factor to the evolutionary state of a star [45].

Hence open clusters provide excellent constraints on the mass and metallicity for its member stars which are in the same evolutionary state. We used RC stars from two old open clusters - NGC 6791 and NGC 6819, which were identified in Bossini et al. (2017) [39]. Both of these clusters are in the Kepler field of view and have been widely studied.

A model grid was created for each cluster using MESA with varying axion-photon coupling constants and different HeCB mixing schemes. The initial conditions used for the models were the same as used in Bossini et al. (2017) [39]. For NGC 6791, the tracks were created with  $M = 1.15 M_{\odot}$ ,  $Z = 0.0350$  and  $Y = 0.300$  [?] whereas for NGC 6819 the initial conditions for the models were  $M = 1.60 M_{\odot}$ ,  $Z = 0.0176$  and  $Y = 0.267$ .

### 3.8.4 Obtaining Synthetic Cluster Data<sup>1</sup>

Although plots and models have been created for the open clusters NGC 6791 and NGC 6819, it may be useful to take data from datasets and create so-called “synthetic” clusters of stars with very similar masses and metallicities. To create such clusters, it is best to choose ranges of mass and metallicity which have the most number of stars.

Using the Vrard (2016) data [42] containing approximately 6100 evolved stars, a 2-dimensional hexbin histogram can be plotted using the values of mass and metallicity given in the dataset. The dataset gives every star a value for “status”, which defines what stage of evolution each star is in. Initially, the whole data set was reduced by this value to give only RC stars, which have a “status” value equal to 1.

Initially there was a problem that this dataset did not give metallicity values for any of its stars. To obtain these values, the Kepler Input Catalog was used to search for all the stars in the Kepler database and get metallicity values for each[43]. Unfortunately errors on these values were not given however.

Another issue to overcome was converting the metallicity values in the data from  $[Fe/H]$  to  $Z$ . This is necessary as  $Z$  is being used as an input into MESA, and so any data that is to populate any models must have the correct model to fit the data to. To do such a conversion equation 3.5 [46] is used,

$$\log Z = 0.977[Fe/H] - 1.699 \quad (3.5)$$

where  $-1.699$  is equal to  $\log Z_{\odot}$  at the time, which used a value of  $Z_{\odot} = 0.02$ . This equation has changed slightly when used to calculate  $Z$  for the 2D histogram by using a more current value for  $Z_{\odot}$  of 0.0196, which gives Equation 3.6,

$$\log Z = 0.977[Fe/H] - 1.708 \quad (3.6)$$

which can be used to calculate values of  $Z$  for all our data. This new dataset was used to plot a 2D histogram of  $Z$  versus  $M$ , as seen in Figure 3.14.

From this histogram ranges of  $M$  and  $Z$  can be chosen to plot synthetic clusters on appropriate models. Two clusters were chosen from the data, with cluster 1 having masses  $0.99 \leq M_{\odot} \leq 1.01$  and metallicities  $0.0124 \leq Z \leq 0.0144$ , and cluster 2  $1.38 \leq M_{\odot} \leq 1.42$  and  $0.004 \leq Z \leq 0.008$ . Both of these clusters contain 11 stars.

The errors on the masses of each star were also given, so an average percentage error on the mass of each cluster could be calculated. For cluster 1 this was found to be 9.50%, and 5.92% for cluster 2. There was unfortunately no errors for the metallicity, however the metallicites were taken directly from Kepler[43], and these values are thought to be inaccurate. This dataset also gives the errors on the period spacing, however it does not give errors on the large frequency spacing. For these values, a percentage error of 1% was taken from

Mosser 2014 [14]. These values can then be used to populate models with errors on the data.

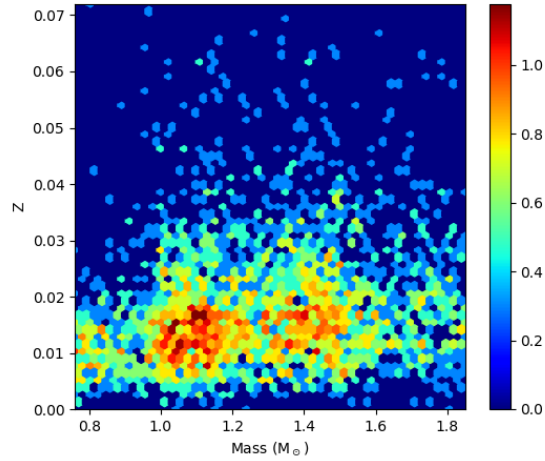


Figure 3.14: 2D hexbin histogram of  $Z$  against  $M$ , with colour indicating frequency. Data was taken from Vrard 2016 [42]

A third cluster was also created from the full data set used by Bossini et al. (2017) [39], with the same mass range as cluster 1, and metallicities of  $-0.3 \leq [Fe/H] \leq 0$ .  $[Fe/H]$  is used here instead of  $Z$  as there are errors for  $[Fe/H]$  in this dataset. This cluster has 28 stars.

The masses in this dataset are more accurate than the ones given in the Vrard dataset [42], with an average percentage error of 8.93% on the masses. Although there are errors on the metallicities, as  $[Fe/H]$  is a log scale a percentage error cannot be directly calculated from these errors. This dataset also gives values for the errors on the large frequency spacing and the period spacing, which can subsequently be directly plotted.

## 3.9 Modelling Low-Luminosity RGB Stars<sup>D</sup>

Seven low-luminosity RGB stars are chosen from the KIC database. Specifically, all seven had been previously modelled accurately by Hernandez et al. (2016) [47]. Using data from the best-fit models, presented in Table 3.1, the models were replicated in MESA [32] with the addition of the axion-photon and axion-electron routines as described in Section 3.2. The standard MESA GS98 metallicity tables and OPAL opacities were used. Additionally, element diffusion is turned on. Alternative mixing schemes are not considered in these models, but could be implemented in future research.

Table 3.1: Initial conditions for the best-fit models as determined by Hernandez et al. (2016) [47]. The uncertainties,  $\sigma$  is relative for the mass,  $M$ , and absolute for the other parameters. The initial values of helium abundance and metallicity are given by  $Y_{ini}$  and  $Z_{ini}$  respectively, and  $\alpha$  is the mixing length parameter.

#	KIC	$M/M_\odot$	$Y_{ini}$	$Z_{ini}$	$\alpha$
1	03744043	1.147	0.272	0.009	1.906
2	06117517	1.198	0.296	0.029	1.916
3	09145955	1.196	0.294	0.009	1.941
4	09475697	1.151	0.296	0.022	1.931
5	09882316	1.393	0.288	0.008	1.862
6	10123207	0.904	0.293	0.009	1.568
7	10200377	0.943	0.273	0.005	1.757
$\sigma$		0.023	0.009	0.003	0.140

Asteroseismic data in Table 3.2 is used to constrain the evolutionary stage of the models to compare with the measurements for each star. The values of  $\Delta\nu_{obs}$  come from Mosser et al. (2012) [48] and  $\nu_{max}$  comes from the peak bagging methods of Corsaro et al. (2015) [49]. In order to recover the asymptotic large frequency spacing  $\Delta\nu_{as}$  the relation,

$$\Delta\nu_{as} = (1 + \zeta)\Delta\nu_{obs}, \quad (3.7)$$

is used, where  $\zeta = 0.038 \pm 0.002$  is determined empirically for the RGB [50]. Using this correction also better determines stellar mass when applying the asteroseismic scaling relations (Equations 2.23 & 2.24) which have been found to overestimate the mass by about 15 % on the RGB [51]. The large frequency spacing is determined with uncertainties of about 0.6 % and the frequency at maximum power has up to 0.2 % uncertainty. These parameters relate directly to the radius of the star through Equations 2.16 and 2.22 so this method is effectively comparing models at a similar radius on the RGB. Theoretically, increased luminosity of the star due to increased nuclear burning is expected to dominate the effects of axion-cooling (see Section 2.4). Therefore, it is appropriate to compare the models at similar radii through the asteroseismic parameters.

Table 3.2: Asteroseismic data for the seven stars considered in Table 3.1. The observed large frequency spacing,  $\Delta\nu_{obs}$  is determined by Mosser et al. [48] and the values for  $\nu_{max}$  are calculated by Corsaro et al. [49]. The asymptotic spacing is independently recovered using Equation 3.7.

#	$\Delta\nu_{obs}$	$\sigma_{\Delta\nu}^{obs}$	$\Delta\nu_{as}$	$\sigma_{\Delta\nu}^{as}$	$\nu_{max}$	$\sigma_{\nu}^{max}$
1	9.90	0.05	10.28	0.06	112.5	0.2
2	10.16	0.05	10.55	0.06	120.3	0.2
3	11.00	0.06	11.42	0.07	131.7	0.2
4	9.88	0.05	10.26	0.06	115.1	0.2
5	13.78	0.07	14.30	0.08	182.0	0.5
6	13.67	0.07	14.19	0.08	160.9	0.2
7	12.47	0.06	12.94	0.07	142.5	0.2

GYRE profiles are output around when the values of  $\Delta\nu_{as}$  and  $\nu_{max}$  are within 5 % of those in Table 3.2

for each star. For every star, the profile with the lowest relative uncertainties from the tabulated values (added in quadrature) is chosen and GYRE is used to calculate the dipole mode frequencies.

Future investigations could consider changing the initial conditions in Table 3.1 for each axion-cooled model in order to best model the star. That way the models can be more consistently compared to the observational data, and with each other. However, this report simply considers keeping all parameters constant and changing the coupling strength to observe its effects independently.

# Chapter 4

## Results & Discussion

### 4.1 Combining Asteroseismology with the HRD<sup>E</sup>

The use of asteroseismology in the investigation for the presence of axions is an entirely new concept, but thanks to advances in the quality of asteroseismic data from Kepler [11] for example, it is now possible. One way is to utilise the method of combining observational asteroseismic data for a single star and stellar models of a range of evolutionary tracks, as described in [52]. This allows an independent estimate of a star's mass and radius to be determined purely from asteroseismology, which is valuable when comparing different estimates since it is derived directly from stellar models. Furthermore, the errors on these values are intrinsically very small because the sensitivity of the asteroseismic parameters and their overlap on the evolutionary tracks is what determines these errors.

An example of how asteroseismic parameters can be combined with a HRD is shown in Figure 4.1, with arbitrary uncertainties on the asteroseismic values (taken from KIC 12008916, see [52]) in order to highlight clearly the overlap and hence ability to determine the mass and radius of a star. Theoretically, these values and uncertainties would be taken from observational data, but due to focusing this investigation elsewhere this was not completed. However, the principle still stands and would be worth investigating in future.

A suggestion for another route of investigation would be to obtain asteroseismic data for a star which has independent mass and radius estimates and produce a plot similar to Figure 4.1 in the first instance with no axion cooling modelled, obtaining an initial estimate for mass and radius. Following this, it would then be beneficial to do the same for a grid of masses with axion cooling and to vary the axion-photon coupling strength and once again calculate the star's mass and radius. If axion cooling is present, this would theoretically be hinted at by the modelled estimates for mass and radius being closer to the independent mass and radius estimates when axion cooling is included, rather than without. Following this, statistical analysis

of the proximity of the various estimates to the independent estimates would help to verify any conclusions about axions, as would analysis into any compensation for the energy loss due to axions from other variables in the models.

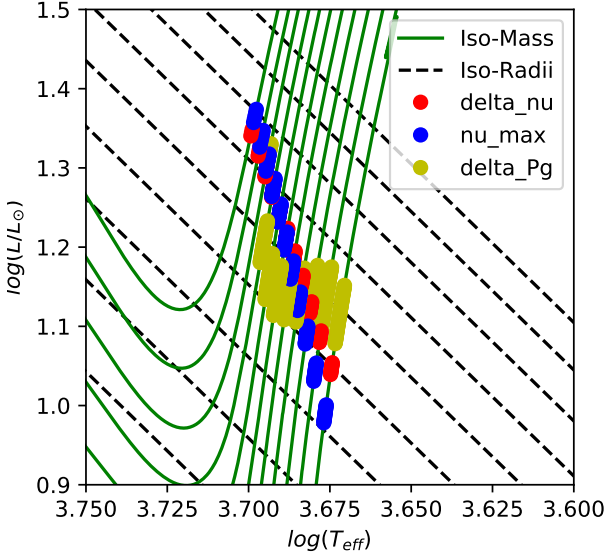


Figure 4.1: Hertzsprung-Russell diagram for eleven evolutionary tracks within the mass range  $1.0 M_{\odot}$ – $2.0 M_{\odot}$  (Right–Left) with overlaid isoradius tracks between the range  $3.0 R_{\odot}$ – $8.0 R_{\odot}$  (Bottom–Top) in increments of  $0.5 R_{\odot}$ . The loci of global asteroseismic parameters  $\nu_{max}$ ,  $\Delta\nu$ , and  $\Delta\Pi_l$ , given to arbitrary precision, are plotted for each evolutionary track. The overlap of all three parameters theoretically provides an estimate for the mass and radius of the star for which those parameters were observed for.

### 4.2 Statistical analysis of MESA output data<sup>N</sup>

In order to thoroughly understand the effects of axion cooling on the models output by MESA, some statistical analysis of the data it produces is necessary.

To quantify the closeness of models to a set of input parameters and the uncertainties on them (these could be for example experimentally determined quantities), a merit function must be defined. If one assumes that a set of multiple measurements of the same quantity are normally distributed due to the random error on each – a common assumption in experimental science – then the natural merit function to use is  $\chi^2$ . This is given by

$$\chi^2 = \sum_i \left( \frac{x_i - o_i}{\sigma_i} \right)^2, \quad (4.1)$$

Where  $o_i$  and  $\sigma_i$  respectively are the values of and uncertainties on the input parameters, and  $x_i$  are the values of the corresponding parameters belonging to

the model for which  $\chi^2$  is being calculated. The use of this as a merit function comes from the probability density function for the normal distribution, which is given by  $f = Ce^{-\chi^2}$  where  $C$  is a constant. The number of input parameters used in calculating  $\chi^2$  for each model is known as the degrees of freedom.

The higher a model's value of  $\chi^2$  is, the further the relevant parameters (i.e. those corresponding to the input parameters) belonging to that model are from the values of the input parameters. The probability of taking a measurement with parameter values between the parameters belonging to a model and the input parameters can be calculated from that model's value of  $\Delta\chi^2$ , which is equal to the model's  $\chi^2 - \chi_{\min}^2$ , where  $\chi_{\min}^2$  is the minimum value of  $\chi^2$  possessed by any model. This is done using the cumulative distribution function of the  $\chi^2$  distribution for the number of degrees of freedom corresponding to the number of input parameters. This calculated probability corresponds to a distance of  $\sigma_{\bar{x}}$  from the mean of a normal distribution <sup>A</sup>.

The calculation of these statistical measures was achieved using a python script. The  $\chi^2$  calculation function takes the input values and uncertainties for an arbitrary number of parameters and uses these to calculate  $\chi^2$  for every model in a model grid.

#### 4.2.1 Quantifying the change in mass and radius with different $g_{10}$ values

A useful statistical analysis to perform is one that can give an estimate on the number of measurements in the vicinity of a certain model (i.e. with similar metallicity, temperature and luminosity) required in order to make a conclusion about the presence of axion cooling from the model data. This analysis requires the consideration of how mass and radius change between the non-axion cooled model grid and the axion cooled model grid when the values of three asteroseismic parameters are held constant:  $\Delta\nu$ ,  $\Delta\Pi_1$  and  $\nu_{\max}$ .

In order to make such an estimate, a model is first chosen from a non-axion cooled grid. The values of  $\Delta\nu$ ,  $\nu_{\max}$ ,  $\Delta\Pi_1$  and  $T_{\text{eff}}$  belonging to this model are recorded. The uncertainties on these quantities are chosen to be  $\sigma\Delta\nu = 0.03\mu\text{Hz}$ ,  $\sigma\nu_{\max} = 0.5\mu\text{Hz}$ ,  $\sigma\Delta\Pi_1 = 1\text{s}$   $\sigma T_{\text{eff}} = 70\text{K}$ . These are estimates based on uncertainties on recent measurements of these quantities found in the scientific literature.

The recorded values and chosen uncertainties on these quantities are then used to calculate  $\chi^2$  and subsequently  $\Delta\chi^2$  for every model in a corresponding (matching input masses and chemical composition) axion-cooled model grid.

A model is found in the axion cooled grid which has the closest mass and radius to the chosen non-axion cooled model. The  $\Delta\chi^2$  value belonging to this model is used to find how far it is from the input parameters in units of  $\sigma$ . This value is equivalent to a distance from

the mean of a normal distribution that has a standard deviation  $\sigma = 1$ , or the error on the mean of a set of  $n$  measurements  $\sigma_{\bar{x}}$ . Using the standard equation for error on the mean and substituting  $\sigma = 1$ ,

$$\sigma_{\bar{x}} = \frac{\sigma}{\sqrt{n}} = \frac{1}{\sqrt{n}} \Rightarrow n = \frac{1}{(\sigma_{\bar{x}})^2}. \quad (4.2)$$

This number  $n$  can thus be thought of as a minimum number of stars with parameters similar to the chosen non-axion cooled model required to observe with the same precision as the input parameters to make a conclusion about axion cooling from the MESA output model grids. The higher  $n$  is, the smaller the difference in mass and/or radius is for constant  $\Delta\nu$ ,  $\nu_{\max}$ ,  $\Delta\Pi_1$  and  $T_{\text{eff}}$  between axion cooled and non-axion cooled model grids at the particular model being considered. As such a higher number of observations would be needed to make a judgement about axion physics in that region. Figure 4.2 shows a visualization of this method: the axion cooled RGB is plotted which has had  $\chi^2$  calculated using  $\Delta\nu$ ,  $\nu_{\max}$ ,  $\Delta\Pi_1$  and  $T_{\text{eff}}$  using a chosen model from the non-axion cooled RGB. The green point on the bottom subplot is the closest model in the axion cooled grid to the chosen non-axion cooled model in terms of mass and radius. Contours of loci of values of  $\chi^2$  corresponding to different  $\sigma_{\bar{x}}$  have been plotted.

<sup>A</sup>The probability is equal to an integral of the pdf of the normal distribution from  $\mu - n\sigma$  to  $\mu + n\sigma$ , where  $\mu$  is the normal distribution's mean

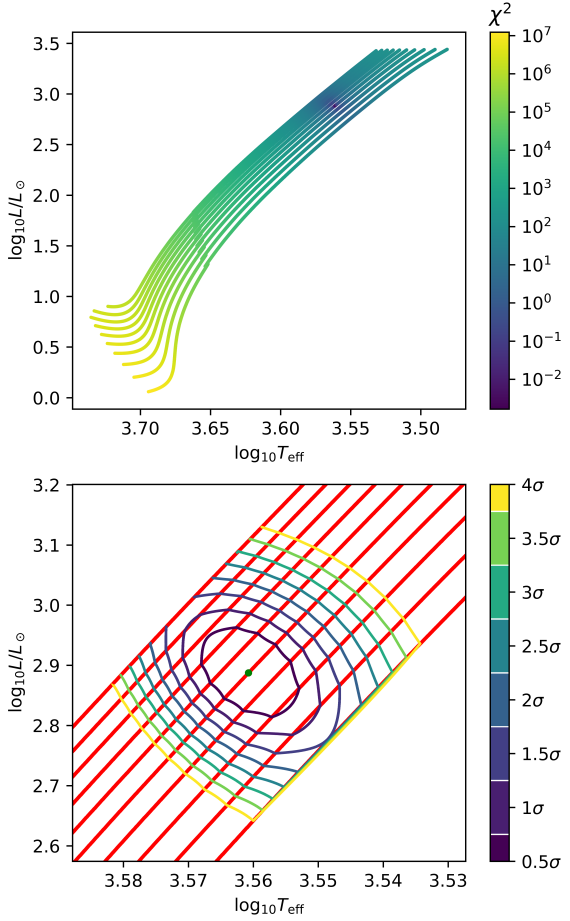


Figure 4.2: Top subplot: HRD for axion-cooled RGB model grid with  $\chi^2$  plotted as colour of points. Bottom subplot: HRD zoomed in on minimum of  $\chi^2$ .

#### 4.2.2 Application of statistical method to model grids

The stages of stellar evolution for which this method was applied were three sub-stages of the red giant branch; low luminosity, RGB bump and high luminosity, and the method was also applied to the RC. These stages of stellar evolution were isolated from the MESA output tracks using the script described in section 3.4. The MS was not considered due to the large uncertainty on determination of  $\nu_{\max}$  in this region 3.4. The non-axion cooled and axion cooled model grids were of solar chemical composition, with axion-photon coupling constant set to 0 and 1 respectively. The highest mass evolutionary track used for both grids was the  $1.7 M_{\odot}$  track as stars of higher mass do not behave as solar-like oscillators (see section 2.1). As a result of this, each model grid is comprised of 10 stellar evolutionary tracks with masses at  $0.1 M_{\odot}$  increments between  $0.8 M_{\odot}$  and  $1.7 M_{\odot}$  inclusive. It should be noted that the mass remains constant throughout each evolutionary track that makes up the grid as RGB mass loss was not in effect.

To sample the low-luminosity RGB, three models were chosen from the non-axion cooled low-luminosity red giant branch with  $\log_{10} 0L$  equalling 1.0, 1.2 and 1.4

when rounded to one decimal place (corresponding to  $L = 10 L_{\odot}$ ,  $15.8 L_{\odot}$  and  $25.1 L_{\odot}$  respectively). Each of the models was selected randomly from the grid with this luminosity constraint in place. For all of these, the value of  $n$  returned by the python script was  $\inf$  (i.e.  $\infty$ ), meaning the closest model in the axion cooled grid to the chosen non-axion cooled model in terms of mass and radius was also the closest model in terms of asteroseismic parameters and effective temperature. This suggests that axion cooling has little effect on stars in the low-luminosity red giant branch as the mass and radius difference between model grids with and without axion cooling in effect for models with the closest effective temperature and asteroseismic parameters.

Similarly, three models were chosen from the non-axion cooled high-luminosity RGB whose  $\log_{10} 0L$  equalled 2, 2.6 and 3.2 when rounded to one decimal place (corresponding to  $L = 100 L_{\odot}$ ,  $398.1 L_{\odot}$  and  $1584.9 L_{\odot}$  respectively). The values of  $n$  calculated for these three models were  $\infty$ ,  $3.7 \times 10^{12}$  and  $2.1 \times 10^8$ . These are unrealistically high numbers of observed stars in the vicinity of the chosen models that would be required to make an assessment about the presence of axion cooling via axion-photon coupling. As such this suggests that the effects of axion cooling in the high luminosity RGB on the mass and radius of a star would be almost immeasurably small.

For the analysis of the RGB bump, three models were chosen from the RGB bump of the MESA output model grid for which axion cooling was not enabled. As the luminosity range of the RGB bump varies significantly depending on the mass of the star, instead of choosing models at certain luminosities, the models were selected from the RGB bump with the constraint that their masses equalled  $0.8 M_{\odot}$ ,  $1.3 M_{\odot}$  and  $1.7 M_{\odot}$ . The model selected from the  $0.8 M_{\odot}$  evolutionary track yielded  $n = 9.97 \approx 10$  ( $\sigma_{\bar{x}} = 0.32$ ), the model selected from the  $1.3 M_{\odot}$  evolutionary track yielded  $n = 4.12 \approx 5$  ( $\sigma_{\bar{x}} = 0.49$ ), and the model selected from the  $1.7 M_{\odot}$  yielded  $n = 8.34 \approx 9$  ( $\sigma_{\bar{x}} = 0.35$ ). From these values it is apparent that the change in mass and/or radius in the RGB bump for a constant set of asteroseismic parameters as a result of axion cooling is significant, as the number of observed stars required to make a judgement about the presence of axion cooling in each case is low at  $n \sim 10$ .

It was determined from preliminary investigation into the data set that the mass difference between non-axion cooled and axion cooled models in the RC when asteroseismic parameters and  $T_{\text{eff}}$  were held constant was typically much larger than in the RGB. For this reason, an iterative process was used whereby 1000 models were chosen at random from the RC of the non-axion cooled model grid and the previously detailed process in calculating a suggested number of observations  $n$  executed for each of them. The value calculated was  $n = 0$  for 756 of the 1000 chosen non-axion cooled models. An  $n < 1$  result is obtained when  $\sigma_{\bar{x}}$  for the axion cooled model with mass and radius closest to the chosen non-axion cooled model is greater than 1. This indicates a very large difference in mass and/or radius

between the non-axion cooled model and corresponding axion cooled model with the most similar  $T_{\text{eff}}$  and asteroseismic parameters. Clearly this is not suggesting that no observations would be required in order to make a judgement, but rather that one observed star would be sufficient.

The application of this statistical analysis identified the RGB bump and particularly the RC as useful stages of stellar evolution for comparison of observational data to MESA output model grids in order to attempt to judge the presence of axion cooling. In order to narrow down further a place to look, the mass difference between non-axion cooled and axion cooled models for constant asteroseismic parameters and effective temperature was further investigated in the RGB bump and RC.

#### 4.2.3 Analysis of mass difference as a result of axion cooling in the RGB bump and RC

As the RGB bump and RC were identified through previous analysis as stages of stellar evolution sensitive to axion cooling on account of non-axion cooled and axion cooled models with similar values of temperature and asteroseismic parameters having significantly different masses. In order to analyse this mass difference in the aforementioned stages of stellar evolution, an iterative process similar to that described in Subsection 4.2.2 (there for RC analysis) was applied.

The process used was a direct extension of the method detailed in subsection 4.2.1. Every model in the non-axion cooled grid (for a particular stage of stellar evolution, e.g RC) was iterated over. During each iteration, the current selected non-axion cooled model's values of  $\Delta\nu$ ,  $\nu_{\text{max}}$ ,  $\Delta\Pi_1$  and  $T_{\text{eff}}$  and the same uncertainties on them listed in subsection 4.2.1 were used to calculate  $\chi^2$  of every model in the axion cooled model grid. The model in the axion cooled grid with the lowest value of  $\chi^2$  was found, and from the mass of this model the mass of the currently selected (at that iteration) non-axion cooled model was subtracted in order to compute a mass difference. This mass difference represents how the mass is different between every model in the non-axion cooled model grid to the model in the axion cooled model grid which is closest in terms of asteroseismic parameters and  $T_{\text{eff}}$ . This mass difference will be represented by the symbol  $\Delta M$ .

In the RGB bump,  $\Delta M$  has only one non-zero value:  $-0.1 M_{\odot}$ . The models possessing these values all correspond to non-axion cooled models with masses greater than or equal to  $1.4 M_{\odot}$ . Most models in the RGB bump have  $\Delta M = 0$ , as is shown by figure 4.3. It is possible that if model grids with higher mass resolution were used, non-zero  $\Delta M$  may be calculable for more of the RGB bump; as the model grids used for this analysis only had mass increasing in increments of  $0.1 M_{\odot}$ , this was the smallest absolute value of  $\Delta M$  that could be found in this analysis.

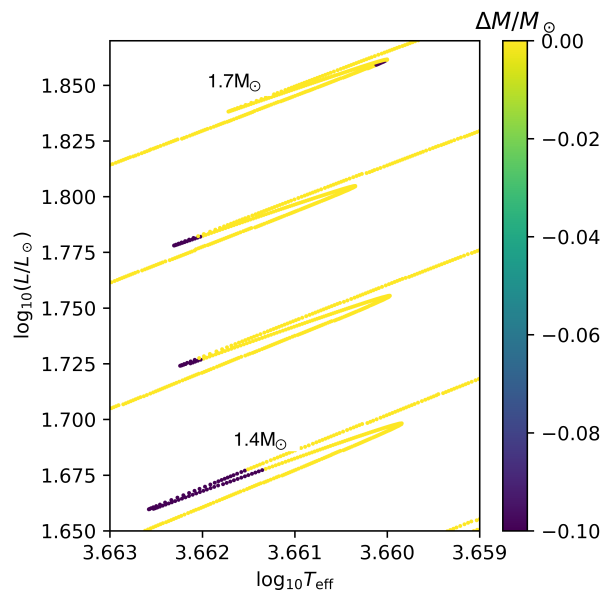


Figure 4.3: HRD of non-axion cooled grid RGB bump showing models with non-zero  $\Delta M$

In the RC  $\Delta M$  takes values between  $-0.9 M_{\odot}$  and  $0.8 M_{\odot}$  inclusive. Figure 4.4 shows how  $\Delta M$  varies within the RC as a function of luminosity and effective temperature (i.e.  $\Delta M$  plotted as colour on an HRD). The dataset was inspected to deduce which masses of non-axion cooled stars corresponded with positive and negative  $\Delta M$ . Doing so found that large negative values of  $\Delta M$  were possessed only by models with high mass, i.e. all non-axion cooled models for which  $\Delta M < -0.3$  had mass between  $1.4 M_{\odot}$  and  $1.7 M_{\odot}$  inclusive. It was also found that large positive values  $\Delta M$  were possessed only by models with low mass, i.e. all non-axion cooled models for which  $\Delta M > 0.5$  had masses between  $0.8 M_{\odot}$  and  $1.1 M_{\odot}$  inclusive. The result for negative  $\Delta M$  is similar to the one obtained for the RGB bump: high mass evolutionary tracks resulting in the greatest negative mass difference due to axion cooling.

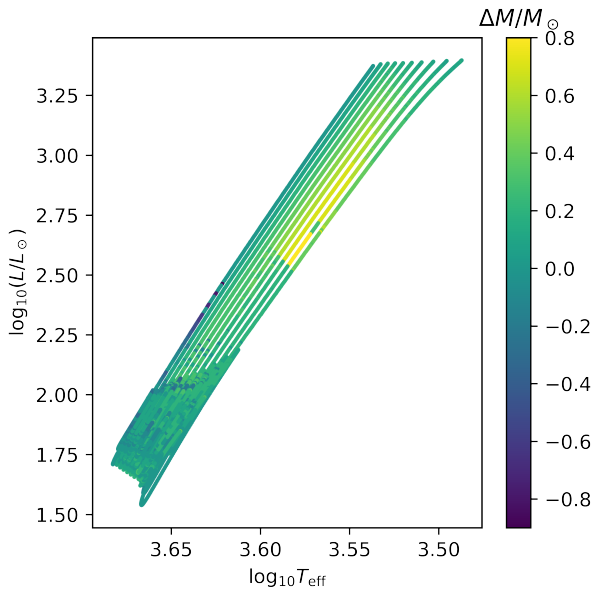


Figure 4.4: HRD of non-axion cooled RC with  $\Delta M$  represented by colour

#### 4.2.4 Conclusions drawn from statistical analysis

As sections 4.2.2 and particularly 4.2.4 have shown, the introduction of axion cooling into MESA results in a significant "mass difference" between non-axion cooled and axion cooled models with the closest  $\Delta\nu$ ,  $\nu_{\max}$ ,  $\Delta\Pi_1$  and  $T_{\text{eff}}$  in the RGB bump and RC but not elsewhere in the RGB. It was calculated that few stellar observations in the RGB bump and RC would be required in order to check if the mass and radius of observed stars best agreed with the MESA model grid produced with an axion-photon coupling constant of 0 or 1;  $n \sim 10$  in the RGB bump and  $n \sim 1$  in the RC. It was found that all non-axion cooled models in the RGB bump with a non-zero mass difference had a negative mass difference and all had masses of  $1.4 M_{\odot}$  or above, and that in the RC non-axion cooled models with higher masses tended to have a negative mass difference while those with lower masses tended to have a positive mass difference.

Commonly used asteroseismic scaling relations for mass determination [11] state that two stars with equal values of  $\Delta\nu$ ,  $\nu_{\max}$  and  $T_{\text{eff}}$  should have the same mass. However, analysis of MESA output model grids has suggested that in the RGB bump and RC models in a model grid for which axion cooling is in effect often have a different mass to corresponding models in a non-axion cooled model grid with the closest values of  $\Delta\nu$ ,  $\nu_{\max}$ ,  $\Delta\Pi_1$  and  $T_{\text{eff}}$ . As no such mass difference was found for models elsewhere in the red giant branch, it is proposed that this mass difference could be tested against observational data for a globular cluster whose stars have a solar-like metallicity (as this was used for the MESA grids) and that contained a sufficient number of stars at various stages of RGB evolution in binary systems. Binary systems would be necessary as

their mass can be determined from the radius and time period of their orbit, allowing a "model-independent" dynamical mass determination [51]. A mass difference parameter could be computed for each RGB star in a binary within the cluster by determining a mass using astrophysical scaling relations and subtracting from it a mass determined dynamically from the orbital properties of the binary. If the values of this observational mass difference showed a correspondence with the computational mass difference between non-axion cooled and axion cooled models found from MESA output data (i.e. they were positive and negative for similar masses and stages of stellar evolution), this could suggest the presence of axion cooling in the cluster's stars.

Finding a globular cluster containing stars with a similar enough chemical composition to the models in the MESA output grids in this investigation may be implausible. As such, an alternative approach would be choosing a globular cluster for which good observed asteroseismological data already exists. Model grids could be produced with a chemical composition more similar to that of this chosen cluster, and the statistical analysis described could be performed on these model grids to allow direct comparison to observed data from the cluster.

### 4.3 Investigating Stellar Central Properties

#### 4.3.1 Chemical Composition <sup>K</sup>

Using data generated from MESA for a synthetic set of stars with and without the effects of axion cooling considered, the extent to which the core composition varied between models was investigated. The motivation behind this route of query stems from the idea that the energy losses from the axion cooling processes have an effect on the rate of energy generation in the stellar cores thus altering the rate of evolution, hence, its chemical composition at any evolutionary stage. In order to more easily identify any variations, the data was split using the data trimming script (see Section 3.4). For each section of data for stellar models in the mass range  $0.8 M_{\odot} - 2.0 M_{\odot}$  in increments of  $0.1 M_{\odot}$  the central H, He, C and O fractions were plotted as a function of central temperature. Temperature was chosen as the independent variable as opposed to age since age was deemed as no longer sufficient to describe the same point of evolution for stars between the models with and without axion cooling.

For the case of H, no change was found between the models across the entire mass range covering all stellar evolutionary stages. This showed the effect of axion cooling was neither dependent on mass nor affected stars during the MS. This was deduced as the conversion of H to He in the stellar core is a process that exists only in the lifetime of a star during the MS. This can be seen in Figure 4.5 for a mass of  $1.4 M_{\odot}$  in the middle of the mass range explored.

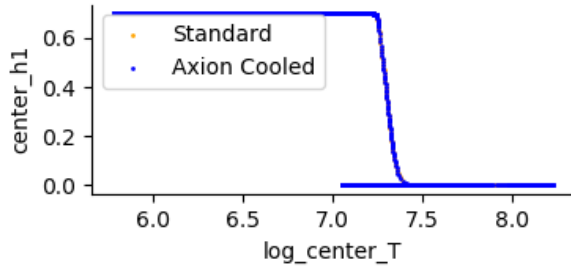


Figure 4.5: Central H fraction plotted as a function of the central temperature for stellar models of  $1.4 M_{\odot}$  with and without the effect of axion cooling considered across the entire evolution of the star.

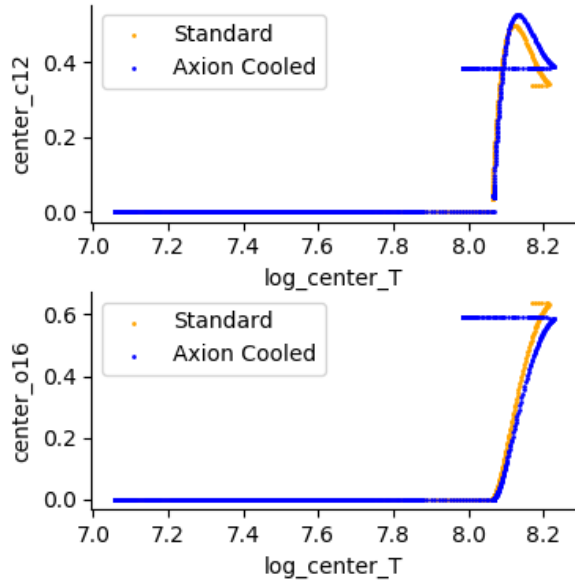


Figure 4.7: Central O and C fraction plotted as a function of the central temperature for stellar models of  $1.4 M_{\odot}$  with and without the effects of axion cooling considered for the RC region.

For the case of He, similar to H, no change was observed until the end of the RC region. At this point the axion cooled model shows slightly higher temperatures compared with the standard models. This difference is observed in Figure 4.6 where the change in temperature is justified as the standard and axion cooled models show the same trend but shifted in the horizontal direction.

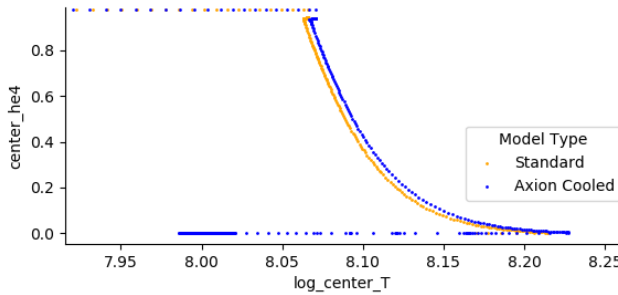


Figure 4.6: Central He fraction plotted as a function of the central temperature for stellar models of  $1.4 M_{\odot}$  with and without the effects of axion cooling considered for the RC region only.

On the other hand, a consistent increase in C and decrease in O was observed towards the end of the RC region in every mass track studied. This would only be a phenomenon observed in the RC as thermonuclear processes producing the two elements only happen after the star experiences a He flash post-RGB. An example of this observation can be seen in Figure 4.7.

The largest level of variation was observed in the  $2.0 M_{\odot}$  models. However these were disregarded from further investigation as it was identified that masses above a  $1.8 M_{\odot}$  limit were no longer abiding by the behavioural conditions of a solar-like oscillator. By its very nature, the core composition of a star is fundamentally not an observable as the ability to probe the chemical content of a stellar core is blocked by the opaque outer layers of a star. For this reason, quantifying a measured difference relative to an error in observing the chemical composition is not possible so these variables were omitted from further investigation going forward with the project.

### 4.3.2 Pressure $K$

Using the same set of MESA data and applying similar analysis techniques as those adopted in section 4.3.1, the central pressure was plotted as a function of the central temperature. The motivation for this line of inquiry was based on the principle that the energy losses from axion cooling which speed up the rate of evolution would likely see the contraction of the core occur at a faster rate, which in turn would increase the central pressure of a star. Similar to what was found with the chemical composition, any deviations between the axion cooled and standard models were observed in areas corresponding to the RC region. Figure 4.8 shows the axion cooled model at a consistently higher pressure compared to the standard model by 0.04.

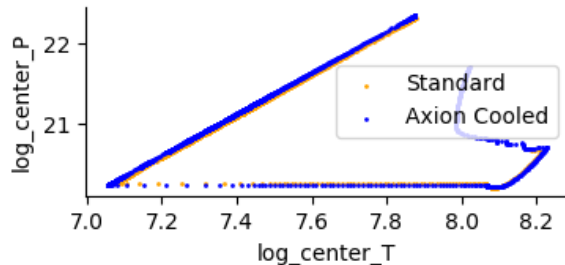


Figure 4.8: Central pressure plotted as a function of central temperature for stellar models of  $1.4 M_{\odot}$  with and without the effects of axion cooling considered for the RC region.

The central pressure is another example of a stellar property that is not a physical observable, meaning it was discounted from any further investigations and comparison with observational data.

#### 4.3.3 Central temperature <sup>F</sup>

Axion cooling is an internal process, therefore any changes in the temperature of the star would be most prominent in the core. By producing plots displaying the variation of the central temperature in each of the four stages produced by the trimming module described in section 3.4, three stars at the start, middle and end of the mass grid were investigated.

MS and SGB stars did not show any large variations in the value of central temperature during these phases of evolution. On the other hand, the RGB and RC stars show much more significant changes in the central temperature.

However, this change is likely due to the faster evolution of the axion cooled models, as the central temperature remains approximately constant across each evolutionary stage of the star. Higher mass stars displayed a greater difference in the central temperature than in those of lower mass, though this is most likely due to these stars not being solar-like oscillators, not the effects of axion cooling within the star.

#### 4.3.4 Radius <sup>L</sup>

To investigate the changes caused by axion cooling in the evolution of a star, evolutionary tracks for stars in the mass range of  $0.8$  to  $2.0 M_{\odot}$  were created, with and without axion cooling. The tracks were cut up into the 5 main stages of stellar evolution - MS, SG, RGB, post RGB, and the RC.

The radius was plotted against the effective temperature on a log-log plot. Detailed analysis was done for three masses in the full range, which are the  $0.8$ ,  $1.4$  and  $2.0 M_{\odot}$  stars. This allowed us to identify general trends in specified regions of the evolutionary track and determine how those trends change with change in stellar mass.

Figure 4.9 shows how a  $1.4 M_{\odot}$  star evolves through its various stages of evolution. There is no significant

difference for most of the MS of the star until the hook at the end of the MS, but this was not explored further due to the low density of models in the transition between MS and the SG phase and due to the possible inaccuracy of the trimming parameters that were used to split the MS from the SG track. Similarly for the SG branch no significant difference is observed between the axion cooled and non-axion cooled tracks. The  $0.8$  and  $2.0 M_{\odot}$  tracks have different shapes for the MS and SG phase, but dont show any significant difference between the axion cooled and non axion cooled tracks.

No significant difference can be observed as the star climbs the RGB, but the tip of the RGB has a lower temperature and a larger radius for the axion cooled model compared to the non-axion cooled one, which is a trend that is observed for all masses. The observed change in temperature is due to energy carried away from the star due to axion emission. This probably leads to faster evolution of the star as the star needs to burn more fuel to compensate for the energy loss, causing the radius of the star to increase due to increased radiated pressure. The RGB subplot in Figure 4.9 shows this difference for the  $1.4 M_{\odot}$  star.

As can be seen in Figure 4.10, the difference on TRGB is about 1% with axion cooling, so detecting axions would be difficult since radius measurement accurate to less than 1% are only available for eclipsing binaries [53] and there isn't enough data available to make reliable predictions. Similarly, difference in the RC is also about 1%. The difference for  $1.9$  and  $2.0 M_{\odot}$  stars is larger but this was probably due to these stars being structurally different, as they don't undergo a helium flash and hence are not considered solar like, therefore these stars were excluded from further investigation.

#### 4.3.5 Surface Gravity <sup>L</sup>

To explore the difference in surface gravity with axion cooling, the tracks were split as before. Due to the increase in radius observed in section 4.3.4 and mass loss due to axion emission, we expected to see a significant difference in surface gravity with axion cooling. To observe this difference we plotted  $\log(g)$  vs  $\log(T_{\text{eff}})$  for the different stages of stellar evolution (Figure 4.11). The changes observed were consistent with mass for solar-like stars so the  $1.4 M_{\odot}$  star is used to infer the changes for solar like stars of all masses.

No difference is observed between the axion and non axion cooled tracks for the MS and the SG stage. The RC only shows about a 1% difference in  $\log(g)$ , which is not significant enough to allow for axion cooling to be identified, as the error on the measurement of  $\log(g)$  is about 2% [54]. This was calculated by taking the average value  $\log(g)$  and averaged errors for the 220 stars and calculating a percentage. The only significant difference is observed on the tip of the RGB where the difference in  $\log(g)$  is 18% for the  $1.4 M_{\odot}$  star, with similar errors observed for the rest of the solar like stars. This provides a possible method for detecting axion cooling as we have accurate  $\log(g)$  data available

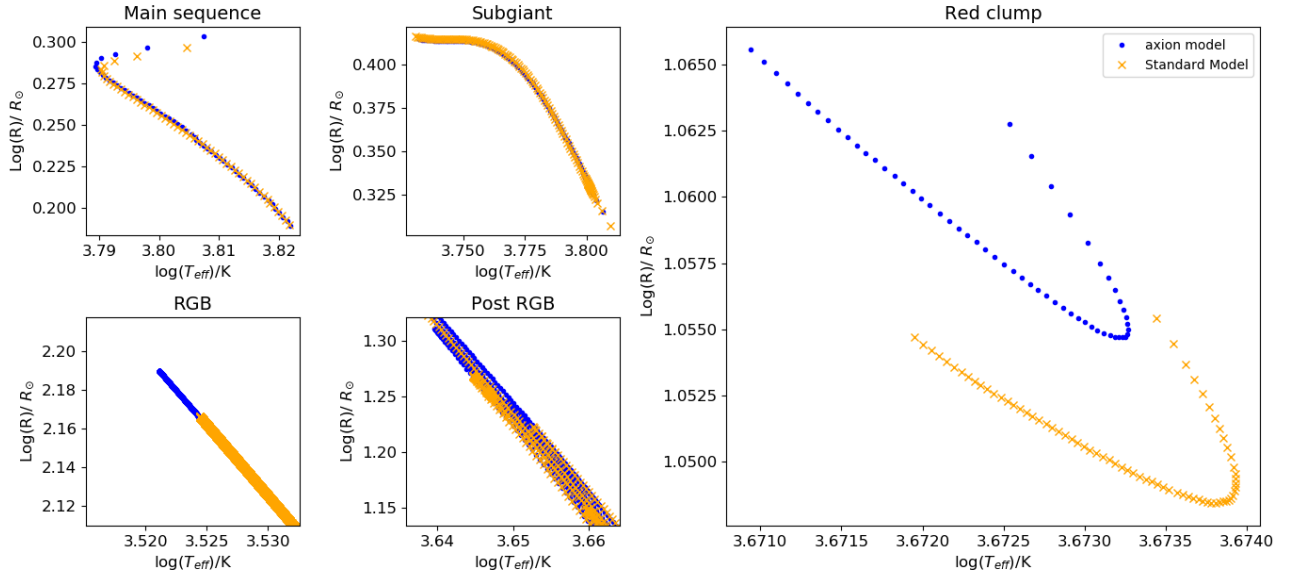


Figure 4.9: Radius against effective temperature for a 1.4 solar mass star, with and without axion cooling, for different stages of stellar evolution (a) MS: shows the full MS evolution of the star (b) SG (c) RGB: zoomed in on the tip of the RGB as that is the only region where significant difference was observed. (d) Post RGB: Zoomed into a specific region of the post RGB branch just before the RC, to clearly show the difference between the two tracks (e) RC

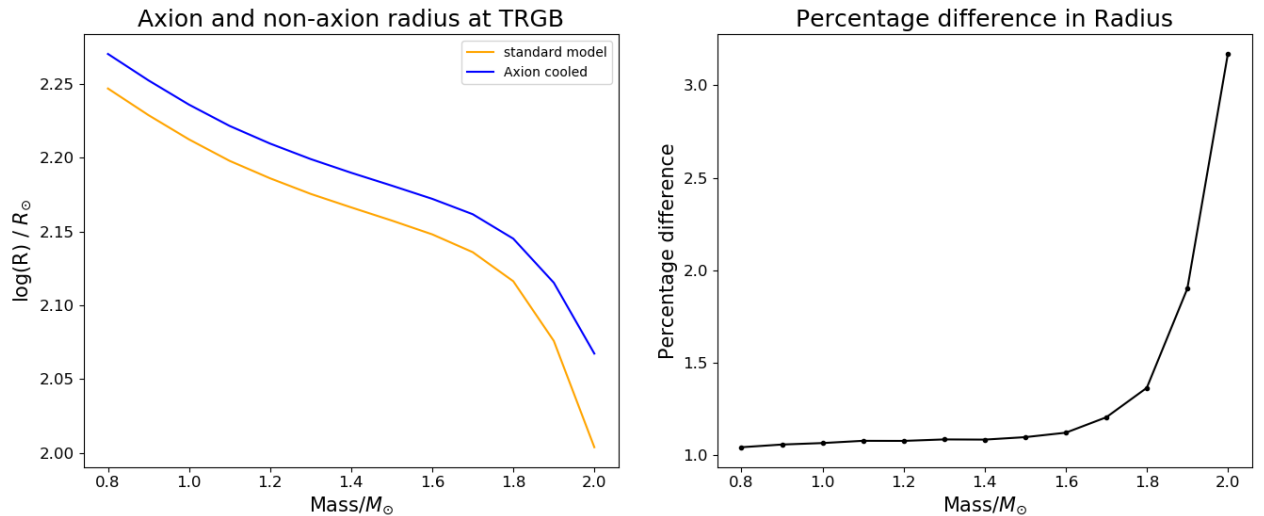


Figure 4.10: Radius against mass at the tip of the RGB (a) shows the radius at the tip of the RGB for stars of different masses with and without axion cooling (b) Percentage difference in radius at the TRGB between the axion and non axion tracks

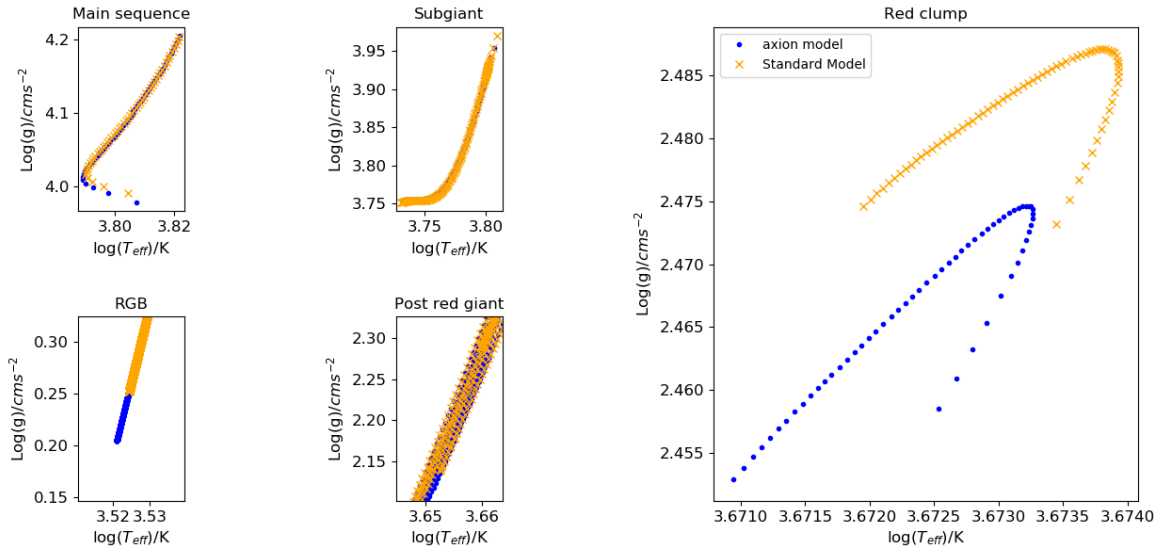


Figure 4.11: Surface gravity against effective temperature for a 1.4 solar mass star, with and without axion cooling, for different stages of stellar evolution (a) MS: shows the full MS evolution of the star (b) SG (c) RGB: zoomed in on the tip of the RGB as that is the only region where significant difference was observed. (d) Post RGB: Zoomed into a specific region of the post RGB branch just before the RC, to clearly show the difference between the two tracks (e) RC

but whether enough of those stars reside on the TRGB to be able to constrain the mass and metallicity of our models needs to investigated further.

#### 4.3.6 Analysis of changes in mass and density <sup>1</sup>

The evolutionary tracks output by MESA were plotted for different masses in the range  $0.8 M_{\odot}$ – $2 M_{\odot}$ . These models were separated into sections that held potential for investigation as discussed previously. The mass and density of each model, with and without axion cooling, were then plotted as a function of  $\log(T_{\text{eff}})$ . The areas of the models that showed the greatest differences between the standard cooled and the axion cooled models were the RGB and the RC, and so these areas were considered for further investigation.

The mass - temperature plots showed no difference throughout the evolution, as MESA does not model any mass loss so both the models with and without axion cooling for each modelled were identical.

The mass - density plots showed a shift in the axion cooled tracks for all masses modelled compared with the non-axion cooled models, noticeably in the RC but also in the RGB. however the difference was very small, at most  $0.2 g/cm^3$ . This difference is in the RC (Figure 4.12), with the RGB showing an even smaller change. Neither of these areas are therefore useful for determining the effects of axion cooling on the density of a star, especially when compared to other observables that can be modelled which show greater differences with axion cooling introduced to their models. From these conclusions, density was no longer considered for comparing observational data.

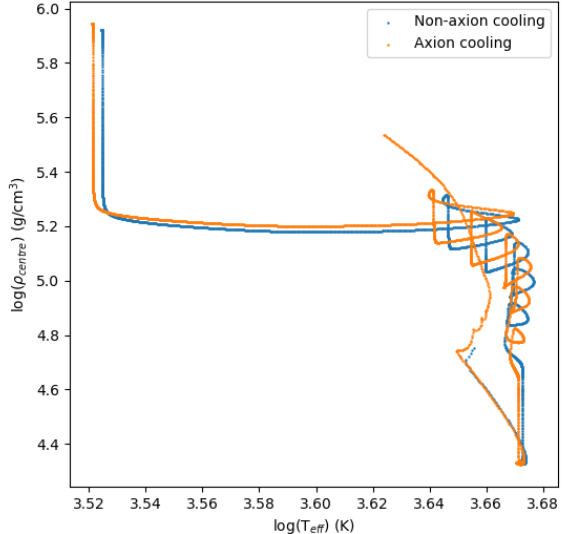


Figure 4.12: Pressure of a  $1.4 M_{\odot}$  as a function of temperature on the RC for non-axion and axion cooled models.

## 4.4 Population & Asteroseismic Parameters

### 4.4.1 Analysis of changes in the R parameter <sup>C</sup>

A good way to detect what must, in actuality, be small changes in stellar evolution caused by axion cooling,

would be to consider a prolonged period of stellar evolution rather than its characteristics at a single point in time. Such a parameter is the well established R-parameter [55]. The R-parameter is the ratio of the RGB lifetime to the horizontal branch lifetime. Practically in observational terms this corresponds to the ratio of the number of stars observed on the RGB to the number observed on the horizontal branch at our snapshot in the evolution of a cluster. The mass of a star obviously also affects its evolution therefore the R-parameter of the MESA models was plotted as a function of mass with and without axion cooling, see Figure 4.13.

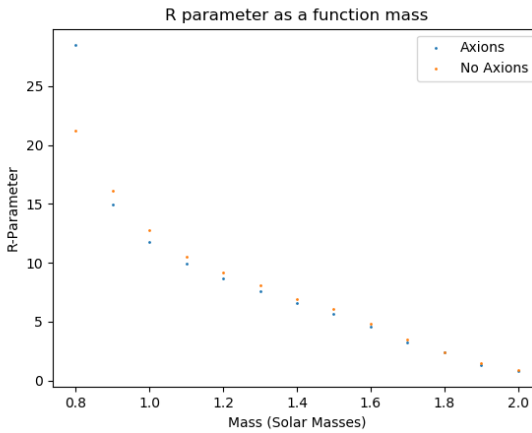


Figure 4.13: The R-parameter of the MESA outputs as a function of mass with and without axion cooling.

It can be seen that the R-parameter is reduced when axion cooling is implemented. This is likely because the axions transport energy out of the stars and so the stars evolve along the RGB at a much quicker rate, hence decreasing the R parameter. However, it is also apparent that changes resulting from axion cooling are less than those between the  $0.1 M_{\odot}$  increments. The gradient,  $dR/dM$ , of plot at  $1.2 M_{\odot}$  is  $-12.98$ . Using the 5% uncertainty on mass from Vrard et al. (2016), the uncertainty on the mass leads to an uncertainty of 0.779 on the R-parameter. The difference between the axion cooled and non-axion cooled models at  $1.2 M_{\odot}$  is only 0.549. Therefore around 20,000 R-parameters would need to be measured for a statistically significant difference to be identified. Since observationally, an R-parameter is a function of a collection of similar stars (i.e. a cluster) the number of R-parameters that can be identified is limited. That being said, a property of clusters is that the masses of all the stars it contains are roughly the same. Therefore, the mass of stars in a cluster could be measured to a high accuracy using a stellar binary which could then be applied to all the stars in the cluster. This would result in a much smaller error due to mass. That would leave the accuracy with which the R-parameter could be measured as the limiting factor. From the study by Ayala et al. (2014) the uncertainty on the measured R-parameter is roughly 2%, which corresponds

to an error on R of 0.26 in this case. This gives a better ratio however still some 2500 R-parameters would be required. There are only about 150 known globular clusters around the Milky Way so going forward, the accuracy with which the R-parameter can be determined needs to be reduced to around 0.05, reducing the error to around 100 times smaller than the expected difference.

#### 4.4.2 Analysis of the changes in $\Delta\Pi$

Evolutionary tracks of solar-like oscillators, with and without axion cooling ( $g_{10} = 0.8$ ), were split into four sections based upon the trimming script (see Section 3.4 to allow easier investigation of any changes caused by axion cooling at different stellar evolutionary stages. After an initial investigation, the RC (in the post RGB phase of evolution) was found to be particularly interesting and so this was added as an additional, more specific phase to look at. The period spacing was plotted as a function of  $\log(T_{eff})$ , as opposed to stellar age in an attempt to compensate for the increased rate of evolution the star experiences with axion cooling, see Figure 4.14.

These plots were compiled for 0.8, 1.4 and  $2M_{\odot}$  tracks to gauge whether the effects of axion cooling vary for different stellar masses. The general trends were the same across all the stellar masses so only the  $0.8 M_{\odot}$  stellar evolution track will be analysed. It is worth noting that a greater change in the period spacing was observed, with the implementation of axion cooling, on the evolutionary tracks of the higher mass stars ( $1.8, 1.9 \& 2.0 M_{\odot}$ ). However, stars of this mass cannot be considered “solar-like oscillators” as their post MS evolution differs from that of a solar mass star. Moreover, these changes in the evolution of the star means that small changes in the mass of the star (equivalent to typical uncertainties on the mass of observed stars) change the expected values of the period spacing more than the implementation of axion cooling does. Therefore, only stars with the masses that more closely match the Sun’s ( $0.8 M_{\odot} - 1.6 M_{\odot}$ ) are considered.

There is no difference in the period spacing observed in the MESA modes on the MS and only a very small difference on the RGB, although the RGB is noticeably longer with axion cooling but this is covered in Section 4.5.2. There is a peak in the period spacing on the SGB which coincides with the decrease in luminosity of higher mass stars ( $1.2 M_{\odot}$  or above) just before the star settles onto the bottom on the RGB. As can be seen in Figure 4.14, the amplitude of this peak is smaller by about 3000 seconds under the influence of axion cooling. However, it is difficult to draw an accurate conclusion about the differences in amplitude because the peaks consist of a single point on the MESA evolutionary tracks. Moreover, these data points are at slightly different temperatures so given the narrow nature of the peaks it is possible that the peaks do in fact have the same amplitude and this apparent difference is simply a result of the low density of

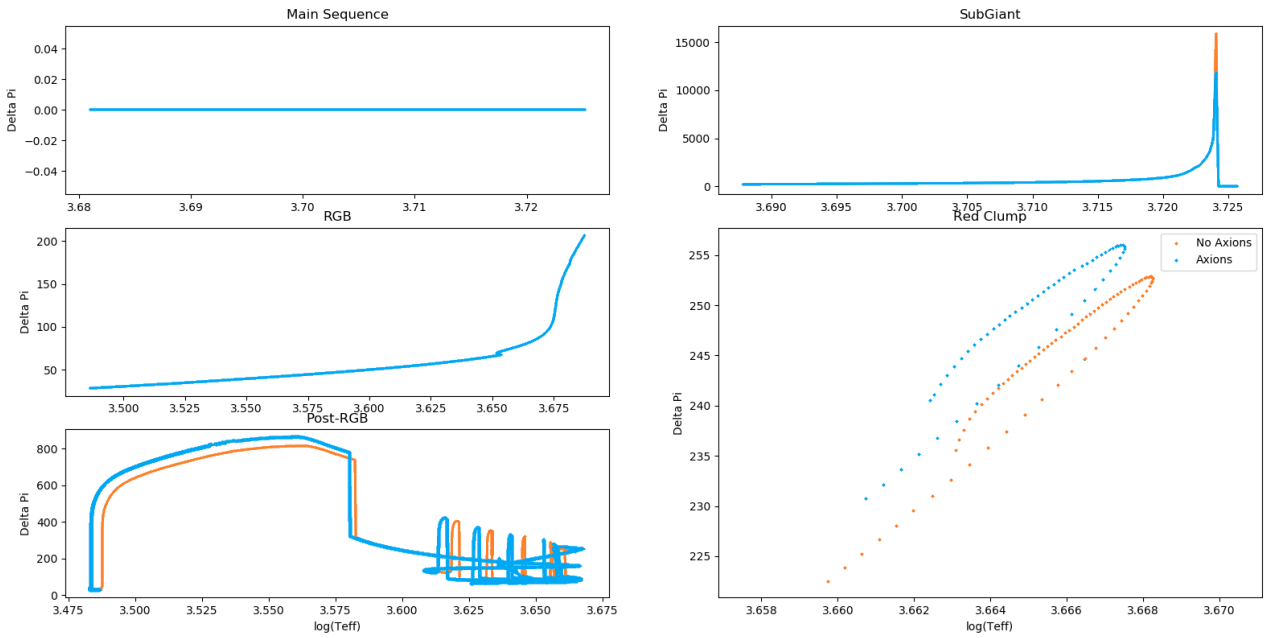


Figure 4.14: Period spacing of a  $0.8 M_{\odot}$  star as a function of temperature on the MS, SGB, RGB, post RGB and RC.

points. The evolutionary tracks were not re-run with a higher density of points as this is very complex and the narrow nature of the peaks means that even if a difference was present, it corresponds to such a small period of time in the evolution of a star, it would be difficult to detect observationally.

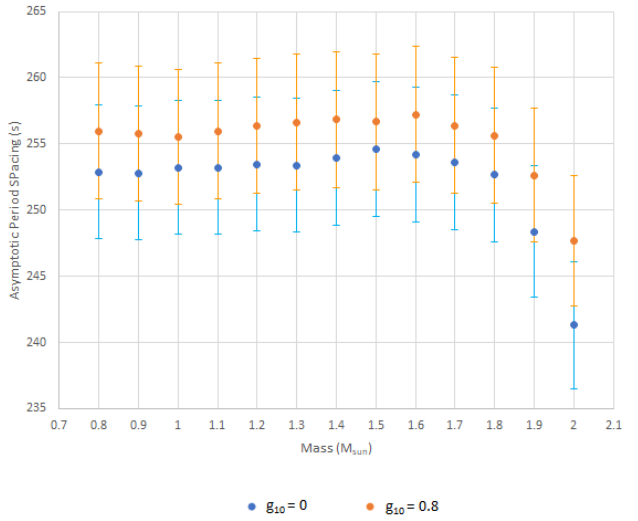


Figure 4.15: The peak period spacing in the RC plotted as a function of stellar mass, with and without axion cooling.

It is immediately evident from Figure 4.14 that axion cooling effects the post-RGB evolution of the star. Whilst most of the post-RGB evolution visible in the plot corresponds to a short period of time in a star's evolution, stars are in the RC for a more reasonable duration. A subplot in Figure 4.14 shows the period spacing as a function of the effective temperature for the duration of the RC. The period spacing is 5 seconds greater for a given temperature with axion cooling however looking at the plot it is apparent that the RC is shifted to a lower temperature with axion cooling which at least partially accounts for this difference in the values. To ensure that this apparent shift was accounted for, the peak period spacing of the RC was plotted as a function of stellar mass with and without axion cooling, see Figure 4.15.

Figure 4.15 shows that there is very little change in the period spacing in the RC between stellar masses of  $0.8 M_{\odot}$ – $1.6 M_{\odot}$ . Beyond this, the stars evolution is different which results in a more drastic change with mass. Therefore, the possibility of identifying axion cooling by the change in the period spacing of the RC is considered for a solar mass star. The gradient,  $dM/d\Pi$ , of the lines in Figure 4.15 is 1.623 therefore, an uncertainty on the mass of 5% [42] on an observed star in a cluster causes an uncertainty on the expected period spacing in the models of 0.03 seconds. The error on the observed period spacing is 5s [42]. The accuracy with which the period spacings can be observed is therefore, the limiting factor in reliably constraining of axion-photon coupling strength. The uncertainty on

an observed star's temperature was found to cause an uncertainty of the order  $10^{-5}s$  on the period spacing of a RC star and is therefore not a significant error.

To be able to confidently identify axion cooling from comparing the period spacing in this way, the uncertainties would need to be reduced by a factor of 100. This could be achieved by observing the period spacing of ten thousand RC stars however there are not enough RC stars for which the period spacing can be measured. Alternatively the observation time could be increased to ten thousands times that of the current Kepler data. In reality, the best course would be the observation of the period spacing of about 1000 RC stars with an observation time 10 times longer than the current Kepler data.

Similar analysis was done on possible detection of RGB period spacing differences. The typical predicted difference with and without axion cooling was only  $0.4s$ , a factor of 20 smaller than the difference observed on the RC which would make it less feasible. However, data for RGB stars is significantly more abundant than for the RC, so this could prove a more promising target if the observational accuracy can be, or isn't, improved.

#### 4.4.3 Analysis of changes in $\nu_{max}^C$

$\nu_{max}$  was a parameter that was not necessarily expected to change with axion cooling however the change in  $\nu_{max}$  with and without axion cooling was analysed for the previously mentioned stages of stellar evolution.  $\nu_{max}$  was plotted as a function of  $\log(T_{eff})$  for each of these five stages of evolution, see Figure 4.16. It should be highlighted that in the original plot, no change could be seen at any stage of the evolution save the RC. Therefore, the plots in Figure 4.16, with the exception of the RC plot which is already a focused look at a short phase in the stellar evolution, do not cover the whole span of the evolutionary stage but are instead an enlarged look at part of that stages evolutionary track to highlight the typical change caused when axion cooling is applied.

It is evident from this figure that even on the scale of individual points on the evolutionary track that there is no difference due to the introduction of axion cooling on the RGB. There is however a clear decrease in  $\nu_{max}$  with the introduction of axion cooling on the MS, the SGB and especially in the RC. The typical uncertainty on observational values of  $\nu_{max}$  is  $0.2Hz$  [56]. It is evident from the flat gradients of the MS and SGB plots in Figure 4.16 that the uncertainties on any observed temperatures is going to cause negligible uncertainty on  $\nu_{max}$ . However,  $\nu_{max}$  is extremely sensitive to mass on the MS and the SGB, with an uncertainty on  $\nu_{max}$  of  $1kHz$  and  $0.5kHz$  respectively from an uncertainty on mass of 5% [42]. Therefore, with the exception of binary systems where there is a very small uncertainty on mass, these are unrealistic targets for axion cooling observation as of the order of a billion stars would need to be observed and analysed. By contrast, the RC is only marginally affected by mass, meaning that the observational uncertainties on  $\nu_{max}$

are the main source of error. Moreover, the difference between axion cooled and not axion cooled in the RC is  $4.5Hz$  therefore only of the order 10 – 100 stars would be necessary to reduce the errors sufficiently to confidently detect axions.

#### 4.4.4 Analysis of the first cycle models - $\Delta\nu^N$

In order to determine if the p-mode large frequency separation  $\Delta\nu$  would be a parameter likely to change due to the introduction of axion cooling, the change in  $\Delta\nu$  between the MESA output models with and without axion cooling included was investigated. For this investigation, the model evolutionary tracks were broken up into four stages of stellar evolution: MS, SGB, RGB and RC. A recent value on the uncertainty on  $\Delta\nu$  from the literature is  $0.04\mu Hz$  (Mosser et al. 2014) [14]. Changes in  $\Delta\nu$  between axion cooled and non-axion cooled MESA output tracks significantly less than this uncertainty will not be considered, as measured differences this size in observed data would not be regarded as significant.

In order to investigate how  $\Delta\nu$  changed in each stage of stellar evolution in terms of an astrophysical parameter that can be precisely measured, it was plotted against  $T_{eff}$  for each of the four stages of stellar evolution chosen. For all of the masses considered (between  $0.8M_\odot$  and  $1.8M_\odot$ ), no significant change in  $\Delta\nu$  was found for any of the stages of stellar evolution other than the MS. The largest change in  $\Delta\nu$  in the MS was found at a mass of  $1.2M_\odot$ . Figure 4.17 shows these plots for  $M = 1.2M_\odot$ .

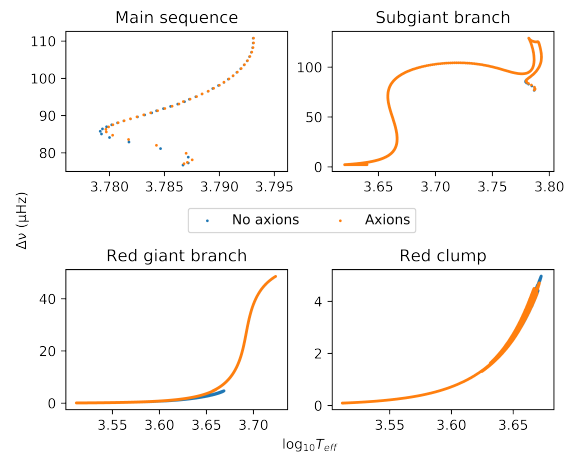


Figure 4.17: Plots of  $\Delta\nu$  against  $\log_{10}(T_{eff})$  for four stages of stellar evolution

#### 4.4.5 Mass and metallicity effects on the $\Delta\Pi_1$ vs $\Delta\nu$ plot<sup>1</sup>

Whilst axion cooling is expected to create a difference in the plots, there are also other factors which may affect these plots by similar, if not greater magnitudes than axion cooling. The two main parameters considered are the mass,  $M$ , and the metallicities,  $Z$ , of any

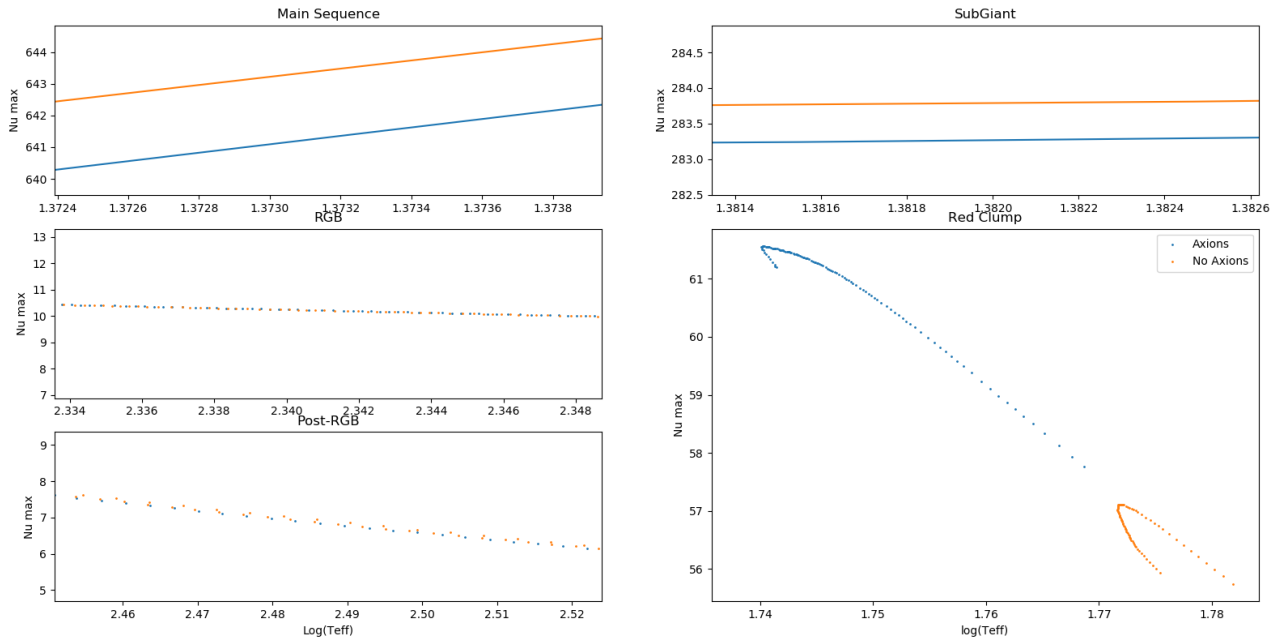


Figure 4.16:  $\nu_{max}$  of a  $0.8 M_\odot$  star as a function of temperature on the MS, SGB, RGB, post RGB and RC.

models produced and subsequently any data that populates these plots.

By first looking at how mass affects plots of period spacing and large frequency spacing, constraints on what data will be fitted to one model can be decided upon. To visualise the effects of varying masses MESA can be used to create models for a range of masses and plot our asteroseismic HRD for them all, as seen in Figure 4.18.

creases, there is a noticeable shift in the value of  $\Delta\nu$ , with a slight but much smaller change in the maximum  $\Delta\Pi$  for some of the tracks. This shift in mass in the x-direction helps to reduce any data available by mass for any specific track used for a plot.

Secondly, the effects of differing metallicities must also be looked at. This is done in a way similar to the masses previously, except this time only one mass of star is used, with varying values of initial metallicity input to show the differing plots. This can be seen in Figure 4.19.

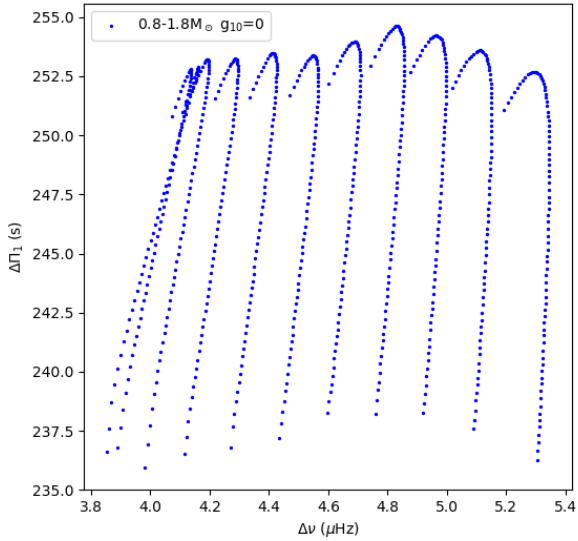


Figure 4.18:  $\Delta\Pi_1 - \Delta\nu$  plots of the RC region using standard cooling models for masses in the range  $0.8 M_\odot - 1.8 M_\odot$ , with increments of  $0.1 M_\odot$ . Mass increases to the right of the plot.

Figure 4.18 shows that as the mass of a star in-

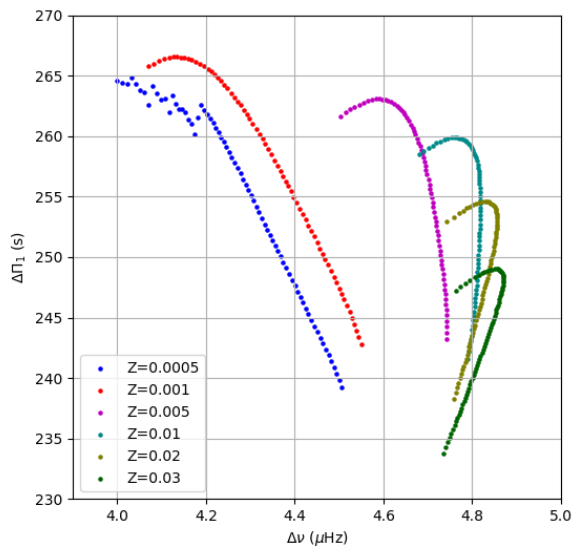


Figure 4.19:  $\Delta\Pi_1 - \Delta\nu$  plots of the RC region using standard cooling models for a star of mass  $1.5 M_\odot$ , with varying values of metallicity,  $Z$ .

Figure 4.19 shows that as the value of Z decreases, the plots move very slightly in the x-direction, however the values of  $\Delta\Pi$  increase significantly. At extremely low values of Z the tracks rotate significantly, and the models are much shifted much more in  $\Delta\nu$ , however the data used later does not use stars with such low metallicities, and so these tracks do not overly concern us. Due to the shifts in the y-direction that different values of Z have on any plots produced, the data must again be reduced, this time covering an appropriate range of metallicity.

Using both of these plots, the effects of mass and metallicity on any plots created are apparent, and also of significant magnitude, with Bossini et al. (2017) agreeing on the conclusion that the period spacing is largely dependent on Z with the support of models [39]. Therefore when choosing any dataset that was not a known cluster, as in section 3.8.4, appropriate ranges of M and Z are necessary to obtain data that can fit to the same model.

## 4.5 Luminosity Changes<sup>C</sup>

From initial investigations, it was clear that the luminosity of the RC and the luminosity of the RGB bump were both affected by the presence of axion cooling. It was observed that the luminosity of the RC decreased in models with axion cooling whilst the luminosity of the bump increased with axion cooling. However, the axion cooling affects the rate of evolution of stars, so the RC and RGB bump appear at different ages and temperatures with and without axion cooling, making a direct comparison unfavourable. Therefore, it is preferential to consider a two dimensional shift in both the RC and RGB bump luminosities by plotting them against each other for varying axion coupling strength. The axion-photon coupling strength can then be constrained by observational data for both the RC and RGB bump. By combining these two observational uncertainties better constraints can be placed on the coupling strength.

### 4.5.1 Luminosity of the Main Sequence and the Sub-Giant Branch<sup>J</sup>

HRD for the MS and SG regions were initially plotted, as shown in Figure 4.20 and Figure 4.21. Although there were some small differences between the luminosities with and without axion-cooling, they were not particularly consistent across the range of masses, and the tracks seemed to follow the same general trend. For example, the  $1.5 M_{\odot}$  track shows a visible difference between the axion and non-axion cooled models on the MS, but such a difference is not seen as clearly for any of the other mass tracks.

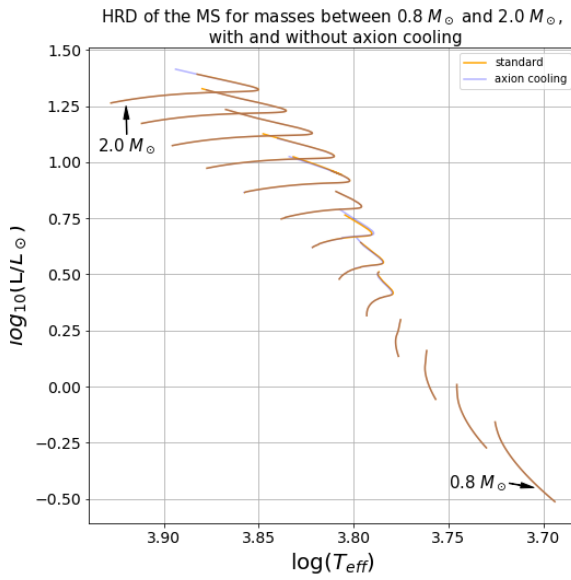


Figure 4.20: HRD of the MS, showing the axion and non-axion cooled models for masses between  $0.8 M_{\odot}$  and  $2.0 M_{\odot}$ .

On the SGB HRD, the models seem to follow the same tracks again, barring small discrepancies at the start of the SG phase for the  $1.6 M_{\odot}$  and  $2.0 M_{\odot}$  tracks. Since these discrepancies are not consistent throughout all the models, this could be due to an error in the trimming function used to separate this region from the MS when applied to these particular mass tracks.

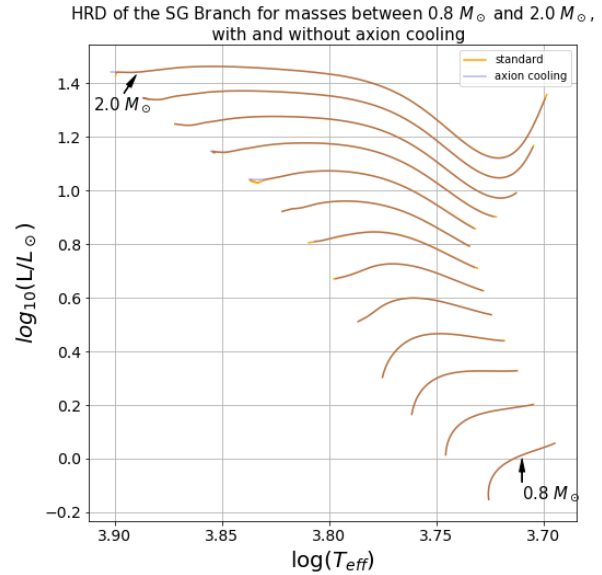


Figure 4.21: HRD of the SGB, showing the axion and non-axion cooled models for masses between  $0.8 M_{\odot}$  and  $2.0 M_{\odot}$ .

A difficulty in investigating the effect axion-cooling may have on the luminosity on the SGB and the MS is actually being able to quantify the differences between

the axion and non-axion cooled models. Since the axion cooled models evolve faster, the change cannot be found through calculating the difference between the luminosity for each model number, since these would not correspond to the same position on the HRD. It is much easier to quantify the difference in luminosity due to a specific, well-defined point, such as the tip of the RGB or the RGB bump. There is also more data on the luminosity of these points in the literature, so it will be easier to compare the model results with observational data.

### 4.5.2 Luminosity of the RGB tip <sup>J</sup>

An HRD of the RGB for all mass tracks (between  $0.8 M_{\odot}$  and  $2.0 M_{\odot}$  with solar composition) with and without axion cooling was plotted in Figure 4.22. The axion cooled models follow the track of the standard models almost exactly, until the tip of the RGB. At this point, a sizeable difference in the luminosities between the axion and non-axion cooled models can be clearly seen. As expected, the tip of the RGB for models with axion cooling activated is at a cooler temperature and higher luminosity than their counterparts of equal mass and metallicity with standard cooling for all masses.

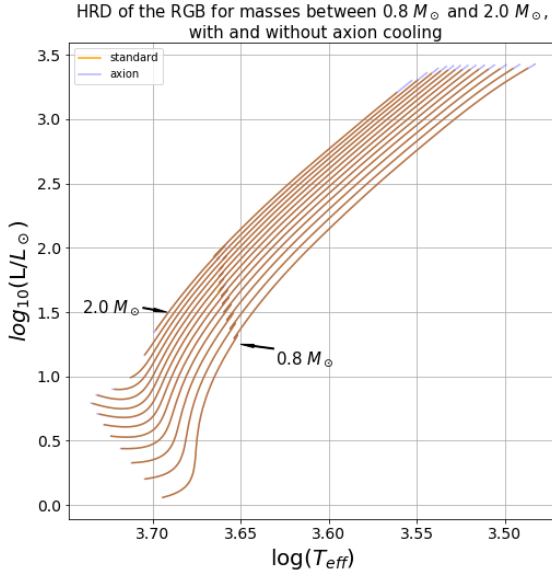


Figure 4.22: HRD of the RGB, showing the axion and non-axion cooled models for masses between  $0.8 M_{\odot}$  and  $2.0 M_{\odot}$ .

The luminosity at the TRGB was found by selecting the maximum value in the luminosity column of the MESA output data. The luminosities for the standard model stars stayed relatively constant, from  $(3.396 \pm 0.001)$  dex to  $(3.35 \pm 0.01)$  dex, for masses up to  $1.8 M_{\odot}$ , and then decrease more dramatically at the higher masses to around  $(3.21 \pm 0.03)$  dex. A similar trend is followed by the axion cooled models, starting at  $(3.43 \pm 0.03)$  dex and decreasing to  $(3.30 \pm 0.02)$  dex at  $2.0 M_{\odot}$ . Errors on the luminosity of the tip for each

mass were calculated using a local gradient of the luminosity with respect to the mass and multiplying by the precision of to which the mass of RGB solar-like oscillators can be determined from asteroseismic parameters, taken to be 4% [57].

The difference between the luminosities of the tip with and without axion cooling was calculated for each mass track and plotted on Figure 4.23. This shows that the differences between the models increase steadily with mass between  $0.8 M_{\odot}$  and  $1.6 M_{\odot}$  from  $(0.030 \pm 0.001)$  dex to  $(0.035 \pm 0.002)$  dex. From this point the difference increased substantially, reaching around three times the luminosity difference for  $0.8 M_{\odot}$ , at  $(0.09 \pm 0.05)$  dex for  $2.0 M_{\odot}$ . The error on the difference was calculated by adding the errors on the two tip luminosities in quadrature.

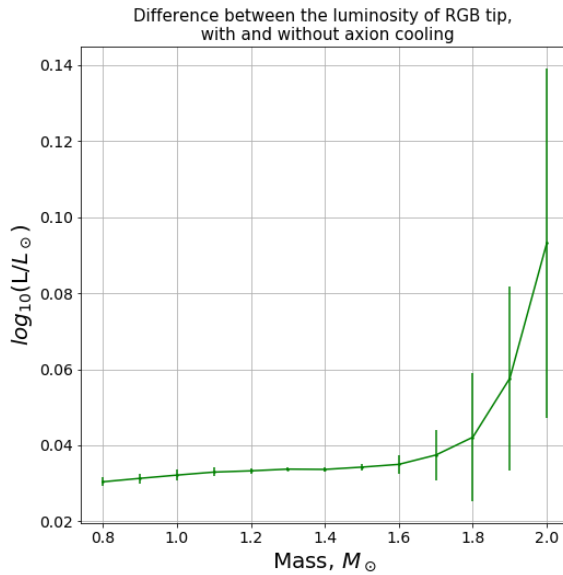


Figure 4.23: The difference in luminosity between the TRGB for stars of masses between  $0.8 M_{\odot}$  and  $2.0 M_{\odot}$  with and without axion cooling.

For the difference between the luminosity of the TRGB for the axion and non-axion cooled models to be statistically significant, the difference needs to be greater than the precision of measuring the luminosity of the tip from observational data. The luminosity of the TRGB can be measured to a precision of around  $\pm 0.1$  dex. This was calculated from converting the bolometric magnitudes of the tips of 22 globular clusters given by Valenti et al. (2004) [58] and the uncertainties on these values to bolometric luminosities of the form  $\log_{10}(L/L_{\odot})$ , and taking an average of the error on each one. The uncertainties on the differences calculated from the models are given in Table B.1 in the Appendix. This shows that all of the differences calculated from the models, apart from that for  $2.0 M_{\odot}$ , are smaller than the average uncertainty in measuring the TRGB from the observational data, even within the errors. However, the values for the luminosity of the TRGB were for globular clusters of varying mass

and metallicities, which means they can not be directly associated with the values from the models.

The more significant difference between the luminosities of the tip of the RGB at higher masses, and the very large errors on these could be due to stars of this mass having a convective, rather than a radiative, core. This means that energy would be lost more efficiently, resulting in the lower temperatures and higher luminosities seen. Consequently, these higher mass stars,  $1.9 M_{\odot}$ – $2.0 M_{\odot}$ , can not be considered “solar-like”, and so were removed from further data plotting.

### 4.5.3 Mixing Zones and the RGB Bump <sup>F</sup>

In order to determine the effects of axion cooling on the RGB bump, first of all the relation between the position of the largest convective mixing zone and the RGB bump was investigated. By displaying the RGB bump for both axion cooled and a standard cooled model, along with the position of the mixing zone varying with age, the impact of axion cooling on the RGB bump can be shown.

The age at which the RGB bump occurs was found to be approximately  $3.57 \times 10^9$  yrs which roughly corresponds to the lowest point of the dip in the mixing zone. Similar plots were also produced for  $0.8 M_{\odot}$  and  $2.0 M_{\odot}$  stars, which also indicated the close relation between mixing zone position and the start of the RGB bump. Due to the accelerated evolution of axion cooled models, the mixing zone dips earlier compared to that of a standard cooled model, however both dip to approximately the same level before the restructuring within the star begins to occur. This is indicative that the mixing zone level is unaffected by axion cooling.

### 4.5.4 The RGB bump as a Function of Mass <sup>F</sup>

Due to the differential change in the RGB bump for the three masses previously investigated, the RGB bump was investigated as a function of mass for the full range produced in the grid. This was appropriate given the previous constraint placed on the limit at which a star will produce an RGB bump described in Section 2.1.4. The RGB bump was plotted on a HRD using a python script for all the masses in the grid, allowing for the impact of mass on the extent of the RGB bump to be checked.

The trends seen in Figure 4.24 are not consistent across the whole mass range. The majority of low mass stars ( $0.8 M_{\odot}$ – $1.3 M_{\odot}$ ) show minor changes in the position of the RGB bump, with the  $0.8 M_{\odot}$  and  $1.2 M_{\odot}$  stars increasing in luminosity, while the remainder of the low mass stars show a decrease in luminosity. The changes due to axion cooling in the higher mass stars are much more significant, with major changes visible for the  $1.4 M_{\odot}$  and  $2.0 M_{\odot}$  stars.

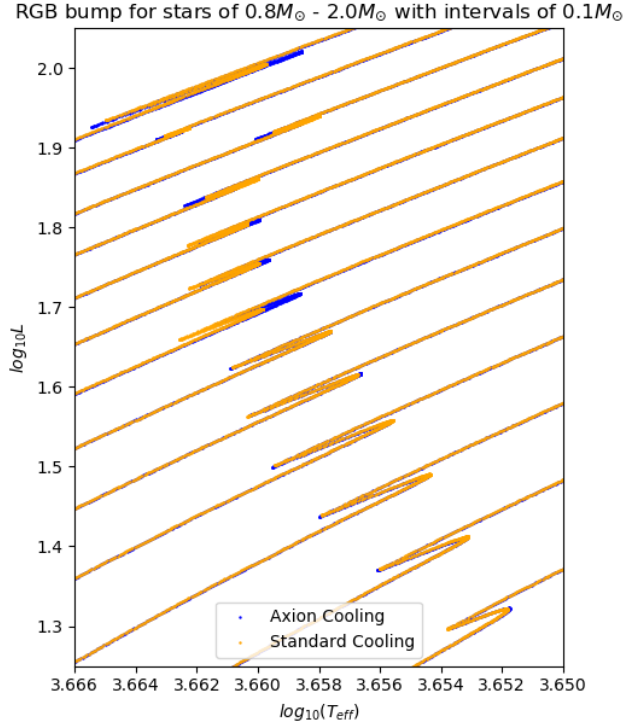


Figure 4.24: HRD focused on the RGB bump for the full grid produced, demonstrating the differential change in the position of the RGB bump from low to high masses. Low mass stars ( $0.8 M_{\odot}$ ) are towards the bottom right of the plot, whereas higher mass stars ( $2.0 M_{\odot}$ ) occupy the upper left hand corner.

Particularly interesting is the way in which the extent of the RGB bump for the  $2.0 M_{\odot}$  mass star has changed entirely, with the axion cooled model having a much greater dip in luminosity than the rest of the masses in the grid. The reason for this however is likely due to the nature at which the stars have evolved, where internally the structure of the star is different to those of lower mass and as such these stars are not representative of solar-like oscillators.

## 4.6 RC Luminosity vs RGB Bump Luminosity

### 4.6.1 Analysis of behaviour of MESA simulations <sup>M</sup>

The selected RC and RGB Bump luminosities were plotted for MESA models of mass  $0.8 M_{\odot}$ – $1.8 M_{\odot}$  in increments of  $0.1 M_{\odot}$ . For each mass, four different axion-photon coupling strengths were plotted, to show the expected effect of different levels of cooling, in order to later compare these predictions with observed data to attempt to constrain a possible value of axion-photon coupling strength,  $g_{10}$  (see Section 4.6). The graph of the luminosities for each model and axion-photon coupling strength is shown in Figure 4.25. No

errors have been plotted for the models, as the size of the errors on the parameters are unclear. This is because no values of uncertainties on the outputs of MESA models could be located, meaning any errors used would need to be estimated. These models will also later be compared to uncertainties on observed data.

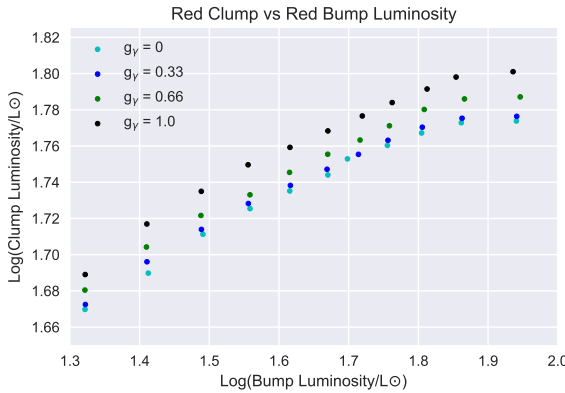


Figure 4.25: Plot showing extracted RC and RGB Bump luminosities from MESA models

An anomalous data point can be seen at a mass of  $1.4 M_{\odot}$ , with  $g_{10} = 0$ . This is the only data point in the data set that breaks the trend of forming an approximate line between the four data points for each mass; it appears as if the RGB Bump luminosity is too low for this model. To attempt to address this, the simulation to create this data point was run again, and the data was manually checked to see if the script created to output the luminosity was indeed selecting the correct data point. After these actions were taken, no improvement could be made. It is unclear what has caused this anomaly.

The impact of the different axion-photon coupling strengths is clear to see in the graph. For each mass (increasing from left to right), as  $g_{10}$  increases, the RC luminosity is impacted by an increasing amount. For a given mass, the impact of axion-photon coupling from  $g_{10} = 0$  to  $g_{10} = 0.33$  is modest, with a small shift in RC luminosity seen. From  $g_{10} = 0.33$  to  $g_{10} = 0.66$ , a slightly greater fractional increase than before in RC luminosity is seen, with the same pattern continuing from  $g_{10} = 0.66$  to  $g_{10} = 1$  where the gap increases again. The increase in RC luminosity seen with increased levels of axion cooling could be attributed to the effect that causes an increase in the luminosity of the TRGB (see Section 4.6). The fact that axion cooling has a more pronounced effect on the RC luminosities at higher values of  $g_{10}$  appears to indicate that the behaviour predicted in Equation 2.42 (see Section 2.4) is being followed. This equation predicts that the energy loss due to axions is proportional to the square of the axion-photon coupling strength.

The impact on the luminosity of the RGB Bump appears to vary between masses. The data points for each mass seem to form an almost vertical line, however the data deviate from this line in various ways

throughout the data set. For some masses, such as the  $0.9 M_{\odot}$  model, there is a slight negative gradient to the data points as axion-photon coupling strength increases. For other models, such as the  $1.6 M_{\odot}$ , this trend seems to reverse, with a positive gradient seen between the four data points for this mass. This behaviour could be explained by the fact that the changes in the RGB Bump luminosity due to axion cooling may be too small to be seen due to the uncertainties on the data. However, it is not clear how meaningful errors could be determined for this data set. If this project were to be repeated, it would be beneficial to attempt to find a way to quantify errors for MESA outputs to enable more meaningful analysis. Approximate errors could have been calculated by estimating the range of luminosities that occur over the lifetime of the RC and the RGB Bump, although it is unclear whether these uncertainties would be significant compared to the unknown statistical uncertainties on the output from MESA.

#### 4.6.2 Model-Data Comparison<sup>F</sup>

Once values of the luminosity of the RC and the RGB bump had been obtained, along with the uncertainties on both values, a comparison was made between the models produced and the obtained estimates of  $L_{\text{Bump}}$  and  $L_{\text{Clump}}$ . Initially the models of varying axion coupling strength were plotted as a scatter (Section 4.6.1), upon which it was possible to overlay the values from Sections 3.5.2 and 3.5.3, along with their uncertainties.

The values of  $L_{\text{Clump}}$  and  $L_{\text{Bump}}$  have been overlaid onto the modelled data, seen in Figure 4.26, along with  $1\sigma$  either side. The size of the uncertainty on  $L_{\text{Clump}}$  is much greater than that of  $L_{\text{Bump}}$ . This stems from the way in which each quantity was determined. The large uncertainty on  $L_{\text{Clump}}$  is due to this value coming from real data, whereas the simulated population which was used to produce  $L_{\text{Bump}}$  will produce smaller errors.

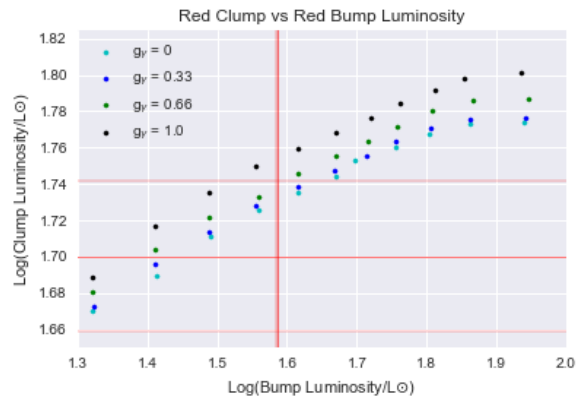


Figure 4.26: Comparing the observed estimates of the luminosity of the RC and RGB bump with modelled data produced by MESA.

The observed data shows the RC luminosity varies fairly consistently within the models and as such the

scale of the estimate provided in Section 3.5.3 is appropriate. However, it is difficult to draw any reasonable conclusions or constraints on the data as there is a clear correlation between the mass of a star and  $L_{\text{Clump}}$ .

This correlation is also evident in  $L_{\text{Bump}}$ , though issues arise when conclusions attempt to be drawn from this data as the uncertainty is so small. The method through which  $L_{\text{Bump}}$  was determined had some flaws, in particular difficulties in separating RGB bump and RC stars within the population. Due to overlap in the luminosities of these stars, the mean value which produced  $L_{\text{Bump}}$  will be skewed from a slight limitation of the range in which stars were deemed to be bump stars. Further work could involve finding a method through which to separate the RC and RGB bump stars effectively. However, from the data provided by the TRILEGAL simulations it was not possible to determine a method which would provide a significant level of confidence from which we could draw conclusions during this research.

One possible extension is to produce a synthetic globular cluster from the TRILEGAL sample used, by combining stars of similar age and metallicities of stars which have been identified as passing through the RGB bump, providing a population of the stars which are necessary for the investigation. This would also provide an indication of globular clusters to search for as the available observational data increases, allowing a comparison of the method used in section 3.5.2 and an indication of its accuracy determined. Using a much larger sample of stars would also improve the accuracy of this method, however the majority of issues that have halted the drawing of conclusions thus far have been due to an excess in precision of modelled data.

## 4.7 Effect of Axions on the TRGB<sup>E,J</sup>

From Section 4.5.2, it was clear that the luminosity of the TRGB could be affected by axion cooling, but the inputs of any comparison models needed to be better constrained in terms of their properties to more accurately compare with observational data. A globular cluster was chosen as the best candidate from data to compare the luminosities since they contain such a large number of stars with similar properties (e.g. age and metallicity), so it is more likely that one will be situated at the tip of the RGB and would be easier to model collectively. The globular cluster M4 (NGC 6121) was chosen as a candidate due to its proximity to Earth, resulting in it being well documented in the literature. The average mass, chosen following correction to the  $\Delta\nu$  scaling, and metallicity of RGB stars in M4 were found to be  $0.84 M_{\odot}$  and  $Z = 0.003$  [59], respectively. The isochrone mass has four nominal errors on it, which were combined using a standard mean, resulting in the models having a mass of  $(0.840 \pm 0.055) M_{\odot}$ . These parameters were input into MESA to produce equivalent evolutionary tracks which

modelled the RGB of M4, with differing values for the axion-photon coupling strength ( $g_{10} = 0, 0.66, 0.8$ ).

Apparent magnitudes for over 70,000 stars in the U, B, V and I bands were found for M4 [60]. Due to the observational data being in magnitude form, artificial and observational data sets were plotted as a Colour-Magnitude Diagram (CMD) instead of a  $\log(L)$  vs  $\log(T_{\text{eff}})$  HRD. The axes chosen were  $m_I$  vs  $m_B - m_I$  as the I-band magnitude best resembled the TRGB luminosity trend observed previously (see Section 4.5.2). The data had to be corrected for reddening caused by interstellar extinction. The reddening correction for M4 was taken to be  $0.37 \pm 0.01$  [61], and this was taken away from the apparent magnitudes. To turn the apparent magnitudes in to absolute magnitudes, the distance modulus,  $\mu$ , was calculated from the known distance to the cluster,  $(1.80 \pm 0.05)$  kpc [61] using the equation,

$$\mu = m - M = 5 \log_{10}(d) - 5, \quad (4.3)$$

where  $m$  is the apparent magnitude,  $M$  is the absolute magnitude, and  $d$  is the distance to the object in parsecs. The distance modulus was taken away from the apparent magnitude values, and the absolute magnitudes were used for plotting a CMD of the cluster.

### 4.7.1 Interpretation<sup>E</sup>

By plotting the stars within the cluster on top of the MESA evolutionary tracks, both with axion cooling and without, we anticipated observing a star within a region on the CMD where axion cooling was modelled. If this were to happen, the axion-photon coupling strength used in the model corresponding to that region would be a lower limit. A comparison between the observational and artificial data is shown in Figure 4.27.

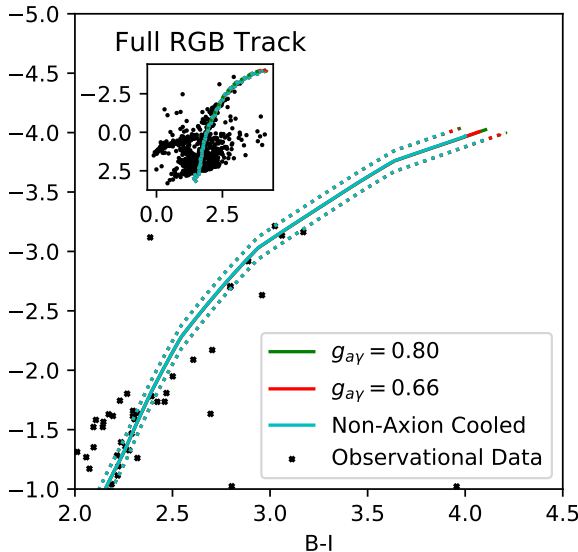


Figure 4.27: *Main:* CMD for the TRGB for the globular cluster M4, comparing observational data with modelled evolutionary tracks for both axion cooled and non-axion cooled models. The bold line is the modelled mass for the RGB of the cluster, whilst the dashed lines are the respective tracks of the modelled mass at its upper and lower error bounds.

*Top-left:* The full M4 cluster data set with the full RGB evolutionary track overlaid.

As shown, the density of stars leading up to the TRGB is thin, and drops off well before the axion cooled extension to the tip. The density is to be expected because as stars ascend the RGB, their evolution accelerates as the rate of hydrogen shell burning increases, resulting in fewer stars at later evolutionary stages along the RGB. However, the drop in the density of points well before the tip prevents us from being able to draw any meaningful conclusions regarding axion cooling from the TRGB. Yet, it is worth noting that the modelled evolutionary track closely follows the RGB for the observational data points, with outliers possibly corresponding to AGB stars later on in their evolution, particularly those points that lie above the RGB track. This is because AGB stars are generally hotter than associated RGB stars due to undergoing helium shell burning rather than hydrogen shell burning. Owing to the correspondence between observational and artificial data, we suggest that this method for potentially identifying axion cooling within stars is still valid, however M4 as a single cluster did not contain enough stars close enough to the TRGB to observe axion cooling.

#### 4.7.2 Improvements

The process of matching an evolutionary track to the observational data for a globular cluster could also be tested for a range of clusters, varying in metallicity and age. This would provide a greater chance of observing

stars within the axion cooled region of a corresponding CMD. The pitfall here is the ability to produce an analogous evolutionary track for the RGB, with the isochrone mass that models the RGB and the chemical composition often being challenging to constrain. The release of Gaia DR2 would aid this process due to containing an unprecedented number of globular clusters for which an isochrone mass and chemical composition can be determined, expanding the number of possible clusters to be used for this method. Additionally, DR2 will reduce the error on determining the tip observationally because it will provide improved parallaxes for numerous stars, which in turn improves the estimate for their distance from Earth and hence their absolute magnitude.

One method for improving results from M4 would be to calculate a theoretical tip for the observational data, similar in fashion to that for M5 [23]. This is because the brightest star along the RGB will not have yet begun helium burning, therefore resulting in a deficit between its magnitude and the magnitude of the tip. This star can be taken as a lower limit on the magnitude of the TRGB in the I-band, providing motivation for examining a theoretical tip beyond this star. One method for calculating this theoretical tip could be that of Vieux et al. (2013) [62], whereby the RGB would have to be simulated through consideration of the evolutionary speed of a star up the RGB. Monte Carlo simulations of the distribution of stars along the RGB would then result in a probability distribution of values for the difference between the tip and the brightest observed star, allowing for this correction to be added to the brightest star to calculate a theoretical tip magnitude. If this were to coincide with the axion cooled region, this would be a significant hint towards the presence of axions and the existence of an axion cooling mechanism within stars.

A secondary method for improving our estimate for the location of the TRGB could be to consider “time-density” spent on a particular section of the RGB. This would require splitting the RGB into “bins” of fixed magnitude (or luminosity) interval and analysing the time spent in each bin. By comparing the time spent in a particular bin to the number of observed stars in the same bin from observational data, it would be possible to extrapolate the bins at which the number density of observed stars was zero, based on their time density. This in turn would allow for an estimate of the TRGB to be made.

We would expect to observe the time and number density decrease exponentially with increasing magnitude. This is because as a star ascends the RGB, the rate of hydrogen shell burning increases and its luminosity increases, shortening the time spent at a particular luminosity. Theoretically, the exponential relationship should be the same if axion cooling is not present, because the number of stars in a given bin and the time-density of that bin are proportional. How-

ever, if axion cooling is present, this would be shown by a translational shift in the power of the exponential due to the increased magnitude of the star from axion cooling. This extra shift would allow a direct calculation of the TRGB magnitude to be performed.

In addition to these proxy methods for determining the theoretical TRGB, it has recently been shown that the tip can in fact be modelled for a globular cluster using its metallicity,  $[M/H]$  [63]. Through use of Equation 4.4, it is possible to obtain a theoretical bolometric magnitude for the TRGB, which in turn can be used to calculate the corresponding luminosity at that magnitude through adapting Equation 3.4 into Equation 4.5,

$$\mathcal{M}_{theory}^{tip} = 0.0161[M/H]^2 - 0.1716[M/H] - 3.87 \quad (4.4)$$

$$L_{\star} = L_0 \times 10^{-0.4\mathcal{M}_{bol}} \quad (4.5)$$

where  $L_0 = 3.0128 \times 10^{28}$  W is the zero point luminosity. Metallicity can be determined from a clusters  $[Fe/H]$  and  $[\alpha/Fe]$  values via Equation 4.6 [64],

$$[M/H] \sim [Fe/H] + \log(0.694f_a + 0.306), \quad (4.6)$$

where  $f_a = 10^{[\alpha/Fe]}$ . Applying these equations to M4 allowed for a theoretical tip luminosity to be calculated for comparison with the MESA models already produced.

For M4,  $[Fe/H] = -(1.07 \pm 0.01)$  dex and  $[\alpha/Fe] = (0.39 \pm 0.05)$  dex [65]. Therefore, using Equation 4.6 for M4,

$$[M/H] = -(0.788 \pm 0.044) \text{ dex}$$

Substituting into Equation 4.4 gives

$$\mathcal{M}_{theory}^{tip} = -3.725 \pm 0.035$$

which when substituted into Equation 4.5 and converted to a  $\log_{10}$  value in solar units, gives

$$\log(L/L_{\odot}) = 3.386 \pm 0.035$$

The errors on all values are calculated through usual propagation of the errors upon  $[Fe/H]$  and  $[\alpha/Fe]$ . The calculated  $\log(L/L_{\odot})$  value lies within  $1\sigma$  of the maximum luminosity of the RGB for the non-axion cooled MESA model (3.341) and is even larger than the maximum luminosities of the  $g_{10} = 0.66$  and  $g_{10} = 0.80$  models too (3.363 and 3.373 respectively). Without constraining the axion-photon coupling strength, this result strongly suggests the presence of axion cooling in stellar interiors, or alternatively an additional effect which is unaccounted for that increases the luminosity of the TRGB.

### 4.7.3 Axion-Electron TRGB<sup>G</sup>

Axion-electron cooled models of M4 were also considered for a number of  $g_{13}$  coupling strengths. The TRGB for each model can be seen in Figure 4.28.

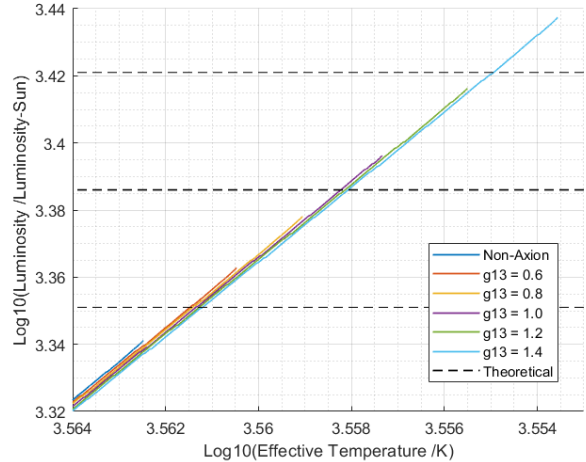


Figure 4.28: HRD showing the TRGB of axion-electron cooled models of M4 with various  $g_{13}$  coupling strengths, with the theoretical tip luminosity of M4 shown with its errors.

Assuming the validity of the theoretical tip luminosity of M4 determined in Section 4.7.2, it is clear that the log of the non-axion cooled model TRGB luminosity ( $3.341 L_{\odot}$ ) is less than  $1\sigma$  of the predicted value. Additionally, the TRGB luminosity of the  $g_{13} = 1.4$  model exceeds the theoretical value by greater than  $1\sigma$ , thus implying  $g_{13} < 1.4$  as an upper limit. Further consideration and application of this method could improve and further verify the constraint on  $g_{13}$ .

### 4.7.4 Alternative considerations from M5<sup>C</sup>

As discussed above, the TRGB was not able to be successfully identified for observational data, as there was a deficiency of points near the tip. However, we know from Section 4.5.2 that the TRGB should vary with axion cooling and that this would be a good place to detect the presence of axion cooling. Therefore we adopt the TRGB luminosity identified from analysis of the globular cluster Messier 5 in the I band [23]:

$$\mathcal{M}_{I,tip} = -4.17 \pm 0.13$$

Using this as an observational limit, the axion-photon coupling strength can be constrained by computing MESA evolutionary tracks with varying axion-photon coupling strength and identifying at which coupling strengths the models agree with the data (within error). The MESA input values were as follows;  $M = 0.82 M_{\odot}$ ,  $Y = 0.245$  and  $Z = 0.00136$ . To best compare with the MESA models the I band magnitude of the TRGB found by Viaux et al. [23] was converted

into a luminosity using the bolometric correction for M5 stars in the I band from Jimenez et al. [66];

$$BC = -0.14 + 0.72(B-I) - 0.19(B-I)^2 = 0.22 \pm 0.02 \quad (4.7)$$

Using the correction above, the I band magnitude was converted to a bolometric magnitude and then a luminosity making the observational luminosity of the TRGB of Messier 5;

$$L_{tip} = (3.39 \pm 0.06) \text{ dex}$$

The characteristic inputs for MESA were identified for Messier 5 as  $M = 0.82 M_{\odot}$ ,  $Y = 0.245$ ,  $Z = 0.00136$ . Evolutionary tracks were then modelled for axion-photon coupling strengths of  $g_{10} = 0, 0.33, 0.4, 0.66, 0.8$  from which the luminosity of the TRGB,  $L_{tip, theory}$  was identified.  $L_{tip, theory}$  was then plotted as a function of axion-photon coupling strength. The tip luminosity found by Vieux et al. (2013) is then overlaid to identify the coupling strength that matches this observation, see Figure 4.29.

The theoretical TRGB luminosity increases with increasing axion-photon coupling strength. This is because a greater coupling strength provides a more effective energy loss mechanism. In turn, this means that the star's degenerate core will be more massive at the onset of helium ignition, and the TRGB will be more luminous.

The error on the theoretical values of  $L_{tip}$  was calculated by considering the errors on the values inputted into MESA to generate models but not errors caused by MESA itself due to limitations on the scientific theory used to generate the code. This is partially because these errors would be smaller than the observational ones considered but largely because an investigation into these theories is a project in itself. These negligible errors include the treatment of mixing length parameters, neutrino emission and mass loss on the RGB of the MESA code. The sources of error that were considered were the RGB-mass, helium abundance and metallicity of M5. The metallicity of M5 was found to have an accuracy of 5.6% by Kraft and Ivans [67]. By plotting an evolutionary track with a metallicity on the upper-bound of the uncertainty, the error on the theory tip was found to be 0.06 dex due to the metallicity determination. Vieux et al. (2013) [23] used the combined results of , Izotov et al. (2007) [68]; Izotov and Thuan (2010) [69] and Aver et al. (2010) [70] to find an uncertainty on the helium abundance of 6% due to both the errors in primordial abundance and the helium enrichment factor. This resulted in an uncertainty of 0.015 dex on the luminosity of the RGB tip in the models. The RGB-mass uncertainty of 6% from Dotter et al. (2010). produced an insignificant uncertainty on the models of just 0.002 dex. The combined uncertainties of these three factors produced an uncertainty of 0.06 dex on the model values and as such correspond to the errors shown in Figure 4.29.

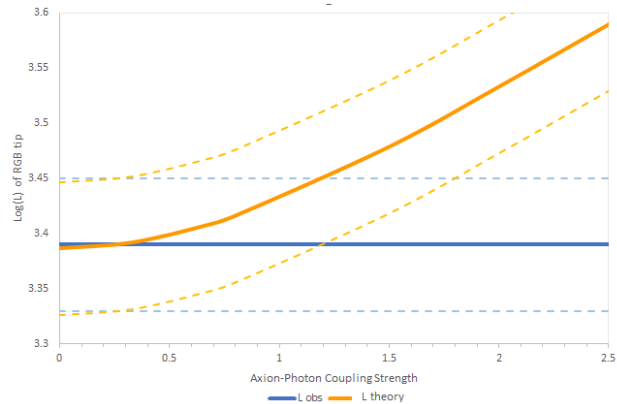


Figure 4.29: The luminosity of the TRGB of M5 for models with varying axion-photon coupling strength compared with the observed tip.

From Figure 4.29 it can be seen that the lines intersect at a small value of axion coupling, in strong agreement with much of the current papers on axion-photon coupling strength. Figure 4.30 is the same plot but focused on a smaller scale about the point of intersection. The value of axion-photon coupling strength at the intersection of the observational tip and the models is shown more clearly in Figure 4.30 as;

$$g_{10} = 0.267$$

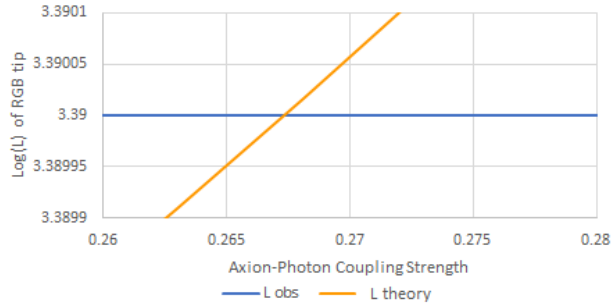


Figure 4.30: The luminosity of the TRGB of M5 for models with varying axion-photon coupling strength compared with the observed tip, scaled about the point of intersection.

However, it is evident from Figure 4.29 that due to errors on both the observational tip and the models the coupling strength cannot be constrained to anything like this kind of accuracy. The models are well within the bounds of error of the observed  $L_{tip}$  even at our reasonable upper bound of 0.8 decided earlier in the project. A conservative upper bound on axion-photon coupling strength can be found by integrating the combined probability distribution and finding the 68% confidence level. This upper bound is  $g_{10} \leq 1.5$ . The lower bound is zero as there is very close agreement between the models and  $L_{tip, obs}$ , well within bounds of error and so a lower constraint cannot be placed which does therefore leave open the question of axion existence, at least in solar like oscillators, or their ability to couple with photons.

It should also be highlighted that axion-electron coupling has not been considered in these models. Vieux et al. (2013) [23] demonstrated that an increase in axion-electron coupling strength also increases the luminosity of the tip of the RGB which would therefore further constrain the upper limit from this method. However, whilst the combined effects of the two coupling effects could be constrained in this way, in addition to the previous individual constraints, it would not be possible to constrain the individual coupling strengths using this method when they are applied in tandem. Therefore, one of the coupling strengths would need to be constrained independently and from that, added to the models to further constrain the other coupling strength.

## 4.8 Frequency & Period Spacing Investigation<sup>B</sup>

Taking a grid of models over the range  $0.8 M_{\odot}$ – $1.8 M_{\odot}$  and a range of coupling strengths, it is possible to look for the predicted trends that axion cooling would introduce.

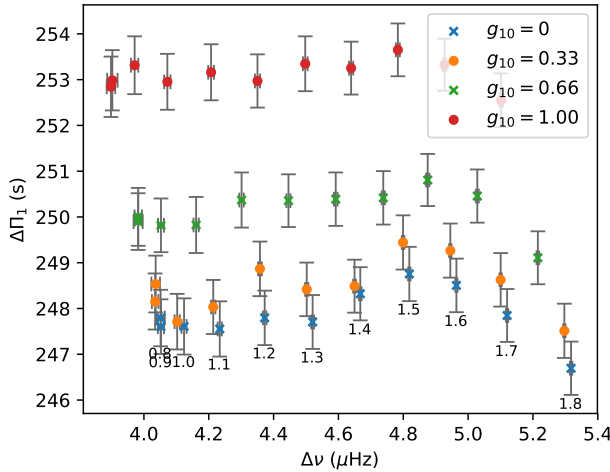


Figure 4.31: The predicted trends of the average asymptotic period and large frequency spacing on the RC upon the introduction of additional cooling due to axions.

An average position was plotted for each evolutionary track in order to provide extra clarity between models of differing coupling constant  $g_{10}$ , especially since the extent of the RC in  $\Delta\Pi_1$  was far larger than any shift introduced by axions. Error bars for Figure 4.31 were provided by calculating a sample standard deviation ( $\sigma$ ) across the RC data in both axes.

Looking at the figure, there is a clear trend that the introduction of axion cooling increases the  $\Delta\Pi_1$ , but also there is a very slight shift towards a smaller frequency spacing  $\Delta\nu$ . The impact of increasing  $g_{10}$  in linear intervals appears to increase  $\Delta\Pi_1$  in a broadly quadratic sense, which likely corresponds to the dependence of the energy loss  $\epsilon_x$  upon the coupling constant

squared, as detailed in Equation 2.42.

Introduction of axion cooling leads to changes in the structural profile of the deep interior, as shown in Equations 2.1–2.4. In turn the Brunt-Väisälä Frequency and sound-speed profiles are affected, as previously described in Section 2.2, and this provides the necessary change observed in the figure.

### 4.8.1 Overshooting Changes

A comparison was also made to see if the introduction of axion cooling would result in any change in the behaviour of the overshooting regions. It is interesting to note from Figure 4.32 that the introduction of axion cooling imparts a small effect not only on the convective core but also the relative boundaries of the overshooting region: the convective core region shrinks slightly whilst the overshooting region broadens marginally.

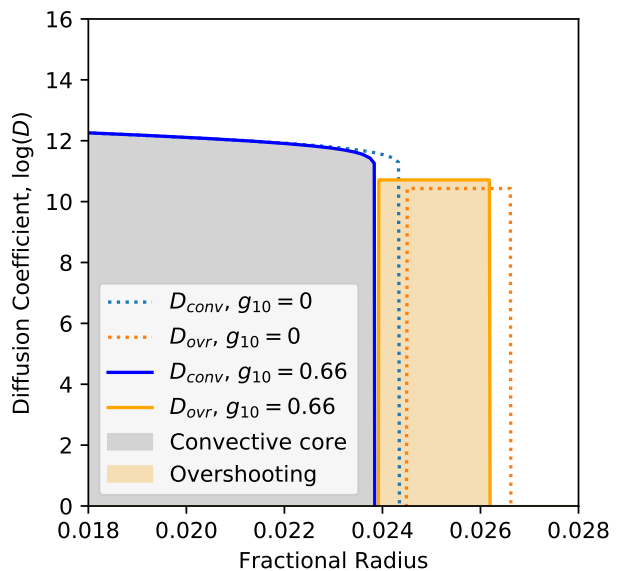


Figure 4.32: Change in convective and overshooting region boundaries around the He-burning core of a RC star upon the introduction of axion cooling.

This can perhaps be explained by referring to Equation 2.35. An increase in the energy loss rate from the non-degenerate HeCB region will result in a contraction and associated heating of the core in order to maintain equilibrium. This mechanism is possibly also the source for explaining why the overshooting region itself broadens. With  $\epsilon_{3\alpha} \propto T^{40}$  (Equation 2.13), the energy transport requirements increase as the temperature gradient out from the core increases. Taking a rough estimate of a mixing length parameter  $\ell_m$  being the radius of the convective core  $r_{cc}$ , the average speed of a parcel of gas in a convective cell is given by [9]

$$v_c \approx \sqrt{\frac{1}{2} \ell_m g \frac{dT}{T}} \quad (4.8)$$

where  $g$  is the gravitational acceleration. The increased temperature gradient hence results in faster convective

motions. Subsequently, elements of the convective cell will possess more kinetic energy and as such are able to travel further into the radiative region surrounding the core, thereby extending the overshooting region.

Further investigation of the impacts of this change are unfortunately beyond the scope of this project, however may be something that can be investigated further in future, in particular with regards to looking at changes in the extent of overshooting, particularly with the uncertainties in modelling core overshooting.[71]

### Core Breathing Pulses

Models that were produced with a LOV mixing scheme had a subtle but noticeable difference in the shape of the data when compared with models using MOV, HOV or no overshooting at all; as seen in Figures 4.33 and 4.35. Data points along the RC no longer formed a smooth curve.

It is not entirely clear why this occurs however it is possible to speculate that this may be the result of the effect of core breathing pulses.[72] This is where the boundary between the convective and radiative zones, as defined by the Schwarzschild Criterion, is not necessarily constant throughout the evolution of the RC. Again, this aspect of the model could potentially be improved through the implementation of a more refined (unspecified) overshooting regime.

### 4.8.2 Calibrating the value of $g_{10}$ using old open clusters <sup>L</sup>

Using the Step Function Overshooting mixing scheme with overshooting parameter  $f = 0.2$  (LOV), an asteroseismic HRD for the RC was plotted for the two clusters with a range of  $g_{10}$  values and populated with the observed data which is shown in Figure 4.33. The RC evolutionary track can be divided into three main sections. The section at minimum  $\Delta\Pi_1$  is the early HeCB phase where structural changes are causing  $\Delta\nu$  to decrease. After this the main HeCB phase starts where overshooting allows for the size of the convectively stable region (core) to grow which leads to an increase in  $\Delta\Pi_1$  while only small change in density explain the minimal change observed in  $\Delta\nu$ . This phase will be referred to as the ladder. The third section is the hook which corresponds to the phase where the star is starting to evolve off the RC.

The value of  $\Delta\Pi_1$  at which the ladder begins, increases exponentially with an increase in the  $g_{10}$ , similarly the value of  $\Delta\nu$  for which the ladder ascends in  $\Delta\Pi_1$  also increases exponentially with  $g_{10}$ , while the end of the ladder, marked by the hook at approximately  $\Delta\Pi_1 = 300s$  is stable and does not seem to change much with increased axion cooling. These observed changes can probably be attributed to faster evolution of the star leading to faster exhaustion of H as energy loss due to axion cooling needs to be compensated for. This will cause the radius to increase as

observed in section 4.3.4, leading to decreased density and hence  $\Delta\nu$ .

Axion-Photon coupling constant of 1.5 appears to fit the data best for this mixing scheme, but the track doesn't reach the two stars (F and B) in NGC 6819, which are early HeCB and hence should provide robust constraints on fitting the models to the data [39]. These early HeCB stars are not present in NGC 6791, possibly due to some of the RC stars being omitted during selection.

Since the cluster NGC 6819 contains the early HeCB stars which provide constraints, we computed additional models using the MOV and HOV schemes as defined in section 3.7.2. The asteroseismic HRD plotted using these schemes are shown in figure 4.34.

For the MOV scheme, a  $g_{10}$  of 1.5 fits the data best, but it doesn't reach the two early HeCB star. The  $g_{10} = 1.0$  track reaches one of those stars but it doesn't fit the rest of the data. However the  $g_{10} = 1.0$  track for the HOV scheme reaches one of the early HeCB stars (B) and most closely fits the stars on the ladder and the hook. This is the best fit that we have obtained across the three mixing schemes. However the ladder for the MOV scheme is less vertical compared to the HOV scheme, which fits the shape of the data better.

From our observations we can visually infer an upper limit on  $g_{10}$  of 1.5, for the three mixing schemes that we have tested. However none of the schemes accurately fit the early HeCB stars that provided constraints for fitting models to the data. This was probably due to our implementation of the HeCB mixing schemes not being completely accurate. From our results, we can't reliably conclude the presence of axion cooling in solar-like oscillators, but future research might provide better independent constraints on the mixing scheme allowing us to determine whether axion cooling exists and if so deduce an accurate value of  $g_{10}$  using this method. Asteroseismic data for more clusters with increased accuracy will also help increase the reliability of this method but future planned missions are not expected to provide reliable cluster asteroseismic data as is discussed in Handberg et al. (2017) [73].

### 4.8.3 Synthetic Cluster Results <sup>I</sup>

Using the data from section 3.8.4, models for clusters 1 and 2 were made using the LOV mixing scheme (3.7.2). Various values of  $g_{10}$  were also plotted for these tracks. The values used for M and Z of the tracks were the mid-range of each value for each cluster. The cluster data was then added to these models, as shown in Figure 4.35.

A similar process was used for cluster 3, however the overshooting parameters used for this cluster were different. Here the HOV and MOV mixing schemes were used in the models (3.7.2), again for varying values of  $g_{10}$ . Cluster 3 data was then added to these plots to create Figure 4.36.

The data for both clusters in Figure 4.35 has quite a large spread with multiple outliers, which makes

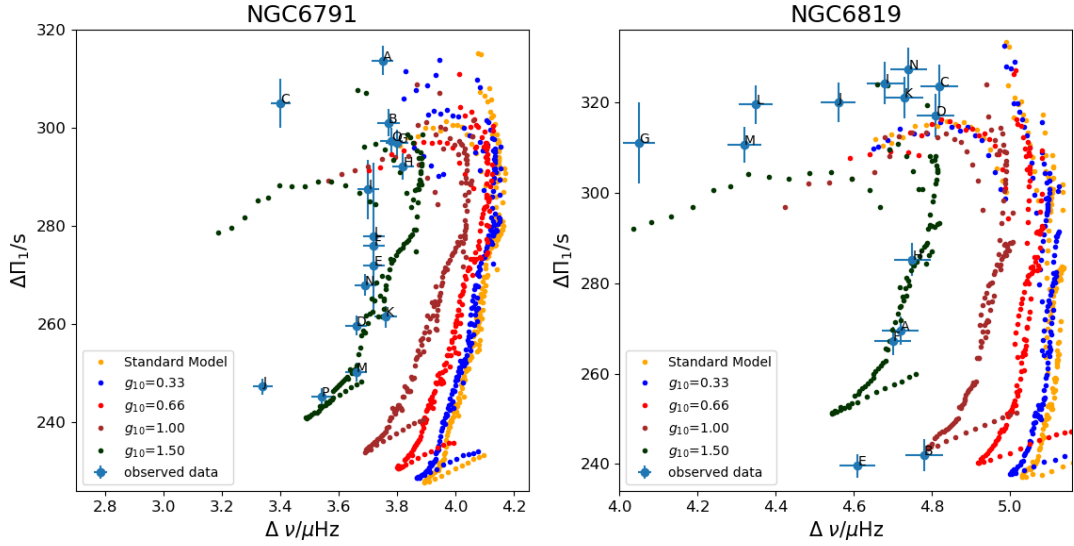


Figure 4.33: The asteroseismic HRD for RC stars in open clusters NGC 6791 and NGC 6819. The observed data was obtained from Bossini et al. (2017) [39] which identified these RC stars for which asymptotic period spacings were available [42]. The evolutionary tracks have been calculated using the core overshooting mixing scheme LOV for different values of axion-photon coupling constant  $g_{10}$ .

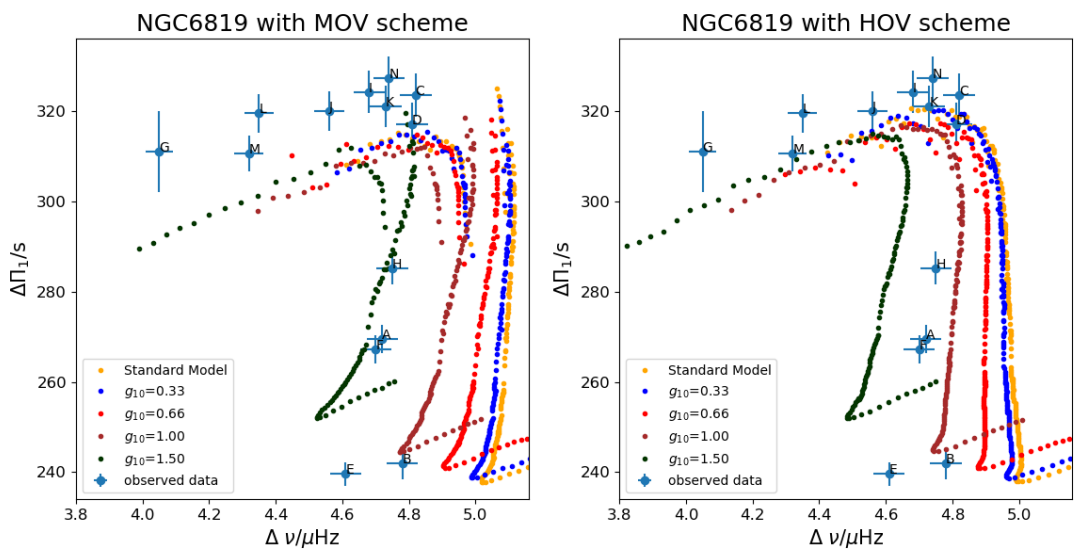


Figure 4.34: The asteroseismic HRD for RC stars in the open cluster NGC 6819 for the MOV and HOV mixing schemes. The observed data was obtained from Bossini et al. (2017) [39]. The evolutionary tracks have been plotted for different values of axion-photon coupling constant  $g_{10}$ .

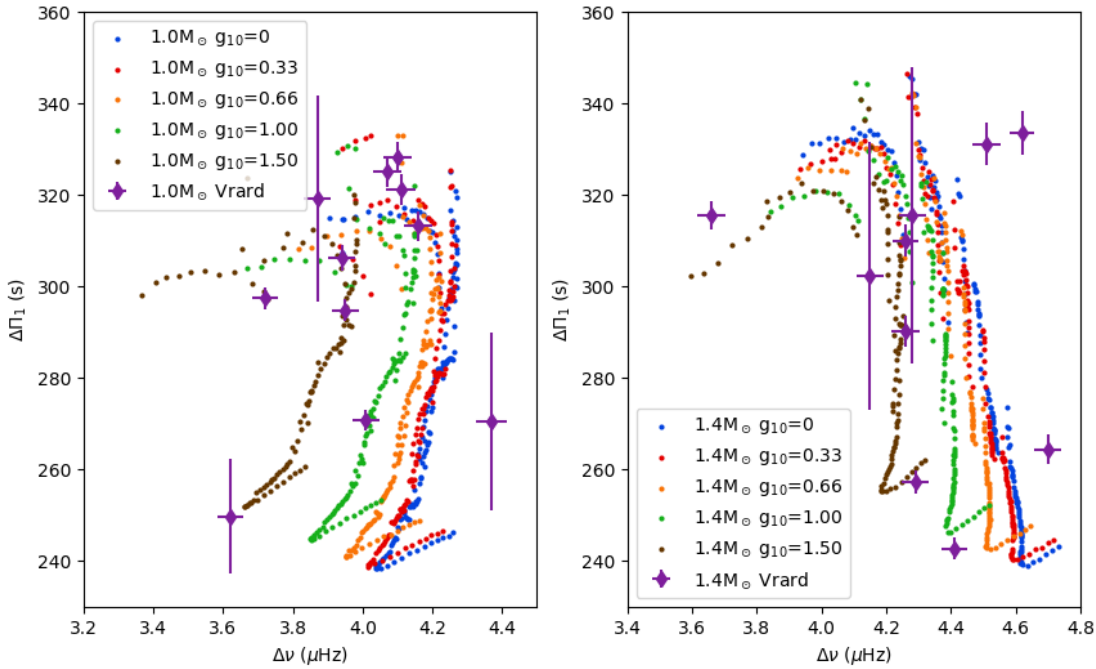


Figure 4.35:  $\Delta\Pi_1 - \Delta\nu$  plots for a) cluster 1 and b) cluster 2 for tracks using the LOV mixing scheme, for various axion cooling strengths.[42]

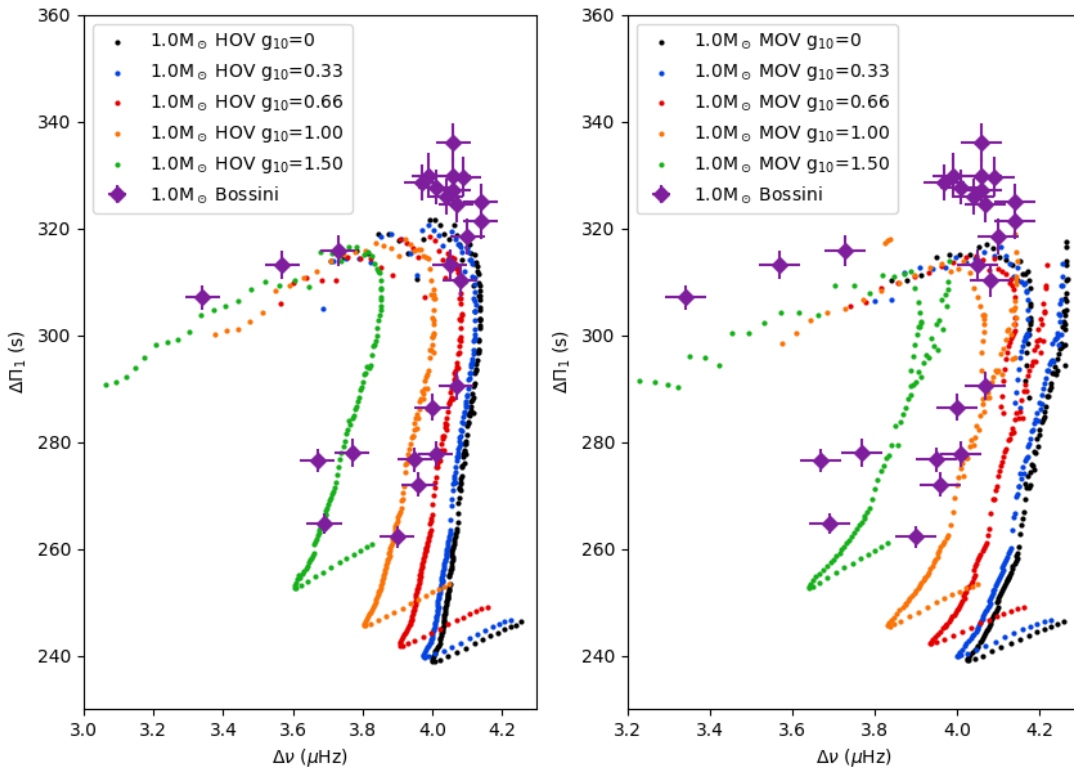


Figure 4.36:  $\Delta\Pi_1 - \Delta\nu$  plots for cluster 3 using the a) HOV mixing scheme and b) MOV mixing scheme, for various axion cooling strengths.[39]

any determination of which axion strength fits the data best quite difficult. This is most likely down to the inaccurate metallicity values given by the Kepler database [43]. From these two clusters values of the cooling strength can be approximated, giving a value of  $g_{10}$  around 1 to 1.5 that looks to fit the data best, however due to the spread of the data this is not a good approximation.

Cluster 3, shown in Figure 4.36, shows more promise for determining a value for the axion cooling strength which best fits our data. The data for both mixing schemes shows slight variation in the best value that fits the data; for the HOV scheme the  $g_{10} = 0.66$  model appears to fit best, whilst for the MOV scheme a value of 1.00 for the axion cooling strength passes through our data better.

In both plots for cluster 3 the models do not appear to be reaching a high enough value of  $\Delta\Pi_1$ , so the models may still be missing some extra parameter that has not been considered, or the mixing scheme used may be incorrect.

## 4.9 Period Spacing of Low Luminosity Red Giants<sup>A</sup>

### 4.9.1 Propagation Diagrams

In an effort to understand the possible effects of axion production on the stellar structure, propagation diagrams were produced for models of seven low-luminosity RGB stars (selected from Hernandez et al. (2016) [47] and axion cooling was implemented with coupling to either photons or electrons (Figure 4.37). There is no observable difference in the Lamb,  $S_l$ , or Brunt-Väisälä,  $N$ , frequencies until the Base of the Convective Zone (BCZ). For the seven stars modelled, a consistent expansion of the low-frequency evanescent region for models with axion-electron coupling<sup>B</sup> implemented was observed, as well as a lesser contraction for models with axions coupled to photons. In the observable frequency range (grey shaded) the peak corresponding to the BCZ does appear shifted, but the absolute size of the convective zone appears unchanged. This effect was probed in more detail using the period spacing pattern (Section 4.9.2).

<sup>B</sup>The scale of the effect as observed here may be larger due to the small error in the axion-electron MESA routine [Appendix A.1].

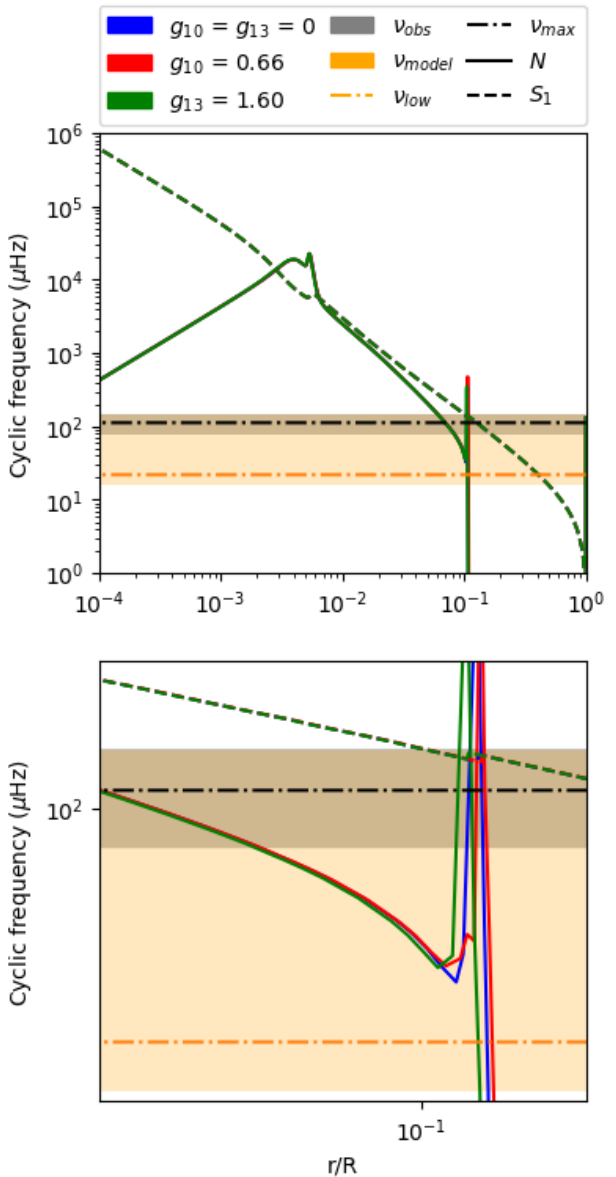


Figure 4.37: *Top:* Propagation diagram for models of KIC 3744043f with no axion production (blue), axion production due to photon coupling with  $g_{a\gamma} = 0.66 \times 10^{-10} \text{ GeV}^{-1}$  (red) and axion production due to electron coupling with  $g_{ae} = 1.60 \times 10^{-13}$  (green). The solid line is the Brunt-Väisälä frequency,  $N$ , and the dashed line is the Lamb frequency,  $S_1$ . The sharp peak at  $r/R \approx 10^{-1}$  marks the location of the BCZ. The dark shaded region indicates the range of oscillation frequencies observed for the star, and the orange region shows the range of frequencies modelled with GYRE.  $\nu_{\text{low}}$  is the central frequency of the lowest frequency trough.

*Bottom:* Close view of the BCZ. Coupling of axions to electrons shifts the position to a lower fractional radius, while coupling to photons has the opposite effect to a lesser degree. These changes were observed consistently for the seven stars modelled

The same stars were then considered on the higher

luminosity RGB (beyond the RGB bump) (Figure 4.38). No consistent effects were observed between the models with different implementations of axion production in this case.

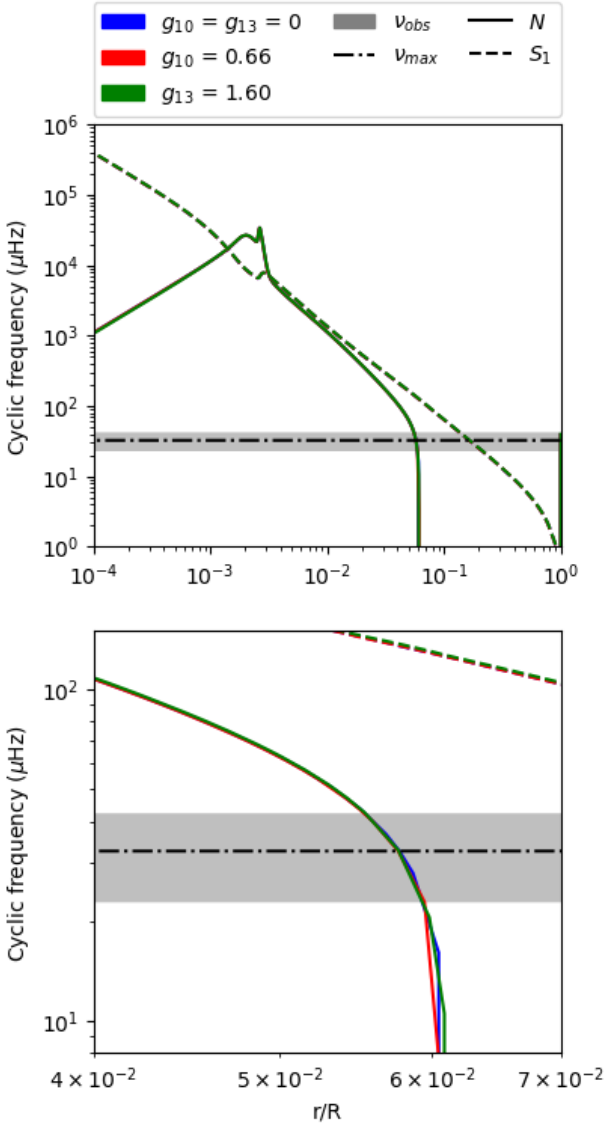


Figure 4.38: *Top:* Propagation diagram for KIC 3744043 modelled higher up the RGB, after passing through the RGB bump.

*Bottom:* Close view of the BCZ; in the seven stars modelled, no consistent splitting of the radial position of this feature was observed.

The case of extreme coupling strengths (an increase of  $g_{a\gamma}$  or  $g_{ae}$  by an order of magnitude or more) was also considered. In models including axion-electron coupling, varying the coupling strength simply resulted in a change in the scale of the effect observed; an increased coupling strength expanded the low-frequency evanescent region further (Figure 4.39). Extreme axion-photon coupling also caused an expansion of this region (Figure 4.40), in contrast to the small contraction observed with a lower coupling strength. The left edge of the evanescent region was also shifted when the highest coupling strength was applied in both the

axion-electron and axion-photon models. The  $N$  was reduced until the base of the BCZ peak, resulting in an expansion of the evanescent region within the observable frequency range.

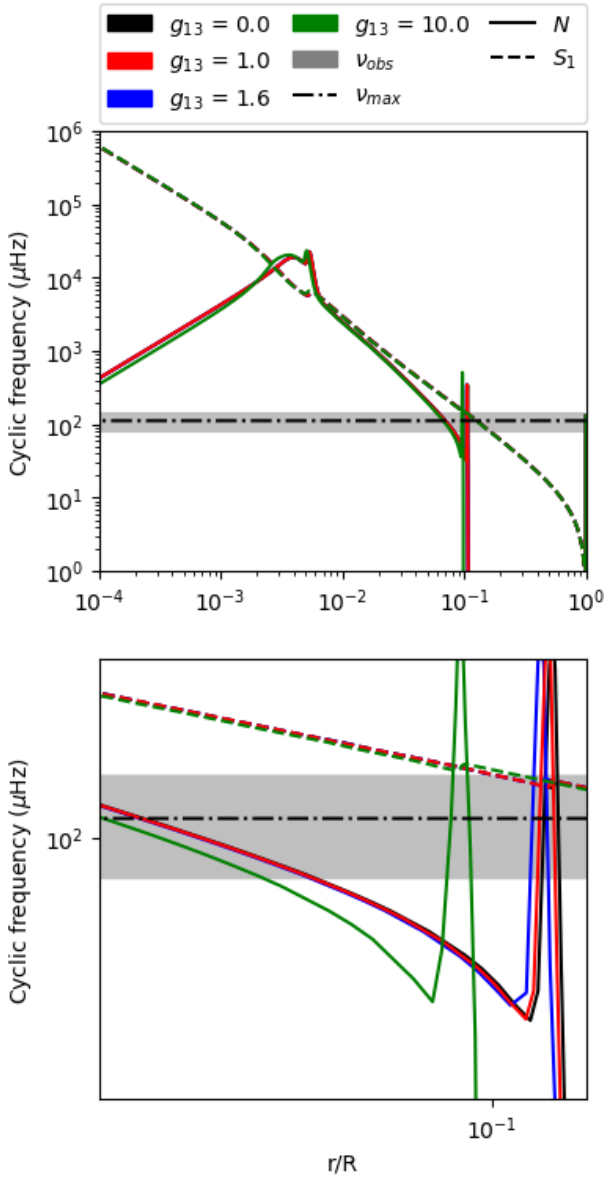


Figure 4.39: *Top:* Propagation diagram for models of KIC 3744043 with a range of axion-electron coupling strengths.

*Bottom:* Close view of the BCZ, showing the greater shift to lower fractional radius at increased coupling strength.

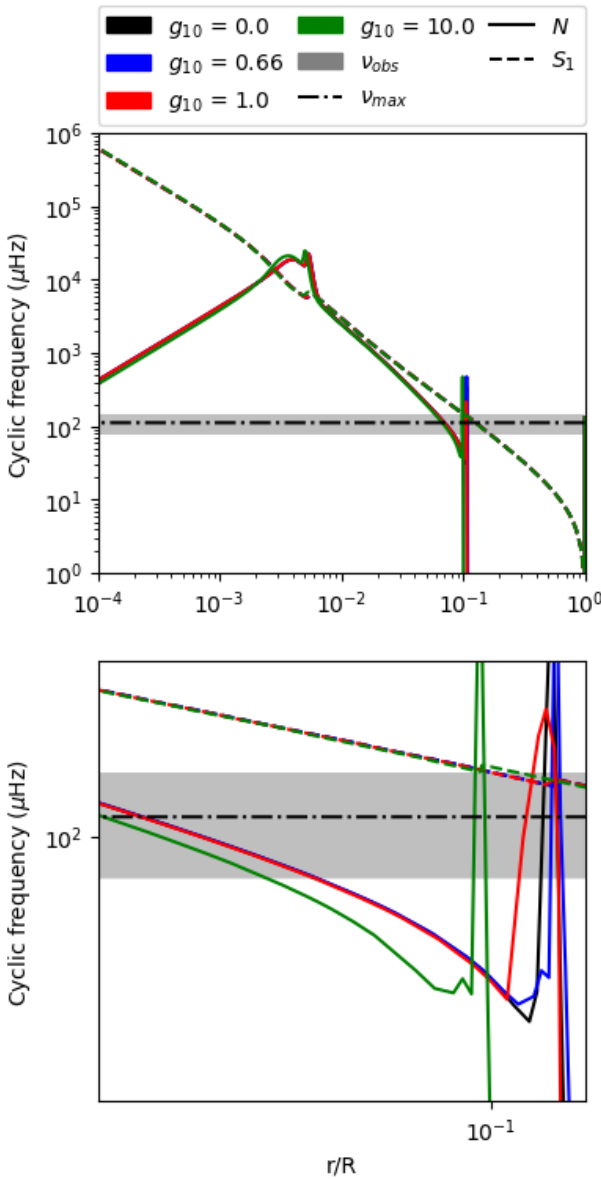


Figure 4.40: *Top:* Propagation diagram for models of KIC 3744043 with a range of axion-photon coupling strengths.

*Bottom:* Close view of the BCZ, showing a shift to lower fractional radius with increased coupling strength, in contrast to the ‘standard’ coupling strength taken from literature [2, 3] which results in a small contraction

We have sought to explain these observations in terms of the density of the inner regions of the star. During the helium flash, the release of energy from the ignition of nuclear reactions lifts the core degeneracy, causing it to expand (Section 2.1.4). This reduces the pressure, increasing  $N$  significantly. (Equation 2.27). We have therefore attempted to exploit this link between the pressure and  $N$  to better understand the observations described above. The explanation given here is incomplete, and due to time constraints there are several features which have not yet been fully explored.

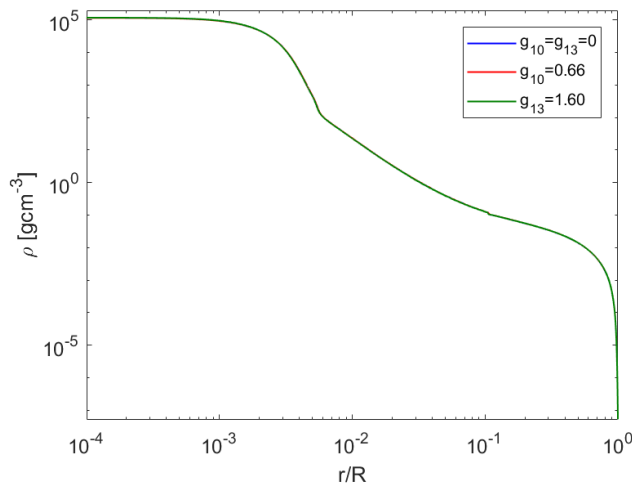
Equation 2.27 may be reduced by the application

of the ideal gas assumption ( $\chi_T = \chi_\rho = 1$ ;  $\chi_\mu = -1$ ):

$$N^2 = g^2 \frac{\rho}{p} (\nabla_{ad} - \nabla_T + \nabla_\mu), \quad (4.9)$$

but no simple scaling may be obtained, as in the ideal gas limit  $p \propto \rho$ . Further analysis is required to determine which of the remaining terms may dominate, but here we look simply for a correlation between  $\rho$  and  $N$ . The full density profile (Figure 4.41a) shows no deviations due to axion production in any region of the star. However, a closer view of the profile in the stellar core or hydrogen-burning shell reveals more (Figure 4.41b). In the core, the implementation of axion cooling by processes with coupling to either photon or electrons increases the density. This may be explained in terms of the partial degeneracy of the core at this evolutionary stage (Section 2.1.4) as the additional energy losses cool the core and therefore increase its density [29]. The difference in scale of the effect due to the axion-photon or axion-electron processes is, at least superficially, sensible. Axion-electron processes dominate in the stellar core (Figure ??), resulting in a more significant effect. In the hydrogen-burning shell, the density shifts follow a different pattern, matching that observed for the radial position of the BCZ, above (Figure 4.37). This appears to be suggestive of a correlation between  $\rho$  in this region and  $N$ , but no explanation of the change in density due to the energy loss processes is clear.

The observations were repeated for the models with higher levels of axion-electron (Figure 4.44) or axion-photon (Figure 4.43) coupling implemented. In all cases, an increased coupling strength increased the core density, while the density of the hydrogen burning shell followed the same order as the BCZ in the corresponding propagation diagram. All the available material therefore demonstrates that an increase in H-shell density corresponds to an increase of  $N$ . This reduces the size of the low-frequency evanescent region, shifting the base of the convective region to a higher fractional radius. This seems somewhat counter-intuitive, as one may expect an increased H-shell density to correspond to a reduction in its size, and therefore for the convective region to migrate to lower radii, and the full effects of this process on the stellar structure have not yet been explored



(a) Full density profile.

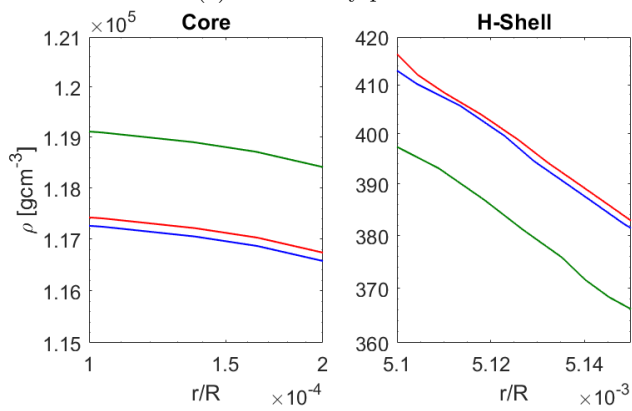
Figure 4.41: Density profiles for models of KIC 3744043. Axion production has been implemented with no axion production (blue), axion production due to photon coupling with  $g_{a\gamma} = 0.66 \times 10^{-10} \text{ GeV}^{-1}$  (red) and axion production due to electron coupling with  $g_{ae} = 1.60 \times 10^{-13}$  (green).

Figure 4.41: Density profiles for models of KIC 3744043. Axion production has been implemented with no axion production (blue), axion production due to photon coupling with  $g_{a\gamma} = 0.66 \times 10^{-10} \text{ GeV}^{-1}$  (red) and axion production due to electron coupling with  $g_{ae} = 1.60 \times 10^{-13}$  (green).

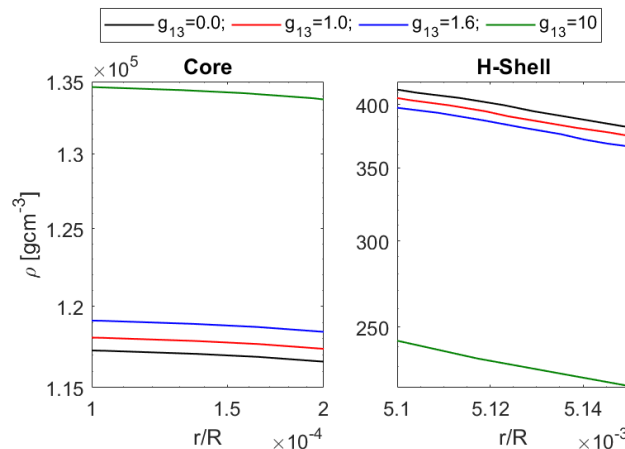


Figure 4.42: Close view density profile for the core and hydrogen burning shell with a range of axion-electron coupling strengths.

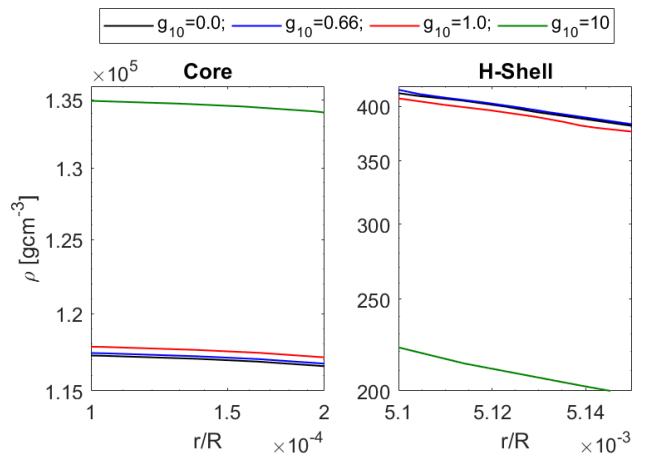


Figure 4.43: Close view density profile for the core and hydrogen burning shell with a range of axion-photon coupling strengths.

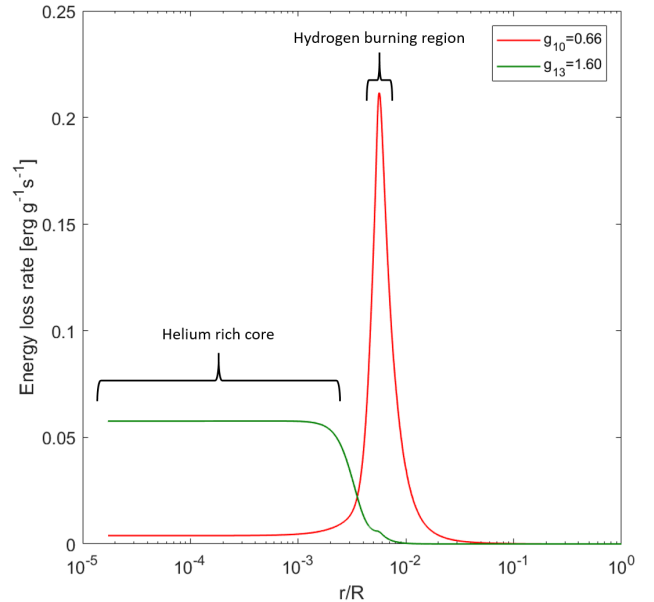


Figure 4.44: Energy loss rate profile for axion production processes with ‘standard’ coupling to photons (red) and electrons (green). The positions of the inert helium core and the hydrogen burning shell are (approximately) indicated, showing the clear dominance of the axion-electron processes in the core and axion-electron processes in the shell.

Care was taken in the selection of the individual profiles between which to compare the different axion cooling implementations (Section 3.9). In short, the deviation of  $\Delta\nu$  and  $\nu_{max}$  from that of the observed star was minimised. From the asteroseismic scaling relations (Equations 2.23 to 2.25), this approach limits the differences in the stellar mass, radius and luminosity for the same effective temperature. The resolution of the profiles obtained in the modelling process was insufficient to allow the values to be matched precisely, introducing a possible systematic effect to the comparisons of the stellar properties. Initial investigations, however, appear to indicate that these deviations are

not the source of the effects described above. In both models with standard axion cooling implemented (Figures 4.37 and 4.41b)  $\Delta\nu$  and  $\nu_{max}$  were slightly ( $\approx 1\%$ ) increased, compared to the model without axion production. This result does not correlate with the behaviours observed in the position of the BCZ, where the axion-photon and axion-electron models show opposing behaviour. The differences in  $T_{eff}$  between the models are much smaller ( $\approx 0.01\%$ ) and the reduced power in the scaling relations further reduces the effect. The total luminosity and core mass have also been considered, but again neither shows a correlation with the effects observed. The validity of the relationships between  $\rho$ ,  $N$  and the size of the evanescent region is also unclear. The assumptions which form the base of Equations 2.31 and 2.32 include a definition of the evanescent region as extending from the hydrogen burning shell to the base of the convective zone. The effects explored here consider the evanescent region at lower frequencies, and therefore higher radii.

Further investigation is certainly required – a repetition of the steps applied here to other model stars, as well as further consideration of other sources of a systematic effect must be completed before any meaningful conclusion may be drawn. However, the evidence presented here suggests a link between  $\rho$  in the hydrogen burning shell and  $N$ . It is not yet possible to say whether this relationship may be causal, or whether both parameters are simply responding to a change in another stellar property. There is currently no possibility of observing these effects in real stars, as they all take place at frequencies below the limits of current observations (shaded in Figures 4.37 - 4.40). This is discussed further in Section 4.9.3. A change in the extent of the convective zone may be expected to affect the luminosity of the RGB Bump. This study has found no clear evidence of such an effect, however (see further discussion in Section 4.6).

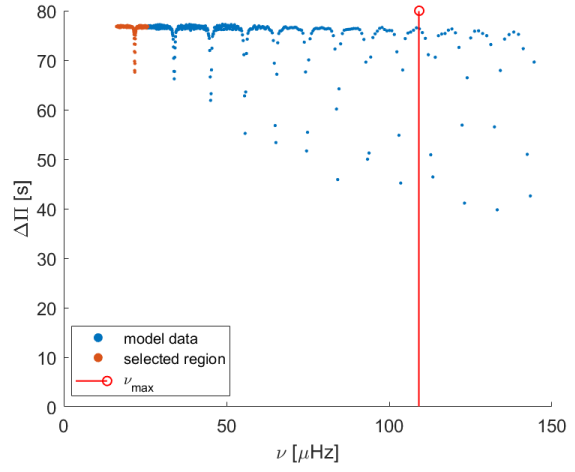
#### 4.9.2 Fits to the mixed mode pattern

In an attempt to better constrain the effects observed in the propagation diagrams, Lorentzian fits to individual troughs in the g mode period spacing pattern (Figure 4.45) were performed [48]. Each trough corresponds to the position in frequency of a pure p mode, and the change in the period spacing arises from the change of frequency caused by the interaction of this p mode with nearby g modes (Section 2.2). Producing these patterns relied upon individual mode frequencies modelled in GYRE (Section 3.3). The fit equation was

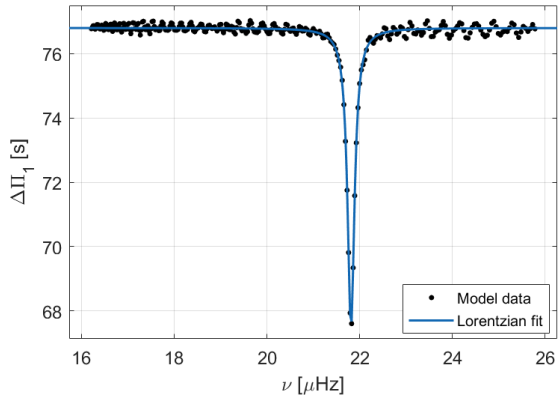
$$\frac{A}{1 + \left(\frac{\nu - \nu_c}{\Gamma}\right)^2} + \Delta\Pi_{as}, \quad (4.10)$$

where  $A$  is the amplitude and  $\nu_c$  is the central (p mode) frequency of the trough, and  $\Delta\Pi_{as}$  is the asymptotic period spacing, which sets the vertical offset of the pattern. The width of the Lorentzian,  $\Gamma$ , is related to the strength of the coupling between the p and g modes [48]. A decrease in the size of the evanescent region,

increasing the mode coupling, should correspond to an increase of  $\Gamma$ .



(a) The full period spacing pattern modelled, showing the selected low-frequency trough to which the most revealing Lorentzian fits were performed. The red stem indicates the position of  $\nu_{max}$



(b) Example Lorentzian fit to the selected low-frequency trough. The fit applied follows Equation 4.10.

Figure 4.45: The period spacing pattern obtained from a model of KIC 3744043 with no axion cooling implemented.

In the first instance, fits were performed to the troughs nearest to  $\nu_{max}$  for the seven modelled stars. As mentioned above (Section 4.9.1) oscillation frequencies are only observed in a small range about  $\nu_{max}$ , so this approach provided the best possibility of a comparison to observational data, as well as an opportunity to probe the changes in the BCZ peak observed in the propagation diagrams (e.g. Figure 4.37). However, the uncertainties on the value of  $\Gamma$  (obtained from the 95% confidence bounds of the fit) were too large to allow any conclusion to be drawn (Figure 4.46).

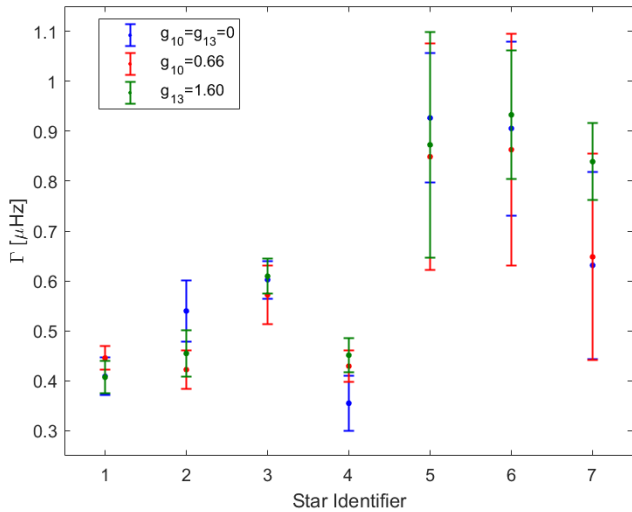


Figure 4.46: The Lorentzian fit width obtained from the troughs closest to  $\nu_{max}$  for models of seven low-luminosity red giants. The ‘Stellar Identifier’ given here corresponds to that in Table 3.1. No consistency between the widths with different axion cooling implementations is apparent, and the error bars cover the full range of measurements.

As previously discussed, the effect of axion production on the size of the evanescent region is much larger at lower frequencies. For this reason, fits to the lowest frequency trough for each star were obtained.

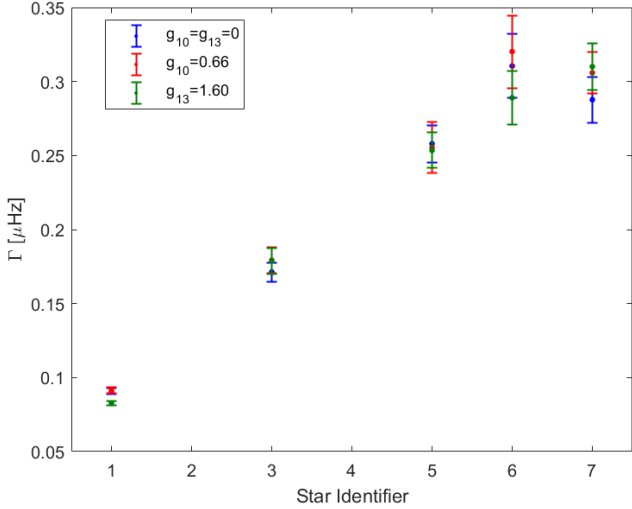


Figure 4.47: The Lorentzian fit width obtained from the lowest frequency troughs for models of seven low-luminosity red giants. The ‘Stellar Identifier’ given here corresponds to that in Table 3.1. No consistency between the widths with different axion cooling implementations is apparent, and the error bars cover the full range of measurements, except in the case of Star 1 (KIC 3744043). This star is discussed further in the text.

In all but one star, the uncertainties were once again too large to allow a conclusion. In the case of KIC 3744043, however, the Lorentzian width was far better constrained. Fits of the other troughs in the pe-

riod spacing pattern of this star were also performed, but again the uncertainties on their widths prevent meaningful conclusion.

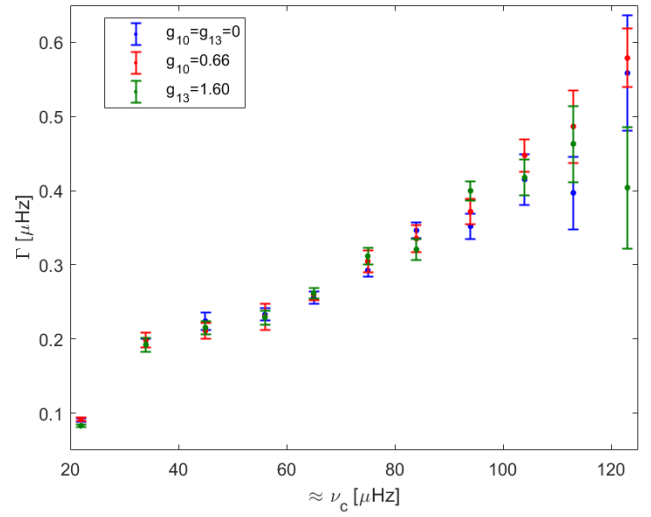


Figure 4.48: The Lorentzian fit width obtained from all the troughs in the model of KIC 3744043. The horizontal axis gives and identifying frequency for the position of the trough considered. No consistency between the widths with different axion cooling implementations is apparent, and the error bars cover the full range of measurements for all troughs beyond the lowest frequency case.

In comparison to previously published values (for example [48]), all the period spacing patterns obtained here show troughs which are several times narrower. There are several caveats to this comparison, however, including the difficulty in determining which ‘width’ of the Lorentzian fit is referred to in literature. Furthermore, the published results are generally confined to the consideration of the evanescent region at higher frequencies than considered here, making a direct comparison impossible. Differences in the modelled surface physics also play a role [11] and in the simplified model atmosphere employed, the mixing regime chosen has an effect on the structure of some regions of the star (Section 3.7.2). An offset towards higher frequencies may also be expected, as this has previously been observed in the Sun [?]. With so little precise data available from this study, further comment is not possible, but it is clear that the potential of this technique has not yet been fully explored. The larger effects observed in the models with high levels of axion coupling (Figures 4.39 and 4.40) may be used as test cases to refine the fitting process and to clarify the relationship between the width,  $\Gamma$ , and the size of the evanescent region. If sufficient improvements can be made, this technique offers the opportunity to robustly extract the behaviour of the evanescent region and so to better probe the changes in the internal structure related to axion production.

### 4.9.3 Observing Period Spacing <sup>K</sup>

Investigation into the difference between consecutive frequency modes of primary angular degree (the period spacing) and the subsequent trend in its variation as a function of frequency was investigated using data from long cadence Kepler observations of low-mass, low-luminosity RGB stars processed with DIAMONDS code to perform the peak bagging and extract individual frequency modes [49]. It is of particular interest to study RGB stars because due to their more evolved state, g modes are brought to higher frequencies (within the region of p modes), which shrinks the evanescent region causing the modes to mix. The data was presented as a series of frequencies corresponding to different modes of resonance; those of interest for this analysis corresponded to angular degrees,  $l = 1$ , and azimuthal orders,  $m = 0$  as they depict resonances from mixed modes probing stellar interiors. The sample of stars considered from the initial 19 for which data was available were chosen based upon the highest availability of these specific modes. As can be seen in Figure 4.49, which shows the period spacing plotted as a function of frequency for a star within the sample, it is immediately evident that the data set was largely incomplete with many consecutive modes missing. This issue ran across the entire data set concluding the ultimate unsuccessful nature of further data analysis.

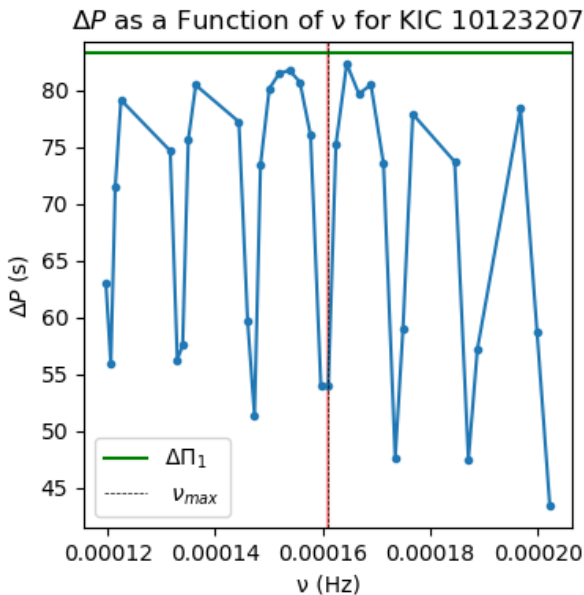


Figure 4.49: The plot includes the period spacing data set omitting any data points above the asymptotic g-mode value. The green line depicts the value of the asymptotic g-mode period spacing whilst the dashed black line marks  $\nu_{max}$ . The red shaded region shows the uncertainty in the determination of this frequency value. It must be noted that the percentage uncertainty in the spacing was at most 0.002% therefore they have been omitted from the plot.

Figure 4.49 shows the deviations of the period spacing from the asymptotic g mode value shown by the

green line. The recurrent pattern of spikes observed is a direct result of the coupling between g and p modes causing mode bumping to occur. This has the effect of decreasing the spacing between adjacent mixed modes. The extent of the coupling strength determines the width of the spikes. Given the structure of evanescent zones in stars is expected to change dependent on the effects of axion cooling, and that the nature of this structure determines the strength of the coupling, the motivation behind this line of inquiry was formed. It follows that fitting Lorentzian profiles to the spikes in the plots and generating values for the width of the fits to compare with values obtained from similar analysis on the data from MESA and GYRE outputs would enable a method of producing evidence to validate the theory of axion cooling in these stars.

Initially the isolation of individual spikes was attempted automatically. This produced unsatisfactory results as a consequence of the aforementioned incomplete nature of the data set, which gave rise to a sharp and scattered distribution of data points. This saw local maxima occurring between individual data points, which disjointed the smoothing process when identifying these characteristic dips. Following this, a manual approach was taken to obtain the spikes after which Lorentzians profiles were fit. The results of the fits were below par following the same reasoning as the other difficulties encountered.

Treating this with any further rigour was decided against as with consideration of the time constraints on the project and as upon comparison with the data from the stellar models, the frequency regions within which any variation between the models with and without axion cooling were far below the range of the observed data. Furthermore, the manual identification of the spikes reduces the reproducibility of the results as it adds an element of subjectivity to the analysis, which is not favoured.

## 4.10 Sound Speed Profiles <sup>H</sup>

When attempting to model the interior of a star, a profile of how the sound speed varies throughout its different zones can be a useful means of visualising the stars internal structure. Typically, the speed of sound in a medium is considered to have the following relationship

$$c_s \propto \frac{P^{1/2}}{\rho} \propto \frac{T^{1/2}}{\mu}$$

where  $P$  is pressure,  $\rho$  is density,  $T$  is temperature and  $\mu$  is mean molecular weight. The proportionality between these values means. Further, it provides the possibility of comparing models with and without additional axion cooling; two stars of identical initial composition at a specified point of evolution may prove to be different internally given that one of them has experienced an additional form of cooling.

During initial investigations, a small amount of work was done to compare models using sound speed profiles. The models tested were of masses

$0.8 M_{\odot} - 2 M_{\odot}$  in increments of  $0.1 M_{\odot}$ , with each model having a solar-like chemical composition. While the idea was to compare a model of each mass with its axion-cooled counterpart (using axion-photon coupling) at several stages of evolution, the points of comparison were defined poorly. For example, for a point on the RGB the MESA profiles compared were each from an arbitrary point at the centre of each models lifetime on the RGB. This was too vague for a valid comparison to be made. During the second cycle, in order to better analyse the data, the models considered were restricted to the low-luminosity RGB to allow for a more careful approach. The models of interest were considered to be at the same stage of evolution when they had the same values of  $\nu_{max}$  and  $\Delta\nu$  within limits, with MESA set to output a profile at this point. Theoretically when this occurs the two models can be considered to be most similar.

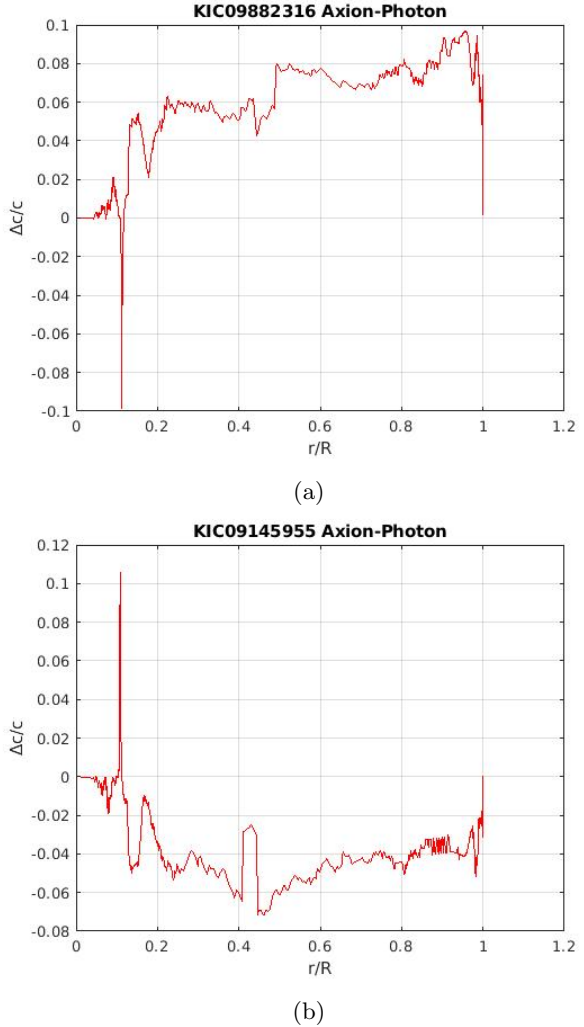


Figure 4.50: Sound speed profiles showing the difference between models KIC09882316 and KIC09145955 with and without axion-photon coupling.

In Figure 4.50, we represent the sound speed profiles showing the differences caused by the inclusion of axion-photon coupling. In these plots,

$$\frac{\Delta c}{c} = \frac{(c_{non-axion} - c_{axion})}{c_{non-axion}}$$

There are a couple of features in all the plots caused by star structure. At a fractional radius of 0.1 we observe a sharp spike, due to the edge of the stars core. The sharp decrease in temperature and pressure that occurs as you progress from the core into the surrounding shell causes a rapid decrease in sound speed. As the two models being compared dont match up perfectly, this change happens at a slightly different radius, causing one model to temporarily have a vastly different sound speed to the other, hence the spike. The second common feature of note is the dip at a fractional radius of 0.4, shown more clearly in the plot for the model KIC09145955. This coincides roughly with the beginning of the convective envelope.

These plots can be considered a representative sample of the seven produced, as they all take the rough form of one of the two. Curiously, when the two plots

A group of nineteen low-luminosity RGB stars observed by Kepler were investigated by [74], providing us with a set of models for which the addition of axion cooling can be tested as described above. Of the nineteen available, seven were sampled over a mass range of roughly  $0.9 M_{\odot} - 1.4 M_{\odot}$ , with varying chemical compositions, radii etc. Three simulations were done of each model within MESA; one with the standard processes, one with axion-photon coupling and one with axion-electron coupling. The coupling constants used were the accepted values for this report, with the axion-photon coupling constant as  $g_{10} = 0.66$  and the axion-electron coupling constant as  $g_{13} = 1.6$ .

above are compared one notices that they are almost identical and are simply reflected in the x-axis. This is an unexpected result; if axion cooling were to have a noticeable effect on a star, we could expect the effect to be consistent over a group of relatively similar stars. The plot for model KIC09145955 suggests a generally higher sound speed in the star with axion-photon coupling, while the plot for model KIC09882316 suggests the opposite. We must consider possible explanations for this result. A possible conclusion that one immediately comes to is that the comparison is being made between two stars that are in fact at different stages of evolution. This may result in the more evolved star having a noticeable decrease in temperature throughout, leading to a lower net sound speed than the less evolved model. The differences are of the magnitude of 1% which is possibly what you'd expect from an evolving star.

Another factor worth consideration is how MESA creates profiles. A profile is made up of a number of mesh points, each of which accounts for a zone of the star. Each profile has a different number of mesh points, as sometimes a zone is designated a single mesh point while some are split into multiple mesh points. Therefore, when comparing two mesh points between models it's possible that they do not correspond to the same zone, as the zones in each model are likely divided differently. A result of this is the jagged appearance of the produced plots as zones of varying size are compared. Lastly, it should be noted that changes in the sound-speed profile will be compensated for by changes in the chemical composition, and the overall composition of a star may change how the implementation of axion-cooling has an effect.

Profiles produced using similar means can be found in [75]. They show the effect of a varying axion-photon coupling constant on the sound speed. There is shown to be a common trend; the models with axion-cooling experience increased sound speed in and at the edge of the core while there is a significant decrease nearer the surface. Another difference in these results is roughly an order of magnitude in the the values of  $\Delta c/c$ . It should be noted that the models used in this case were solar-like and on the main sequence, closer to the Sun than a red giant, which may explain this. The profiles in this report show similarities to those produced by Vinyoles et al. (2015) at a fractional radius of 0.4 and above, though it still stands that half of the plots here see negative values of  $\Delta c/c$  rather than positive. Profiles for solar models with axion cooling can also be found in [76], which show similar results around the core though no change nearer the star surface. Regardless, both of these papers show a common trend, reinforcing the notion that there was error in the production of the profiles in this report and making it difficult to draw conclusions from these profiles.

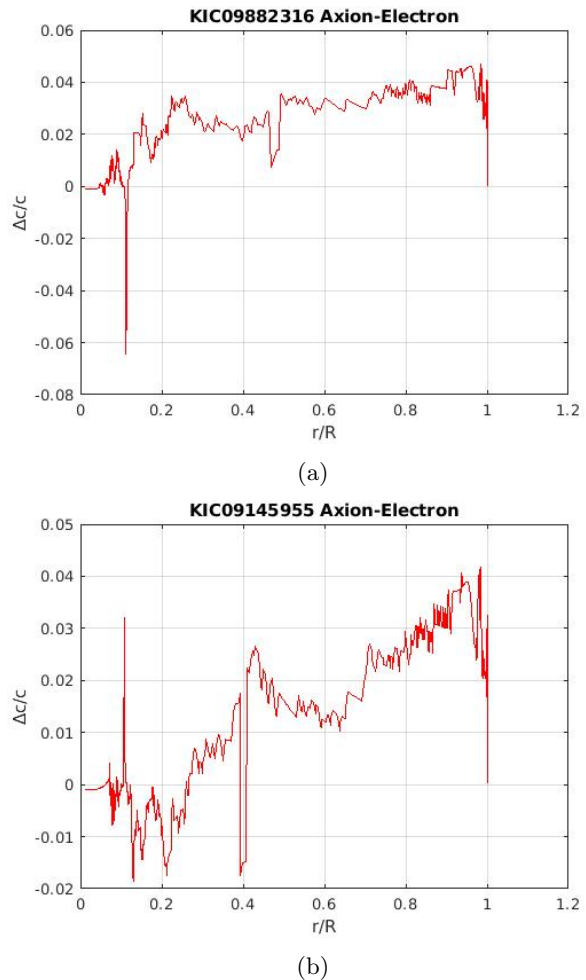


Figure 4.51: Sound speed profiles showing the difference between models KIC09882316 and KIC09145955 with and without axion-electron coupling.

Unlike the axion-photon coupling models, when comparing the models with and without axion-electron coupling we do see a common trend in each profile. The same features can be seen in the plots, however they all portray positive values of  $\Delta c/c$  throughout the whole the star. This would suggest that all the models see a decrease in the magnitude of sound-speed when axion-electron coupling is applied. Theoretically, axion-cooling would increase the energy loss from the core, resulting in an increase in the burning of fuel and an overall increase in the luminosity of the star. Given this increase in burning, it seems unlikely that the sound speed would decrease in this region, as increased burning would result in a higher temperature around the core. With regards to the magnitude of values observed, they appear to be roughly half of that seen in the case of axion-photon coupling.

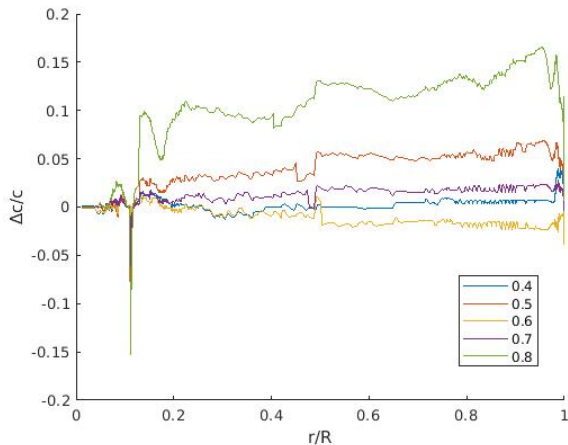


Figure 4.52: Sound speed profile investigating how varying the axion-photon coupling constant affects the difference between models with and without axion-photon coupling, for KIC09882316.

In order to perform a simple check on whether the method being used to create the above profiles is accurate, six models of KIC09882316 were created; one without axion-cooling, and five with axion-photon coupling constants ranging between 0.4 and 0.8. Figure 4.52 shows the comparison between the non-axion cooled model with the others on the same axes. With a large coupling constant youd expect a greater variation and therefore a larger plot magnitude, and while a constant of 0.8 yielded values of  $\Delta c/c$  of 0.15 compared to a constant of 0.4 providing a  $\Delta c/c$  of roughly zero, the results are muddled inbetween (e.g.  $g_{10} = 0.7$  had less of an effect than  $g_{10} = 0.5$ ). Secondly, theres a mix of plots displaying a majority of negative values and a majority of positive values. Given that all the models in this case had the same chemical composition, this can be removed as a potential cause of this occurrence. However it is apparent that there is fault in the comparison of the models.

Its obvious that the results shown here are unreliable, potentially due to a number of variables. A fitting conclusion is that the comparison of models produced within MESA may not be the most reliable way of profiling in a way that will produce notable results. Despite this, its clear that there is some effect had by the implementation of axion-cooling on a magnitude of 1%, though describing the effect much more beyond this proves difficult due to the spread of results shown above.

# Chapter 5

## Conclusions

### 5.1 Luminosity of RGB Bump and RC<sup>F</sup>

A simulated population of stars was used alongside observational data to estimate the luminosities of the RGB bump and the RC, producing values of  $L_{\text{Bump}} = (1.5854 \pm 0.0003)$  dex and  $L_{\text{Clump}} = (1.700 \pm 0.041)$  dex respectively. Figure 4.26 demonstrates that at the moment no conclusions can be drawn with respect to the axion coupling strength.

The uncertainty on the observed value of  $L_{\text{Clump}}$  includes all the models which were produced and as such cannot be used to constrain the axion coupling strength. However, it is estimated that with the release of Gaia DR2, the error on  $L_{\text{Clump}}$  will likely be reduced to a value of approximately 0.01, allowing further constraints to be made.

The uncertainty on  $L_{\text{Bump}}$  is incredibly small due to the large simulated population which was used. No models fit within this range as such indicating an issue in the method used to determine  $L_{\text{Bump}}$ . Gaia's DR2 will provide a large increase in the number of stars on which precise astrometric data is available, it will be possible to provide an estimate for  $L_{\text{Bump}}$  from observed data and by extension place a more realistic constraint on axion coupling strength. Moreover, the estimation of  $L_{\text{Bump}}$  from observed data will provide an indication of how effective the method used in Section 3.5.2 was, possibly indicating further adjustments to the method in order to improve simulated estimates.

### 5.2 TRGB Summary<sup>C,E</sup>

The TRGB was expected to be a prime target for identifying and constraining axion cooling in solar-like oscillators and so it proved, but ultimately observational data, and the uncertainties that come with it, proved to be limiting when drawing conclusions. The globular cluster identified for investigation, M4, was not able to produce any immediate comparison to model tip luminosities as it had no stars near the expected tip. Whilst different globular clusters could be used, one that is sufficiently well resolved containing stars at or about the TRGB is unlikely to be found. The tip

luminosity therefore had to be estimated from the data available.

Comparisons of the time density of the modelled RGB with the star density of the M4 data were used to estimate the luminosity of the TRGB of M4. Somewhat unsurprising given the visible deviation about the fit used, the tip luminosity could not be constrained to an accuracy that allowed differentiation between models of varying axion-photon coupling strength. The tip luminosity was found to be  $(3.39 \pm 1.10)$  dex. To find a more accurate estimate of the tip, interpolation could be used to better fit the time-density and number-density plots. An even more accurate estimate of the tip could be found using a Monte Carlo simulation, however time constraints did not allow for this to be done in this investigation.

Using a power law that relates the bolometric magnitude of the TRGB of a cluster to its metallicity provided an estimate of the TRGB luminosity for M4 of  $(3.386 \pm 0.035)$  dex. This luminosity is in fact greater, even, than that predicted with the largest reasonable axion-photon coupling strength,  $g_{10} = 0.80$ . Whilst this might imply that axion-photon coupling is stronger than current research might suggest, it is more likely that this suggests that both axion-photon and axion-electron coupling contributes an increase in the luminosity of the TRGB, the latter only being lightly investigated here. However, given the recent and somewhat unverified nature of this power law, a more direct constraint of axion coupling would be preferential. Furthermore, other properties of the star may compensate for the increase in TRGB luminosity, which would be worth investigating following the release of Gaia DR2 and more available data.

Using the I-band magnitude of the TRGB of M5 found by Vieux et al. (2013), an upper bound of  $g_{10} < 1.5$  was found. The luminosity of M5, converted from the Vieux et al. (2013) I-band magnitude, was compared with models of varying axion-photon coupling strength. The upper bound was found by integrating the combined probability distribution and finding the 68% confidence level. The predicted axion-photon coupling strength was found to be much less than this ( $g_{10} = 0.267$ ) however errors on both the models and the observed tip meant that the coupling strength could not be constrained to anything like this accuracy. As the errors on the theoretical and observed tip both arise from observational errors, tighter constraints should be able to be placed on axion-photon coupling strength going forward with the improved accuracy of future observing missions.

### 5.3 Asteroseismic HRD Conclusion<sup>I</sup>

By using real, well observed clusters in section 4.8.2 as well as creating groups of stars which could be considered a cluster with their M and Z properties in section 4.8.3, an upper limit of  $g_{10} = 1.5$  has been determined.

The synthetic clusters produced with more accurate data show a more apparent fit to some models with lower axion cooling strengths ( $g_{10} \approx 0.66 - 1.00$ ), however due to the uncertainty in the mixing scheme used these values may not be appropriate.

To improve on any limits approximated, a better understanding and model of what mixing scheme is present in the stars must be found and used. Uncertainties on the data for properties such as mass and metallicity will also improve any fits with populated data. Gaia and its second data release should improve the accuracy of any data that can be used, as well as providing an increased sample size to fit to models, which will improve model fits as well.

Future research into such models and data with improved accuracy holds a lot of promise for research into the presence of axions, with any differences due to axion cooling then being able to be compared with previous research and results from other papers, such as Ayala et al. (2014) [55].

## 5.4 Low-Luminosity RGB Summary<sup>A,D</sup>

Investigation into the affects of mixed mode period spacing for stars on the low-luminosity RGB has yielded promising results, with room for further research. In particular, they have shown to be good probes of the proposed scheme of axion-electron coupling.

Detailed analysis of the evanescent region (Section 4.9.1) should be repeated for other stars pre-RGB bump, where the hypothetical effects due to axions-electron processes appear to dominate in the core. Lorentzian fitting to the modelled p-g coupled modes should be further refined; current fits of the return widths with prohibitively large errors for modes about  $\nu_{max}$ , as well as those at lower frequencies. This is problematic when comparing between models and subsequently to observed data.

Finally, better modelling of the stars is required. This study assumes the same model initial conditions for varying coupling strengths. However, if axion cooling has a notable effect on the period spacing due to losses in the core, the models would have to be adjusted. Further consideration of the mixing scheme implemented in the stellar models is also required, as the effects on internal structure may mask or exaggerate and effects apparently due to axions. Initial conditions for the models could be changed to obtain a better fit for a range of axion-electron coupling strengths. With better models, the effects of axionic energy-loss on the size of the evanescent region can be better constrained.

## 5.5 Limitations of Current Data<sup>K</sup>

The issues encountered during the analysis of the observed data raises the reality of the importance of the resolution and limitations of data currently available, such as that from the Kepler/K2 and CoRoT missions, poses on the field of asteroseismology and ability to probe the interior of stars. The difficulty in detecting these particular modes of resonance lies in the high level of complexity of the power density spectrum for solar-like oscillators that incorporates signals from granulation on the surface, shot noise, instrumental noise as well as the stochastically excited oscillation modes [77]. In particular relation to observing the  $l = 1$  modes and detecting axion cooling effects, it is necessary to detect modes in low frequency ranges of the order of  $10\text{ }\mu\text{Hz}$ . The photometric variations corresponding to these oscillations are too low in amplitude to resolve above background noise signals within current data leading to the question of what must be changed in order to make the methods of detection outlined in this paper more robust.

Lengthening the time of observation would increase the signal to noise ratio therefore allowing the detection of lower amplitude resonance modes in the frequency power spectrum. These modes tend to lie toward the extrema from  $\nu_{max}$  in these plots. This is exhibited in Figure 4.49 whereby around  $\nu_{max}$ , the plot is well populated however further from this point gaps between data points can be seen. According to the Libbrecht formula [78] which states that the uncertainty on frequency measurement is inversely proportional to the root of the length of observation (see Equation 5.1).

$$\sigma_\nu \propto \frac{1}{\sqrt{T_{obs}}} \quad (5.1)$$

Space missions like PLATO which propose total 6.5 years of observations, exceeding that of Kepler, combined with an assortment of cameras with far smaller apertures (120 mm) compared with Keplers large telescope, will serve to enhance the quality of observed data [79].

It is expected that the number of stars with solar-like oscillations that future space missions such as PLATO and TESS will detect are  $2 \times 10^5$  and  $3 \times 10^5$  respectively [78]. Both missions promise to survey stars 30-100 times brighter than those studied by Kepler [80] which will aid in reducing the photon noise observed as this was identified as a major contributor to noise in the Kepler data set as opposed to instrumental noise[81]. These factors will have the common effect of drastically increasing the inventory of targets which supply useful data. PLATO will enjoy a Nyquist frequency of  $833\text{ }\mu\text{Hz}$  sitting a degree higher than Kepler which had  $278\text{ }\mu\text{Hz}$  [82] which will uncover a broader range of oscillation frequencies.

## Acknowledgements

We thank Andrea Miglio for his role as project supervisor, providing useful feedback throughout this investigation, regarding our lines of enquiry and subsequent findings. We would also like to thank Warrick Ball and Guy Davies for their roles as subgroup supervisors, providing advice and feedback regarding stellar modelling and data analysis respectively. Finally, we are grateful to the HiROS research group for allowing us access to the BiSON simulation machines, which was used extensively for producing models using MESA and GYRE.

# References

- [1] T. M. Brown and R. L. Gilliland, “Asteroseismology,” *Annu. Rev. Astron. Astrophys.*, vol. 32, no. 1, pp. 37–82, 1994.
- [2] V. Anastassopoulos *et al.*, “New cast limit on the axion-photon interaction,” *Nature Phys.*, vol. 13, pp. 584–590, 2017.
- [3] M. Giannotti, I. G. Irastorza, J. Redondo, A. Ringwald, and K. Saikawa, “Stellar recipes for axion hunters,” *jcap*, vol. 10, p. 010, Oct. 2017.
- [4] G. G. Raffelt, “Astrophysical axion bounds,” *Lect. Notes Phys.*, vol. 741, pp. 51–71, 2008. [,51(2006)].
- [5] R. Kippenhahn and A. Weigert, *Stellar Structure and Evolution*. Springer Science & Business Media, Dec. 2012.
- [6] M. Schönberg and S. Chandrasekhar, “On the evolution of the Main-Sequence stars,” *Astrophys. J.*, vol. 96, p. 161, 1942.
- [7] J. Christensen-Dalsgaard, “On the red-giant luminosity bump,” *Mon. Not. R. Astron. Soc.*, vol. 453, no. 1, pp. 666–670, 2015.
- [8] B. Carroll and D. Ostlie, *An Introduction to Modern Astrophysics*. Pearson Addison-Wesley, 2007.
- [9] O. R. Pols, “Stellar structure and evolution.” Online, Sept. 2011.
- [10] O. Straniero, I. Dominguez, G. Imbriani, and L. Piersanti, “The chemical composition of white dwarfs as a test of convective efficiency during core helium burning,” *Astrophys. J.*, vol. 583, no. 2, pp. 878–884, 2003.
- [11] W. J. Chaplin and A. Miglio, “Asteroseismology of Solar-Type and Red-Giant stars,” *Annu. Rev. Astron. Astrophys.*, vol. 51, no. 1, pp. 353–392, 2013.
- [12] D. Bossini, “Asteroseismology of red giant stars: a tool for constraining stellar models.” December 2016.
- [13] T. R. Bedding, B. Mosser, D. Huber, J. Montalbán, P. Beck, J. Christensen-Dalsgaard, Y. P. Elsworth, R. A. García, A. Miglio, D. Stello, T. R. White, J. De Ridder, S. Hekker, C. Aerts, C. Barban, K. Belkacem, A.-M. Broomhall, T. M. Brown, D. L. Buzasi, F. Carrier, W. J. Chaplin, M. P. Di Mauro, M.-A. Dupret, S. Frandsen, R. L. Gilliland, M.-J. Goupil, J. M. Jenkins, T. Kallinger, S. Kawaler, H. Kjeldsen, S. Mathur, A. Noels, V. S. Aguirre, and P. Ventura, “Gravity modes as a way to distinguish between hydrogen- and helium-burning red giant stars,” *Nature*, vol. 471, pp. 608–611, Mar. 2011.
- [14] B. Mosser, O. Benomar, K. Belkacem, M. J. Goupil, N. Lagarde, E. Michel, Y. Lebreton, D. Stello, M. Vrard, C. Barban, and Others, “Mixed modes in red giants: a window on stellar evolution,” *Astron. Astrophys. Suppl. Ser.*, vol. 572, p. L5, 2014.
- [15] S. Deheuvels and E. Michel, “Constraints on the structure of the core of subgiants via mixed modes: the case of HD 49385,” *Astron. Astrophys. Suppl. Ser.*, vol. 535, p. A91, 2011.
- [16] B. Mosser, C. Pinçon, K. Belkacem, M. Takata, and M. Vrard, “Period spacings in red giants (corrigendum),” *Astron. Astrophys. Suppl. Ser.*, vol. 607, p. C2, 2017.
- [17] R. D. Peccei and H. R. Quinn, “CPConservation in the presence of pseudoparticles,” *Phys. Rev. Lett.*, vol. 38, no. 25, pp. 1440–1443, 1977.
- [18] G. G. Raffelt, “Axions,” in *Stars as Laboratories for Fundamental Physics: The Astrophysics of Neutrinos, Axions, and Other Weakly Interacting Particles*, pp. 524–544, University of Chicago Press, May 1996.
- [19] R. D. Peccei and H. R. Quinn, “Constraints imposed byCPconservation in the presence of pseudoparticles,” *Phys. Rev. D Part. Fields*, vol. 16, no. 6, pp. 1791–1797, 1977.
- [20] J. Preskill, M. B. Wise, and F. Wilczek, “Cosmology of the invisible axion,” *Phys. Lett. B*, vol. 120, no. 1–3, pp. 127–132, 1983.
- [21] S. Borsanyi, Z. Fodor, J. Guenther, K.-H. Kampert, S. D. Katz, T. Kawanai, T. G. Kovacs, S. W. Mages, A. Pasztor, F. Pittler, J. Redondo, A. Ringwald, and K. K. Szabo, “Calculation of the axion mass based on high-temperature lattice quantum chromodynamics,” *Nature*, vol. 539, pp. 69–71, Nov. 2016.
- [22] M. M. Miller Bertolami, B. E. Melendez, L. G. Althaus, and J. Isern, “Revisiting the axion bounds from the galactic white dwarf luminosity function,” *JCAP*, vol. 1410, no. 10, p. 069, 2014.
- [23] N. Viaux, M. Catelan, P. B. Stetson, G. G. Raffelt, J. Redondo, A. A. R. Valcarce, and A. Weiss, “Neutrino and axion bounds from the globular cluster M5 (NGC 5904),” *Phys. Rev. Lett.*, vol. 111, p. 231301, Dec. 2013.

- [24] G. G. Raffelt, “Particles interacting with electrons and baryons,” in *Stars as Laboratories for Fundamental Physics: The Astrophysics of Neutrinos, Axions, and Other Weakly Interacting Particles*, pp. 89–116, University of Chicago Press, May 1996.
- [25] G. G. Raffelt, “Two-Photon coupling of Low-Mass bosons,” in *Stars as Laboratories for Fundamental Physics: The Astrophysics of Neutrinos, Axions, and Other Weakly Interacting Particles*, pp. 165–192, University of Chicago Press, May 1996.
- [26] A. Friedland, M. Giannotti, and M. Wise, “Constraining the Axion-Photon coupling with massive stars,” *Phys. Rev. Lett.*, vol. 110, no. 6, 2013.
- [27] A. Heger, A. Friedland, M. Giannotti, and V. Cirigliano, “THE IMPACT OF NEUTRINO MAGNETIC MOMENTS ON THE EVOLUTION OF MASSIVE STARS,” *Astrophys. J.*, vol. 696, no. 1, pp. 608–619, 2009.
- [28] G. Raffelt and A. Weiss, “Red giant bound on the axion-electron coupling reexamined,” *Phys. Rev. D Part. Fields*, vol. 51, pp. 1495–1498, Feb. 1995.
- [29] G. G. Raffelt, *Stars as Laboratories for Fundamental Physics: The Astrophysics of Neutrinos, Axions, and Other Weakly Interacting Particles*. University of Chicago Press, May 1996.
- [30] G. G. Raffelt, “The energy-loss argument,” in *Stars as Laboratories for Fundamental Physics: The Astrophysics of Neutrinos, Axions, and Other Weakly Interacting Particles*, pp. 1–22, University of Chicago Press, May 1996.
- [31] G. G. Raffelt, “Anomalous stellar energy losses bounded by observations,” in *Stars as Laboratories for Fundamental Physics: The Astrophysics of Neutrinos, Axions, and Other Weakly Interacting Particles*, pp. 23–88, University of Chicago Press, May 1996.
- [32] B. Paxton, L. Bildsten, A. Dotter, F. Herwig, P. Lesaffre, and F. Timmes, “MODULES FOR EXPERIMENTS IN STELLAR ASTROPHYSICS (MESA),” *Astrophys. J. Suppl. Ser.*, vol. 192, no. 1, p. 3, 2010.
- [33] A. Choplin, A. Coc, G. Meynet, K. A. Olive, J.-P. Uzan, and E. Vangioni, “Effects of axions on population III stars,” *Astron. Astrophys. Suppl. Ser.*, vol. 605, p. A106, 2017.
- [34] R. H. D. Townsend and S. A. Teitler, “GYRE: an open-source stellar oscillation code based on a new magnus multiple shooting scheme,” *Mon. Not. R. Astron. Soc.*, vol. 435, no. 4, pp. 3406–3418, 2013.
- [35] R. H. D. Townsend, “Namelist input files (5.1) — bitbucket.” [https://bitbucket.org/rhdtownsend/gyre/wiki/Namelist%20Input%20Files%20\(5.1\)](https://bitbucket.org/rhdtownsend/gyre/wiki/Namelist%20Input%20Files%20(5.1)), 2017. Accessed: 2018-3-13.
- [36] R. H. D. Townsend, “Understanding grids — bitbucket.” <https://bitbucket.org/rhdtownsend/gyre/wiki/Understanding%20Grids>, 2017. Accessed: 2018-3-13.
- [37] E. Vanhollebeke, M. A. T. Groenewegen, and L. Girardi, “Stellar populations in the galactic bulge,” *Astron. Astrophys. Suppl. Ser.*, vol. 498, no. 1, pp. 95–107, 2009.
- [38] K. Hawkins, B. Leistedt, J. Bovy, and D. W. Hogg, “Red clump stars and gaia: calibration of the standard candle using a hierarchical probabilistic model,” *Mon. Not. R. Astron. Soc.*, vol. 471, no. 1, pp. 722–729, 2017.
- [39] D. Bossini, A. Miglio, M. Salaris, M. Vrard, S. Cassisi, B. Mosser, J. Montalbán, L. Girardi, A. Noels, A. Bressan, A. Pietrinferni, and J. Tayar, “Kepler red-clump stars in the field and in open clusters: constraints on core mixing,” *Mon. Not. R. Astron. Soc.*, vol. 469, no. 4, pp. 4718–4725, 2017.
- [40] A. Maeder, “Stellar evolution. III - the overshooting from convective cores,” *Astron. Astrophys. Suppl. Ser.*, vol. 40, pp. 303–310, May 1975.
- [41] D. Bossini, A. Miglio, M. Salaris, A. Pietrinferni, J. Montalbán, A. Bressan, A. Noels, S. Cassisi, L. Girardi, and P. Marigo, “Uncertainties on near-core mixing in red-clump stars: effects on the period spacing and on the luminosity of the AGB bump,” *Mon. Not. R. Astron. Soc.*, vol. 453, no. 3, pp. 2291–2302, 2015.
- [42] M. Vrard, B. Mosser, and R. Samadi, “Period spacings in red giants,” *Astron. Astrophys. Suppl. Ser.*, vol. 588, p. A87, 2016.
- [43] T. B. A. M. A. for Space Telescopes (MAST), “KIC10 search.” <http://archive.stsci.edu/kepler/kic10/search.php?form=fuf>, 2016. Accessed: 2018-3-17.
- [44] F. D. Albareti, C. Allende Prieto, A. Almeida, F. Anders, S. Anderson, B. H. Andrews, A. Aragón-Salamanca, M. Argudo-Fernández, E. Armengaud, E. Aubourg, and et al., “The 13th data release of the Sloan Digital Sky Survey: First spectroscopic data from the SDSS-IV survey mapping nearby galaxies at Apache Point Observatory,” *apjs*, vol. 233, p. 25, Dec. 2017.
- [45] C. J. Lada, “The physics and modes of star cluster formation: observations,” *Philos. Trans. A Math. Phys. Eng. Sci.*, vol. 368, pp. 713–731, Feb. 2010.
- [46] G. Bertelli, A. Bressan, C. Chiosi, F. Fagotto, and E. Nasi, “Theoretical isochrones from models with new radiative opacities,” *Astron. Astrophys. Suppl. Ser.*, vol. 106, pp. 275–302, 1994.

- [47] F. Pérez Hernández, R. A. García, E. Corsaro, S. A. Triana, and J. De Ridder, “Asteroseismology of 19 low-luminosity red giant stars from kepler,” *Astron. Astrophys. Suppl. Ser.*, vol. 591, p. A99, 2016.
- [48] B. Mosser, M. J. Goupil, K. Belkacem, E. Michel, D. Stello, J. P. Marques, Y. Elsworth, C. Barban, P. G. Beck, T. R. Bedding, J. De Ridder, R. A. García, S. Hekker, T. Kallinger, R. Samadi, M. C. Stumpe, T. Barclay, and C. J. Burke, “Probing the core structure and evolution of red giants using gravity-dominated mixed modes observed with kepler,” *Astron. Astrophys. Suppl. Ser.*, vol. 540, p. A143, 2012.
- [49] E. Corsaro, J. De Ridder, and R. A. García, “Bayesian peak bagging analysis of 19 low-mass low-luminosity red giants observed with kepler,” *Astron. Astrophys. Suppl. Ser.*, vol. 579, p. A83, 2015.
- [50] B. Mosser, E. Michel, K. Belkacem, M. J. Goupil, A. Baglin, C. Barban, J. Provost, R. Samadi, M. Auvergne, and C. Catala, “Asymptotic and measured large frequency separations,” *Astron. Astrophys. Suppl. Ser.*, vol. 550, p. A126, 2013.
- [51] P. Gaulme, J. McKeever, J. Jackiewicz, M. L. Rawls, E. Corsaro, B. Mosser, J. Southworth, S. Mahadevan, C. Bender, and R. Deshpande, “Testing the asteroseismic scaling relations for red giants with eclipsing binaries observed by kepler,” Sept. 2016.
- [52] G. R. Davies and A. Miglio, “Asteroseismology of red giants: From analysing light curves to estimating ages,” *Astron. Nachr.*, vol. 337, no. 8-9, pp. 774–782, 2016.
- [53] G. Torres, J. Andersen, and A. Giménez, “Accurate masses and radii of normal stars: modern results and applications,” *Astron. Astrophys. Rev.*, vol. 18, no. 1-2, pp. 67–126, 2009.
- [54] T. L. Campante, N. C. Santos, and Mário J P F, *Asteroseismology and Exoplanets: Listening to the Stars and Searching for New Worlds: IVth Azores International Advanced School in Space Sciences*. Springer, Nov. 2017.
- [55] A. Ayala, I. Domínguez, M. Giannotti, A. Mirizzi, and O. Straniero, “Revisiting the bound on axion-photon coupling from globular clusters,” *Phys. Rev. Lett.*, vol. 113, p. 191302, Nov. 2014.
- [56] G. A. Verner, Y. Elsworth, W. J. Chaplin, T. L. Campante, E. Corsaro, P. Gaulme, S. Hekker, D. Huber, C. Karoff, S. Mathur, B. Mosser, T. Appourchaux, J. Ballot, T. R. Bedding, A. Bonanno, A.-M. Broomhall, R. A. García, R. Handberg, R. New, D. Stello, C. Régulo, I. W. Roxburgh, D. Salabert, T. R. White, D. A. Caldwell, J. L. Christiansen, and M. N. Fanelli, “Global asteroseismic properties of solar-like oscillations observed by kepler: a comparison of complementary analysis methods,” *Mon. Not. R. Astron. Soc.*, vol. 415, no. 4, pp. 3539–3551, 2011.
- [57] K. Brogaard, C. J. Hansen, A. Miglio, D. Slumstrup, S. Frandsen, J. Jessen-Hansen, M. N. Lund, D. Bossini, A. Thygesen, G. R. Davies, W. J. Chaplin, T. Arentoft, H. Bruntt, F. Grundahl, and R. Handberg, “Establishing the accuracy of asteroseismic mass and radius estimates of giant stars. i. three eclipsing systems at [Fe/H]0.3 and the need for a large high-precision sample,” *Mon. Not. R. Astron. Soc.*, 2018.
- [58] E. Valenti, F. R. Ferraro, and L. Origlia, “Red giant branch in near-infrared colour-magnitude diagrams - II. the luminosity of the bump and the tip,” *Mon. Not. R. Astron. Soc.*, vol. 354, no. 3, pp. 815–820, 2004.
- [59] A. Miglio, W. J. Chaplin, K. Brogaard, M. N. Lund, B. Mosser, G. R. Davies, R. Handberg, A. P. Milone, A. F. Marino, D. Bossini, Y. P. Elsworth, F. Grundahl, T. Arentoft, L. R. Bedin, T. L. Campante, J. Jessen-Hansen, C. D. Jones, J. S. Kuszlewicz, L. Malavolta, V. Nascimbeni, and E. L. Sandquist, “Detection of solar-like oscillations in relics of the milky way: asteroseismology of K giants in M4 using data from the NASA K2 mission,” *Mon. Not. R. Astron. Soc. Lett.*, June 2016.
- [60] F. D’Antona, P. B. Stetson, P. Ventura, A. P. Milone, G. Piotto, and V. Caloi, “The influence of the C N O abundances on the determination of the relative ages of globular clusters: the case of NGC 1851 and NGC 6121 (m4),” *Mon. Not. R. Astron. Soc. Lett.*, vol. 399, no. 1, pp. L151–L155, 2009.
- [61] B. Hendricks, P. B. Stetson, D. A. VandenBerg, and M. Dall’Ora, “A NEW REDDENING LAW FOR M4,” *Astron. J.*, vol. 144, no. 1, p. 25, 2012.
- [62] N. Viaux, M. Catelan, P. B. Stetson, G. G. Raafelt, J. Redondo, A. A. R. Valcarce, and A. Weiss, “Particle-physics constraints from the globular cluster m5: neutrino dipole moments,” *Astron. Astrophys. Suppl. Ser.*, vol. 558, p. A12, 2013.
- [63] O. Straniero, I. Dominguez, M. Giannotti, and A. Mirizzi, “Axion-electron coupling from the RGB tip of Globular Clusters,” *ArXiv e-prints*, Feb. 2018.
- [64] M. Salaris and S. Cassisi, *Evolution of Stars and Stellar Populations*. 2005.
- [65] A. F. Marino, S. Villanova, G. Piotto, A. P. Milone, Y. Momany, L. R. Bedin, and A. M. Medling, “Spectroscopic and photometric evidence of two stellar populations in the galactic

- globular cluster NGC 6121 (m 4)," *Astron. Astrophys. Suppl. Ser.*, vol. 490, no. 2, pp. 625–640, 2008.
- [66] R. Jimenez and P. Padoan, "The ages and distances of globular clusters with the luminosity function method: The case of M5 and M55," *Astrophys. J.*, vol. 498, no. 2, pp. 704–709, 1998.
- [67] R. P. Kraft and I. I. Ivans, "A globular cluster metallicity scale based on the abundance of feii," *Publ. Astro. Soc. Pac.*, vol. 115, no. 804, pp. 143–169, 2003.
- [68] Y. I. Izotov and T. X. Thuan, "MMT observations of new extremely metalpoor EmissionLine galaxies in the sloan digital sky survey," *Astrophys. J.*, vol. 665, no. 2, pp. 1115–1128, 2007.
- [69] Y. I. Izotov and T. X. Thuan, "THE PRIMORDIAL ABUNDANCE OF  $^{4}\text{He}$ : EVIDENCE FOR NON-STANDARD BIG BANG NUCLEOSYNTHESIS," *Astrophys. J.*, vol. 710, no. 1, pp. L67–L71, 2010.
- [70] E. Aver, K. A. Olive, and E. D. Skillman, "A new approach to systematic uncertainties and self-consistency in helium abundance determinations," *J. Cosmol. Astropart. Phys.*, vol. 2010, no. 05, pp. 003–003, 2010.
- [71] T. Constantino, S. W. Campbell, J. Christensen-Dalsgaard, J. C. Lattanzio, and D. Stello, "The treatment of mixing in core helium burning models – i. implications for asteroseismology," *Mon. Not. R. Astron. Soc.*, vol. 452, no. 1, pp. 123–145, 2015.
- [72] T. Constantino, S. W. Campbell, and J. C. Lattanzio, "The treatment of mixing in core helium-burning models – III. suppressing core breathing pulses with a new constraint on overshoot," *Mon. Not. R. Astron. Soc.*, vol. 472, no. 4, pp. 4900–4909, 2017.
- [73] R. Handberg, K. Brogaard, A. Miglio, D. Bossini, Y. Elsworth, D. Slumstrup, G. R. Davies, and W. J. Chaplin, "NGC 6819: testing the asteroseismic mass scale, mass loss and evidence for products of non-standard evolution," *Mon. Not. R. Astron. Soc.*, vol. 472, no. 1, pp. 979–997, 2017.
- [74] J. N. Bahcall, S. Basu, M. Pinsonneault, and A. M. Serenelli, "Helioseismological implications of recent solar abundance determinations," *Astrophys. J.*, vol. 618, no. 2, pp. 1049–1056, 2005.
- [75] N. Vinyoles, A. Serenelli, F. L. Villante, S. Basu, J. Redondo, and J. Isern, "New axion and hidden photon constraints from a solar data global fit," *J. Cosmol. Astropart. Phys.*, vol. 2015, no. 10, pp. 015–015, 2015.
- [76] H. Schlattl, "Helioseismological constraint on solar axion emission," *Astropart. Phys.*, vol. 10, no. 4, pp. 353–359, 1999.
- [77] A. García Saravia Ortiz de Montellano, A. G. S. O. de Montellano, S. Hekker, and N. Themelis, "Automated asteroseismic peak detections," *Mon. Not. R. Astron. Soc.*, vol. 476, no. 2, pp. 1470–1496, 2018.
- [78] K. G. Libbrecht, "On the ultimate accuracy of solar oscillation frequency measurements," *Astrophys. J.*, vol. 387, p. 712, 1992.
- [79] ESA, "Plato: Mission concept," 2017. Accessed: 2018-03-22.
- [80] NASA, "Transiting exoplanet survey satellite," 2014.
- [81] R. L. Gilliland, W. J. Chaplin, J. M. Jenkins, L. W. Ramsey, and J. C. Smith, "Kepler mission stellar and instrument noise properties revisited," *Astron. J.*, vol. 150, no. 4, p. 133, 2015.
- [82] A. Miglio, C. Chiappini, B. Mosser, G. R. Davies, K. Freeman, L. Girardi, P. Jofré, D. Kawata, B. M. Rendle, M. Valentini, L. Casagrande, W. J. Chaplin, G. Gilmore, K. Hawkins, B. Holl, T. Appourchaux, K. Belkacem, D. Bossini, K. Brogaard, M.-J. Goupil, J. Montalbán, A. Noels, F. Anders, T. Rodrigues, G. Piotto, D. Pollacco, H. Rauer, C. A. Prieto, P. P. Avelino, C. Babusiaux, C. Barban, B. Barbay, S. Basu, F. Baudin, O. Benomar, O. Bienaymé, J. Binney, J. Bland-Hawthorn, A. Bressan, C. Cacciari, T. L. Campante, S. Cassisi, J. Christensen-Dalsgaard, F. Combes, O. Creevey, M. S. Cunha, R. S. Jong, P. Laverny, S. Degl'Innocenti, S. Deheuvels, É. Depagne, J. Ridder, P. D. Matteo, M. P. D. Mauro, M.-A. Dupret, P. Eggenberger, Y. Elsworth, B. Famaey, S. Feltzing, R. A. García, O. Gerhard, B. K. Gibson, L. Gizon, M. Haywood, R. Handberg, U. Heiter, S. Hekker, D. Huber, R. Ibata, D. Katz, S. D. Kawaler, H. Kjeldsen, D. W. Kurtz, N. Lagarde, Y. Lebreton, M. N. Lund, S. R. Majewski, P. Marigo, M. Martig, S. Mathur, I. Minchev, T. Morel, S. Ortolani, M. H. Pinsonneault, B. Plez, P. G. P. Moroni, D. Pricopi, A. Recio-Blanco, C. Reylé, A. Robin, I. W. Roxburgh, M. Salaris, B. X. Santiago, R. Schiavon, A. Serenelli, S. Sharma, V. S. Aguirre, C. Soubiran, M. Steinmetz, D. Stello, K. G. Strassmeier, P. Ventura, R. Ventura, N. A. Walton, and C. C. Worley, "PLATO as it is : A legacy mission for galactic archaeology," *Astron.Nachr./AN*, vol. 338, pp. 644–661, July 2017.

# Appendix A

## Stellar Modelling

### A.1 MESA Additions<sup>D</sup>

The following sections document the main additional MESA routine written for this report. Crucially, improvements to the code are presented in Appendix A.1.2.

#### A.1.1 Axion Coupling to Electrons

An extract from the addition written to the `other_neu` MESA routine for the implementation of energy losses due to axion-electron coupling is presented below. This code is placed in the `run_star_extras.f` file in the working directory for each simulation and configured in the `inlist`.

```

subroutine other_neu( &
id, k, T, log10_T, Rho, log10_Rho, abar, zbar,
z2bar, log10_Tlim, flags, &
loss, sources, ierr)
use neu_lib, only: neu_get
use neu_def
integer, intent(in) :: id ! id for star
integer, intent(in) :: k ! cell number or 0 if not
    for a particular cell
real(dp), intent(in) :: T ! temperature
real(dp), intent(in) :: log10_T ! log10 of
    temperature
real(dp), intent(in) :: Rho ! density
real(dp), intent(in) :: log10_Rho ! log10 of
    density
real(dp), intent(in) :: abar ! mean atomic weight
real(dp), intent(in) :: zbar ! mean charge
real(dp), intent(in) :: z2bar ! mean charge
    squared
real(dp), intent(in) :: log10_Tlim
logical, intent(inout) :: flags(num_neu_types) !
    true if should include the type of loss
real(dp), intent(inout) :: loss(num_neu_rvs) !
    total from all sources
real(dp), intent(inout) :: sources(num_neu_types,
    num_neu_rvs)
integer, intent(out) :: ierr

real(dp) :: axionz2ye, axioncsi, faxion, faxioncsi
    , ye, p2f, beta2f, kappa2, &
scomp, sbrem_nd, sbrem_d, stotal, d_stotal_dt,
    d_stotal_drho
type (star_info), pointer :: s

```

```

include 'formats'

ierr = 0
call star_ptr(id, s, ierr)
if (ierr /= 0) return

call neu_get( &
T, log10_T, Rho, log10_Rho, abar, zbar, z2bar,
    log10_Tlim, flags, &
loss, sources, ierr)
if (ierr /= 0) return

!... Fitting from GG Raffelt (1996), implemented
    by Alexander Lyttle (2018)

ye = zbar/abar ! mean no. of free electrons per
    nucleon
axionz2ye = z2bar/abar + ye ! + ye from electron
    contribution

! AXION-ELECTRON - Alexander Lyttle
! need to do everything in natural units then
    finally convert to erg/g/s.
p2f = 26.576d6 * (Rho*ye)**(2.0/3.0)
! fermi momentum squared (natural units)
! p2f = ( 3.0 pi^2 / u )^2/3 * ( rho * ye )^2/3 [
    eV^2]
! atomic mass unit, u = 931.4941 d6 [eV]
! ( 3.0 pi^2 / u )^2/3 = 1.003 446 d-5 [eV^-2/3]
! conversion factor, g/cm^3 -> eV^4, (1.973 270 d
    -5)^3 / 1.782 662 d-33 = 4.310 132 d18 [cm^3/
    g]
! 1.003 446 d-5 * ( 4.310 132 d18 )^2/3 = 26.576
    d6

beta2f = 1.0 / (0.26112d6/p2f + 1.0)
! fermi velocity squared as a fraction of the
    speed of light (natural units)
! beta2f = 1.0 / ( m_e^2 / p2f + 1.0 )
! electron mass, m_e = 0.511 000 d6 [eV]

kappa2 = 2.4620d12 * Rho*ye / (T*p2f)
! { debye screening factor / (sqrt 2 x Fermi
    momentum) } squared for use in faxion
! kappa2 = { ( 2 * pi * alpha ) / u } * { ( rho *
    ye ) / ( T * p2f ) } [dimensionless]
! fine struc const, alpha = 7.297 353 d3
! ( 2 * pi * alpha ) / u = 4.922 266 d-11 [eV^-1]

```

```

! conversion factor, g/(cm^3 K) -> eV^3, 4.310 132
  d18 [cm^3/g] * 1.160 451 d4 [K] = 5.001 697
  d23 [cm^3 K/g]
! 4.922 266 d-11 * 5.001 697 d23 = 2.4620d12

faxion = 2.0/3.0 * log((2.0 + kappa2)/kappa2) +
  ((2.0 + 5.0*kappa2)/15.0 * log((2.0 + kappa2)/kappa2) - 2.0/3.0)*beta2f
! function to take account of relativistic and
  degenerate effects.

scomp = 2.6261d-48 * axion_g13*axion_g13*ye*T
  **6*faxion
! this is the loss rate per unit mass per unit
  time due to Compton
! scmp = 33.0 * g_13^2 / (4 * pi) * ye * (T_8 x
  10^-8)^6 * faxion [erg/g/s]
! T_8 = T * 10^-8
! 33.0 * (10^-8)^6 / (4 * pi) = 2.6261d-48

sbrem_nd = 46.951d-26 * axion_g13*axion_g13*ye*T
  **(2.5)*Rho*(axionz2ye + ye/sqrt(2.0))
! this is the loss rate due to non-degenerate
  bremsstrahlung
! sbrem_nd = 590.0 * axion_g13^2 / (4 * pi) * ye *
  T_8^2.5 * rho_6 * (axionz2ye + ye/sqrt(2.0))
  [erg/g/s]
! rho_6 = rho * 10^-6
! 590.0 * (10^-8)^2.5 * 10^-6 / (4 * pi) =
  46.951d-26

sbrem_d = 0.85944d-32 * axion_g13*axion_g13*T**4*
  faxion*axionz2ye
! this is the loss rate due to degenerate
  bremsstrahlung
! sbrem_d = 10.8 * axion_g13^2 / (4 * pi) * T^4 *
  faxion * axionz2ye [erg/g/s]
! 10.8 * (10^-8)^4 / (4 * pi) = 0.85944d-32

stotal = scmp + 1.0/(1.0/sbrem_nd + 1.0/sbrem_d)
! interpolates the three energy loss effects

! these don't seem to be required now
d_stotal_dT = 0
d_stotal_dRho = 0

! Add the loss rates to MESA's neutrino rates
loss(ineu) = loss(ineu) + stotal
loss(idneu_dT) = loss(idneu_dT) + d_stotal_dT
loss(idneu_dRho) = loss(idneu_dRho) +
  d_stotal_dRho

! Output to terminal, is this correct way to do it
?
!if (k == s% nz) write(*,3) 'beta2f', s%
  model_number, k, beta2f
!if (k == s% nz) write(*,3) 'faxon', s%
  model_number, k, faxion
!if (k == s% nz) write(*,3) 'kappa2', s%
  model_number, k, kappa2
!if (k == s% nz) write(*,3) 'stotal', s%
  model_number, k, stotal

end subroutine other_neu

```

### A.1.2 Improvements

Some improvements to the MESA addition written for axion-electron coupling have become apparent since carrying out the investigation. These include a correction to the implementation of Equation (??) for axion-electron Compton energy-loss, and a few minor corrections to the sums over ions and electrons used. The effects of these corrections are unlikely to have changed the general affect of axion-cooling on the star, but may have increased the total losses by some factor of order unity.

Consider Equation (??) added to the MESA axion-cooling routine,

```

faxion = 2.0/3.0 * log((2.0 + kappa2)/kappa2) +
  ((2.0 + 5.0*kappa2)/15.0 * log((2.0 + kappa2)/kappa2) - 2.0/3.0)*beta2f
! function to take account of relativistic and
  degenerate effects.

scomp = 2.6261d-48 * axion_g13*axion_g13*ye*T
  **6*faxion
! this is the loss rate per unit mass per unit
  time due to Compton
! scmp = 33.0 * g_13^2 / (4 * pi) * ye * (T_8 x
  10^-8)^6 * faxion [erg/g/s]
! T_8 = T * 10^-8
! 33.0 * (10^-8)^6 / (4 * pi) = 2.6261d-48

```

Here the function `faxion` is used to account for degenerate effects (see Equation (2.50)). However, this is incorrect and has been confused with the function accounting for similar effects in the degenerate bremsstrahlung case. The function should cause the Compton case to fall off at very hight densities but it does not. A suggested improvement would be to use the function  $f_{deg}$  in Equation (2.45) and multiply the energy-loss by  $(1 + f_{deg}^{-2})^{-1/2}$  (see Equation (2.44)),

```
fdeg = 3*T/(1.16d4*sqrt(beta2f*p2f))
```

```
scomp = 2.6261d-48 * axion_g13**2*ye*T**6*(1 +
  fdeg**(-2))**(-0.5)
```

This causes the Compton energy-loss to fall off as shown in Figure 2.11.

Further changes should be made to the value of  $\kappa^2$  calculated in the code where the Debye screening wavenumber was used rather than the Debye-Hückel wavenumber,

```

kappa2 = 2.4620d12 * Rho*ye / (T*p2f)
! { debye screening factor / (sqrt 2 x Fermi
  momentum) } squared for use in faxion
! kappa2 = { ( 2 * pi * alpha ) / u } * { ( rho *
  ye ) / ( T * p2f ) } [dimesionless]
! fine struc const, alpha = 7.297 353 d3
! ( 2 * pi * alpha ) / u = 4.922 266 d-11 [eV^-1]
! conversion factor, g/(cm^3 K) -> eV^3, 4.310 132
  d18 [cm^3/g] * 1.160 451 d4 [K] = 5.001 697
  d23 [cm^3 K/g]
! 4.922 266 d-11 * 5.001 697 d23 = 2.4620d12

```

should be corrected to,

```
axionz2ye = ye + zbar^2/abar
```

```

kappa2 = 2.4620e12 * Rho*axionz2ye / (T*p2f)

Furthermore, axionz2ye has been misused later on
in the calculation of bremsstrahlung losses (Equations
(2.48) and (2.49))

sbrem_nd = 46.951d-26 * axion_g13*axion_g13*ye*T
    **(2.5)*Rho*(axionz2ye + ye/sqrt(2.0))
! this is the loss rate due to non-degenerate
    bremsstrahlung
! sbrem_nd = 590.0 * axion_g13^2 / (4 * pi) * ye *
    T_8^2.5 * rho_6 * (axionz2ye + ye/sqrt(2.0))
    [erg/g/s]
! rho_6 = rho * 10^-6
! 590.0 * (10^-8)^2.5 * 10^-6 / (4 * pi) =
    46.951d-26

sbrem_d = 0.85944d-32 * axion_g13*axion_g13*T**4*
    faxion*axionz2ye
! this is the loss rate due to degenerate
    bremsstrahlung
! sbrem_d = 10.8 * axion_g13^2 / (4 * pi) * T^4 *
    faxion * axionz2ye [erg/g/s]
! 10.8 * (10^-8)^4 / (4 * pi) = 0.85944d-32

```

should be corrected to,

```
z2a = z2bar/abar
```

```
sbrem_nd = 46.951e-26 * axion_g13**2*ye*T**2.5*
    Rho*(z2a + ye/np.sqrt(2.0))
```

```
sbrem_d = 8.5944e-33 * axion_g13**2*T**4*faxion*
    z2a
```

Typically,  $Y_e \approx 1/2$ , thus effects due to the latter error lead to systematically greater bremsstrahlung energy-loss rates by a factor of 1.5. Error due to not suppressing the Compton case at high density is less easy to predict, so it should be corrected for in future experiments.

## A.2 GYRE Input<sup>G</sup>

An example of the GYRE namelist input file used throughout this investigation to calculate modes of harmonic degree  $l = 0$  and  $l = 1$  with continuous radial order for early evolution, low luminosity RGB stars and post-helium burning Red Clump stars.

```

&constants
/
&model
  model_type = 'EVOL' ! Obtain stellar structure
    from an evolutionary model
  file = 'Stellar_Model.GYRE' ! File name of the
    evolutionary model
  file_format = 'MESA' ! File format of the
    evolutionary model
/
&mode
  l = 0          ! Harmonic degree
  tag = 'radial' ! Tag for namelist matching
/

```

```

&mode
  l = 1          ! Harmonic degree
  tag = 'non-radial' ! Tag for namelist matching
/
&osc
  outer_bound = 'JCD' ! Use a Christensen-
    Dalsgaard (ADIPLS) outer mechanical boundary
    condition to allow use of acoustic cut-off
    frequency units
  tag_list = 'radial,non-radial' ! Comma-separated
    list of tags
/
&num
  diff_scheme = 'MAGNUS_GL4' ! 4th-order Magnus
    solver for initial-value integrations
/
&scan
  grid_type = 'LINEAR' ! Scan for modes using a
    uniform-in-frequency grid; best for p modes
  freq_min_units = 'ACOUSTIC_CUTOFF' ! Minimum
    frequency given in acoustic cut-off
    frequency units
  freq_max_units = 'ACOUSTIC_CUTOFF' ! Maximum
    frequency given in acoustic cut-off
    frequency units
  freq_min = 0.1 ! Minimum frequency to scan from
  freq_max = 0.9 ! Maximum frequency to scan to
  n_freq = 1000 ! Number of frequency points in
    scan
  tag_list = 'radial' ! Tag matching scan
/
&scan
  grid_type = 'INVERSE' ! Scan for modes using a
    uniform-in-period grid; best for g modes
  freq_min_units = 'ACOUSTIC_CUTOFF' ! Minimum
    frequency given in acoustic cut-off
    frequency units
  freq_max_units = 'ACOUSTIC_CUTOFF' ! Maximum
    frequency given in acoustic cut-off
    frequency units
  freq_min = 0.1 ! Minimum frequency to scan from
  freq_max = 0.9 ! Maximum frequency to scan to
  n_freq = 10000 ! Number of frequency points in
    scan
  tag_list = 'non-radial' ! Tag matching scan
/
&grid
  alpha_osc = 10 ! Ensure at least 10 points per
    wavelength in propagation regions
  alpha_exp = 2 ! Ensure at least 2 points per
    scale length in evanescent regions
  n_inner = 5 ! Ensure at least 5 points between
    center and inner turning point
/
&ad_output
  summary_file = 'summary.txt' ! File name for
    summary file
  summary_file_format = 'TXT' ! Format of summary
    file

```

```
summary_item_list = 'M_star,R_star,L_star,j,l,          mode_item_list = 'M_star,R_star,L_star,l,n_pg,
    n_pg,n_p,n_g,freq,freq_units,Delta_p,Delta_g      freq,xi_r,xi_h,prop_type' ! Items to
    ,E_p' ! Items to appear in summary file           appear in mode files
freq_units = 'UHZ' mode_template = 'mode.%J.txt /      '
    ! File-name template for mode files
mode_file_format = 'TXT' ! Format of mode files      &nad_output
    /
```

## Appendix B

# Tables

### B.1 Luminosity of the TRGB<sup>J</sup>

Table B.1: Luminosity of the TRGB with no axion cooling,  $L_{tip}$  and with an axion cooling of  $g_{a\gamma} = 0.66 \times 10^{-10} \text{ GeV}^{-1}$  in the column  $L_{tip}^{a\gamma}$ . The difference between the two is given by  $\Delta L_{tip} = L_{tip}^{a\gamma} - L_{tip}$  with its respective errors.

$M/M_\odot$	$L_{tip}/\text{dex}$	$\sigma_L/\text{dex}$	$L_{tip}^{a\gamma}/\text{dex}$	$\sigma_L^{ae}/\text{dex}$	$\Delta L_{tip}/\text{dex}$	$\sigma_{\Delta L}/\text{dex}$
0.8	3.3960	0.0010	3.4265	0.0006	0.0304	0.0012
0.9	3.3940	0.0010	3.4249	0.0007	0.0313	0.0013
1.0	3.3910	0.0010	3.4228	0.0008	0.0322	0.0014
1.1	3.3878	0.0009	3.4207	0.0007	0.0330	0.0011
1.2	3.3861	0.0006	3.4194	0.0005	0.0333	0.0008
1.3	3.3847	0.0004	3.4185	0.0003	0.0338	0.0005
1.4	3.3841	0.0004	3.4178	0.0003	0.0337	0.0005
1.5	3.3828	0.0008	3.4171	0.0005	0.0343	0.0010
1.6	3.3800	0.0020	3.4150	0.0010	0.0350	0.0024
1.7	3.3730	0.0050	3.4100	0.0040	0.0375	0.0065
1.8	3.3500	0.0100	3.4000	0.0100	0.0421	0.0169
1.9	3.3000	0.0200	3.3600	0.0100	0.0576	0.0242
2.0	3.2100	0.0400	3.3000	0.0200	0.0932	0.0459

# Glossary

## Acronyms

Table B.2: Acronyms used throughout this report.

Acronym	Definition
AGB	Asymptotic Giant Branch
BCZ	Base of the Convective Zone
CMD	Colour-Magnitude Diagram
CNO	Carbon-Nitrogen-Oxygen
CP	Charge-Parity
HeCB	Helium Core Burning
HOV	High Overshooting
HRD	Hertzsprung-Russell Diagram
KIC	Kepler Input Catalogue
KDE	Kernel Density Estimate
LOV	Low Overshooting
MESA	Modules for Experiments in Stellar Astrophysics
MOV	Medium Overshooting
MS	Main Sequence
NGC	New General Catalogue
QCD	Quantum Chromodynamics
RC	Red Clump
RGB	Red Giant Branch
SG	Sub-Giant
SGB	Sub-Giant Branch
TAMS	Terminal-Age Main Sequence
TP	Thermal Pulse
TRGB	Tip of the Red Giant Branch
ZAMS	Zero-Age Main Sequence

## Symbols

Table B.3: Symbols used throughout this report.

Symbol	Units	Definition
$g_{a\gamma}$	$GeV^{-1}$	Axion-Photon Coupling Strength
$g_{ae}$	none	Axion-Electron Coupling Strength (Yukawa)
$g_{10}$	$GeV^{-1}$	$g_{a\gamma} \times 10^{-10}$
$g_{13}$	none	$g_{ae} \times 10^{-13}$
M	$M_\odot$	Stellar Mass
L	$L_\odot$	Stellar Luminosity
$\mathcal{M}$	none	Absolute Magnitude